The top portal to new physics

de Beurs, M.P.R.

Publication date
2022

Document Version
Final published version

Link to publication

Citation for published version (APA):
de Beurs, M. P. R. (2022). *The top portal to new physics*. [Thesis, fully internal, Universiteit van Amsterdam].

Marc de Beurs

A top portal to new physics

ACADEMISCH PROEFSCHRIFT

ter verkrijging van de graad van doctor
aan de Universiteit van Amsterdam
op gezag van de Rector Magnificus
prof. dr. ir. K.I.J. Maex
ten overstaan van een door het College voor Promoties ingestelde commissie,
in het openbaar te verdedigen in de Agnietenkapel
op donderdag 31 maart 2022, te 13.00 uur

door Marcus Pieter Raymond de Beurs
geboren te Amsterdam

Promotiecommissie

Promotores:	prof. dr. M. Vreeswijk	Universiteit van Amsterdam
	prof. dr. E.L.M.P. Laenen	Universiteit van Amsterdam
Overige leden:	dr. E. Vryonidou	University of Manchester
	dr. P. Ferrari	Nikhef
	prof. dr. ir. P.J. de Jong	Universiteit van Amsterdam
	prof. dr. S.C.M. Bentvelsen	Universiteit van Amsterdam
	prof. dr. H.G. Raven	Vrije Universiteit Amsterdam
	prof. dr. W. Verkerke	Universiteit van Amsterdam
	dr. I.B. van Vulpen	Universiteit van Amsterdam

Faculteit der Natuurwetenschappen, Wiskunde en Informatica

Publications

Chapter 3: M. de Beurs, E. Laenen, M. Vreeswijk, E. Vryonidou. "Effective operators in t-channel single top production and decay". In: The European Physical Journal C volume 78, Article number: 919 (2018), p. 919. Reference [1].

All authors contributed to the strategy of the analysis, the interpretation of the results and the editing of this paper. MB was mostly responsible for the Monte Carlo simulations and the analysis. EV was of essential support for the production of the Monte Carlo samples and conducted crucial cross checks.

Chapters 5, 6 and 8: R. Bi, J. Boudreau, N. Bruscino, S. Cabrera Urban, M.J. Costa Mezquita, M. de Beurs, C. Escobar Ibanez, O. Estrada Pastor, G.R. Gonzalvo Rodriguez, J.A. Mueller, M. Vreeswijk, P. Martinez Agullo, J.E. Garcia Navarro, C.W. Ng, J. Degens, H. Cai. "Measurement of the polarisation of top quarks and antiquarks produced in the t-channel collected by the ATLAS detector at $\sqrt{s} = 13$ TeV and bounds on the tWb dipole operator". In: Journal of High Energy Physics, *to be published*.

Supervision on the unfolding measurement has been done by SCU, MJCM, JEGN and CEI. Optimisation of the signal region has been done by PMA and SCU and the unfolding analysis has been done by OEP and GGR. Supervision on the extraction of the EFT coefficients has been done by MV and JM. MB build the signal model, exploiting the morphing technique, and analysed the data in terms of the EFT coefficients. The paper was mostly edited by JB, MJCM, MB, CEI, RGR and JAM. This paper will also contain a template fit approach, not included in this thesis, which was supervised by JB, NB and JM, and was analysed by RB and CWN..

Table of contents

PJOT

Introduction

The universe is a mysterious and wonderful place. Since the beginning of time, humanity has been wondering about fundamental questions, such as: what happened at the very beginning and what is everything made of? Doing research provides the possibility to unravel some of these mysteries and often reveals utter beauty. This thesis is a small contribution to the quest for the complete understanding of everything around us.

One of the greatest successes in trying to answer these fundamental questions is the standard model of particle physics (SM). It offers a theoretical description of all the building blocks in the universe and how they interact with each other. Rather than a thorough review of the SM, this thesis contains a snapshot of the current status.

At the current stage already a lot is known about the building blocks of nature. All matter consists of fermions that interact through bosons. The fundamental forces of nature are thus governed by particles. The electromagnetic force can be described by the exchange of photons, its force carrier. The same holds for the weak and strong nuclear forces that are mediated by the vector bosons (Z and W) and gluons, respectively. A key feature of the SM is that all these forces are united into one theory. An immediate shortcoming is however that it does not include gravity. Combining the SM, a quantum field theory, with Einstein's classical theory of general relativity remains an unsolved issue.

The full content of the SM can be expressed by the elementary particles given in figure 1, where the blue lines show with whom the force carriers (bosons) interact. The leptons and the quarks together make up the fermion sector. The difference between the two categories of fermions is that quarks carry the colour charge and couple to gluons. There are three generations of fermions distinguished only by a difference in mass. The origin of mass is attributed to the Higgs mechanism and the discovery of its associated boson was a huge milestone in 2012 [2]. Of particular interest in this work is the heaviest known elementary particle: the top quark. Due to its large mass, it decays before it hadronises making it possible to study its spin and coupling properties directly.

The SM has been very successful at the energies that current experiments reach. However, it can not be the complete theory. As already mentioned above there remains the open question about gravity, but there is more. From cosmological observations it seems that the SM only describes about 5% of the total energy in the universe [4]. In a sense we only see the tip of the iceberg, where the yet unknown energy sources are referred to as Dark Matter and Dark Energy. Even in the part we do see, the visible 5% described by the SM, a huge mismatch between matter and anti-matter exists. In the SM equal amounts of matter and anti-matter are produced. A small deviation from this exists in the weak sector, although it is by no means enough to explain the matter dominated universe. All this hints towards yet unknown processes that occur at energies higher than currently probed.

In a sense the SM should be seen as an approximate model. At higher energies processes should exist that are responsible for the asymmetry between matter and anti-matter. This is why particle accelerators want to keep increasing their collision energy, to enhance the sensitivity in the so-called direct searches. There is however another way to be able to obtain a glimpse of physics beyond the standard model (BSM). This is through very precise measurements, also known as indirect searches. In the quantum world all existing processes lead to (small) corrections to measured values. Very precise measurements possibly reveal deviations from the theoretical predictions, which would be an explicit hint of new physics.

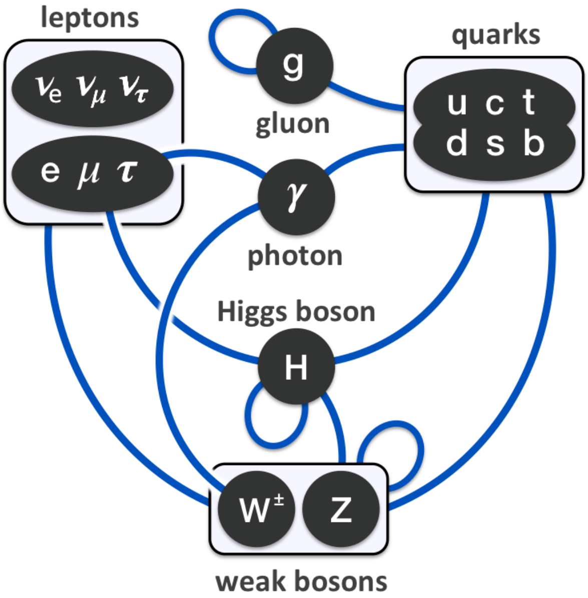

Figure 1: The standard model content and its interactions. The top left (leptons) and top right (quarks) make up all the matter. In the middle the force carries are shown, where the blues lines depict with whom they interact. This figure has been taken from [3].

The quest for the origin of the asymmetry between matter and anti-matter in the universe is the main motivation for this work. Data collected with the ATLAS detector in the years 2015 until 2018 is used to study the top quark. As the top decays, it conveys all its spin information to its decay products. As a result, distributions of spin correlated observables are analysed to provide sensitivity to the production and/or decay mechanism of the top quark. The framework of Effective Field Theory (EFT) is exploited to predict the deviations in the observed distributions. The EFT is model independent, but adds mathematical structures to the SM that become increasingly manifest at high energy scales. One such structure is the operator O_{tW}, which is of paramount interest as it could cause an asymmetry between matter and anti-matter.

The work in this thesis is divided into three main parts. Part I contains the phenomenological study on how EFT affects the single top quark process. It discusses the important theoretical aspects and presents the most sensitive distributions for measuring deviations from the SM based on Monte Carlo (MC) simulations. In part II the experimental analysis on measuring these distributions with the ATLAS detector is provided. The technique of unfolding is employed to remove effects caused by the detector material, making it possible to compare the measured results directly to simulations. Finally in part III the measured results are interpreted in terms of EFT operators, where a morphing technique is exploited for the parametric description of the signal.

Part I

Phenomenological study

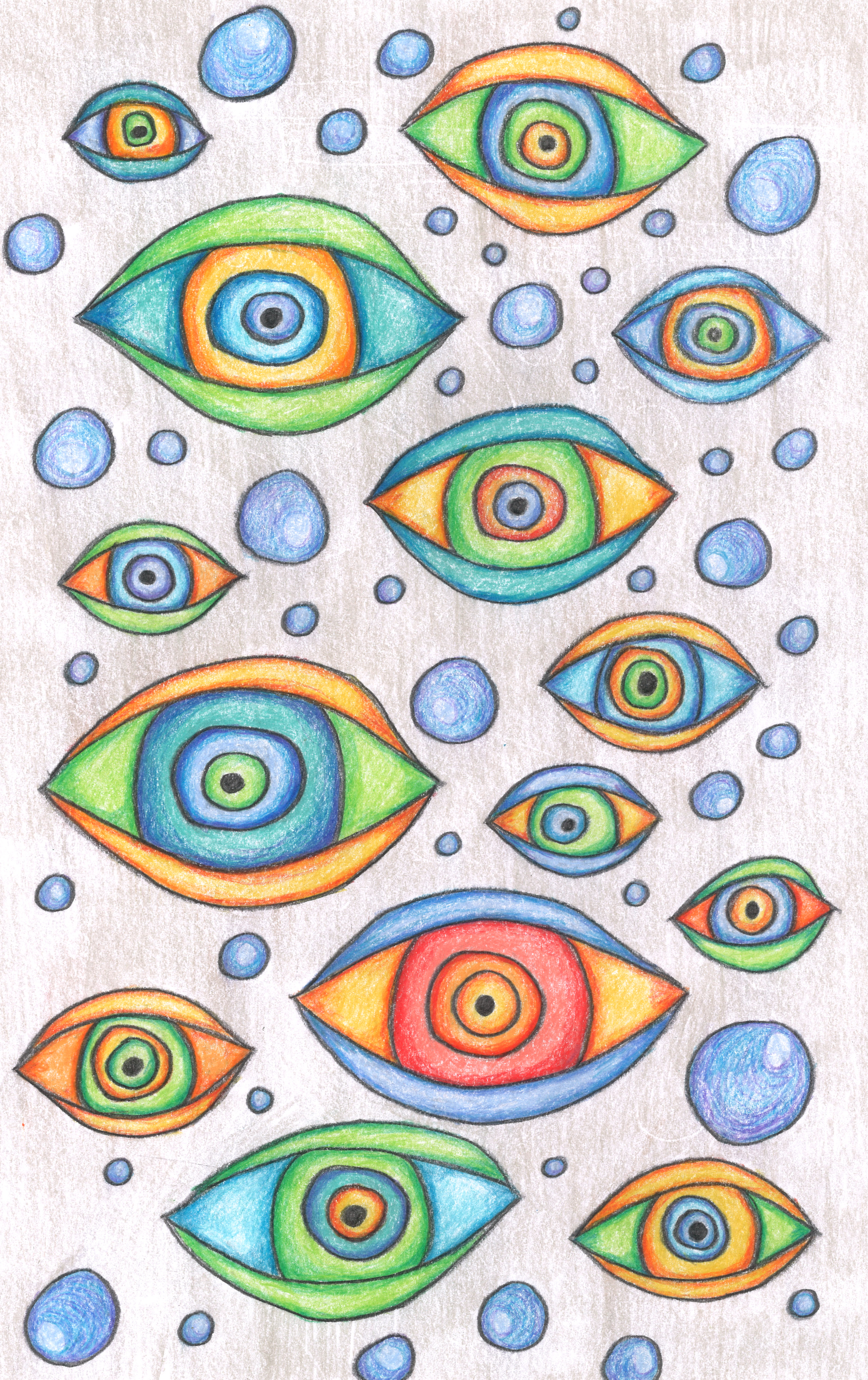
PJOT

Chapter 1

Theoretical framework

This chapter presents the important theoretical aspects related to this work. The sections discussing the single top quark (1.2) and Effective Field Theory (1.3) contain parts from earlier work, published as [1].

1.1 Standard Model

The standard model of particle physics (SM) is described in detail in numerous books [5, 6, 7, 8]. In this section only the topics that are of special interest to this research are briefly addressed.

1.1.1 Mathematical formalism

The SM describes all the kinematics of elementary particles and their interactions, which is mathematically represented by the SM Lagrangian. As introduction, the following equation shows the Lagrangian for the kinematic term of fermions:

$$\mathcal{L}_{\text{fermion}} = \bar{\psi}\left(i\gamma^{\mu}\partial_{\mu} - m\right)\psi, \tag{1.1}$$

where ψ corresponds to a fermion field with a mass m and the Lorentz index μ runs from zero to three, the spinor indices are not shown. Lorentz invariance is apparant when all Lorentz indices are contracted. This Lagrangian leads to the famous Dirac equation that represents the equation of motion (EOM) for a massive fermion:

$$\left(i\gamma^{\mu}\partial_{\mu} - m\right)\psi = 0. \tag{1.2}$$

The lowest order solution to equation 1.2 has four components, resulting in ψ being represented by a vector with four entries, called a spinor, and each component of γ being a 4×4 matrix. There are different possible choices on the representation of the fermion field together with the γ matrices. It should be clear that each choice of basis must be consistent with the Dirac equation, leading to the same physical results.

Defining the fermion field based on its handedness or chirality, which will be discussed in the next paragraph, corresponds to the Weyl representation:

$$\psi = \begin{bmatrix} \psi_L \\ \psi_R \end{bmatrix}, \quad \gamma^0 = \begin{bmatrix} 0 & \mathbb{1} \\ \mathbb{1} & 0 \end{bmatrix}, \quad \gamma^k = \begin{bmatrix} 0 & \sigma^k \\ -\sigma^k & 0 \end{bmatrix}, \quad \gamma^5 = \begin{bmatrix} -\mathbb{1} & 0 \\ 0 & \mathbb{1} \end{bmatrix}, \tag{1.3}$$

where the L and R indices indicate the handedness, $\mathbb{1}$ the identity matrix and σ^k one of the Pauli spin matrices with k the space index running from one to three.

Only bilinear combinations of spinors and γ matrices can enter in the Lagrangian. Five distinct such combinations exist that behave differently under parity. They are summarised in table 1.1, where $\bar{\psi} = \psi^{\dagger}\gamma^0$ is the adjoint spinor.

Form	Type	Components
$\bar{\psi}\psi$	scalar	1
$\bar{\psi}\gamma^5\psi$	pseudo scalar	1
$\bar{\psi}\gamma^\mu\psi$	vector	4
$\bar{\psi}\gamma^\mu\gamma^5\psi$	axial vector	4
$\bar{\psi}\left(\gamma^\mu\gamma^\nu - \gamma^\nu\gamma^\mu\right)\psi$	tensor	6

Table 1.1: Bilinear combinations of spinors and γ matrices.

1.1.2 Charged weak interaction

The term in the SM Lagrangian describing the charged weak interaction is given in equation 1.4, where g_w corresponds to its coupling strength and W_μ represents the field of its mediator: the W boson with a mass of approximately 80 GeV.

$$\mathcal{L}_{\text{charged current}} = -\frac{g_w}{2\sqrt{2}}\bar{\psi}\gamma^\mu\left(1-\gamma^5\right)\psi\, W_\mu + \text{h. c.} \tag{1.4}$$

The weak interaction posses two unique features: it distinguishes between chiralities and it causes transitions between the different flavours of fermions. Both will be addressed in separate paragraphs below.

Chirality

As presented in table 1.1, $\bar{\psi}\gamma^\mu\psi$ behaves as a vector and $\bar{\psi}\gamma^\mu\gamma^5\psi$ as an axial vector under a parity transformation. The structure of the weak interaction, seen in equation 1.4, can therefore be referred to as V-A and this causes parity to be maximally violated: it differentiates maximally between left and right handed fields. This is a unique feature of the charged current interaction.

The handedness (or chirality) of a fermion is defined by the eigenstates of the γ^5 matrix, which is how the chiral representation of the fermion field is constructed:

$$\gamma^5\psi_R = +\psi_R, \qquad \gamma^5\psi_L = -\psi_L. \tag{1.5}$$

Useful operators are the chiral projectors that pick out the corresponding handedness:

$$P_R = \frac{1}{2}\left(1+\gamma^5\right), \qquad P_L = \frac{1}{2}\left(1-\gamma^5\right). \tag{1.6}$$

$$\begin{aligned} P_R\psi_R &= \psi_R, \qquad & P_R\psi_L &= 0. \\ P_L\psi_R &= 0, \qquad & P_L\psi_L &= \psi_L. \end{aligned} \tag{1.7}$$

The Lagrangian of the charged current, equation 1.4, can thus be written with $\bar{\psi}P_L\psi$ which makes the maximum violation of parity directly apparent.

Chirality is an important quantity to classify and describe the interactions of the SM. It is however not conserved as it does not commute with the Hamiltonian[1]: $[\gamma^5, H] \propto -m\gamma^5$. For massless particles chirality is conserved and it coincides with a different quantity: helicity. Most interactions analysed in this thesis involve particles with relatively small mass. Helicity is therefore a very helpful quantity to describe them (at least qualitatively). It is defined as the direction of momentum of a particle with respect to its spin axis $\left(\frac{s\cdot p}{|p|}\right)$. For massive particles helicity is not Lorentz invariant since boosting to a frame that travels faster than the particle will result in the momentum pointing in the opposite direction. The relation between helicity and chirality is:

$$\begin{aligned} \psi_\uparrow &\propto \frac{1}{2}(1-\kappa)\psi_R + \frac{1}{2}(1+\kappa)\psi_L, \\ \psi_\downarrow &\propto \frac{1}{2}(1+\kappa)\psi_R + \frac{1}{2}(1-\kappa)\psi_L, \end{aligned} \tag{1.8}$$

---

[1] Recall that the expectation value of an operator evolves over time as: $\frac{d}{dt} < O > = i < [H, O] >$.

where $\kappa = \frac{p}{E+m}$. It can be seen that only in limit $m \to 0$ (so that $E = p$ and $\kappa = 1$) helicity and chirality are the same.

Flavour changing

The weak force couples with the same strength to all fermions. This is however in the flavour eigenstate of the fermions, which is different from the physical mass eigenstate. In a sense fermions propagate through space as the mass eigenstate, but interact via the weak force in the flavour eigenstate. A mass eigenstate is thus a combination of all flavours with its composition described by the Cabibbo-Kobayashi-Maskawa (CKM) matrix [9, 10] for quarks and the Pontecorvo–Maki–Nakagawa–Sakata (PMNS) matrix [11, 12] for neutrinos[2].

$$\begin{bmatrix} d' \\ s' \\ b' \end{bmatrix} = \begin{bmatrix} V_{ud} & V_{us} & V_{ub} \\ V_{cd} & V_{cs} & V_{cb} \\ V_{td} & V_{ts} & V_{tb} \end{bmatrix} \begin{bmatrix} d \\ s \\ b \end{bmatrix} \qquad \begin{bmatrix} \nu_e \\ \nu_\mu \\ \nu_\tau \end{bmatrix} = \begin{bmatrix} U_{e1} & U_{e2} & U_{e3} \\ U_{\mu 1} & U_{\mu 2} & U_{\mu 3} \\ U_{\tau 1} & U_{\tau 2} & U_{\tau 3} \end{bmatrix} \begin{bmatrix} \nu_1 \\ \nu_2 \\ \nu_3 \end{bmatrix} \tag{1.9}$$

The off-diagonal elements of these matrices describe the probability of a transition between different generations, a unique feature of the weak force. Each of these 3 × 3 unitary matrices can be parameterised by three rotation angles and one[3] complex phase. The angles represent the mixing between the different flavour states and a non-zero complex phase signifies $V_{ij} \neq V_{ij}^*$ (for some ij) which is connected to CP violation.

1.1.3 CP violation in the SM

As mentioned in the introduction of this thesis, the quest for the origin of CP violation is the main motivator for this work. This section makes the connection between CP violation and a non-zero complex phase in the CKM matrix, which encompasses all the CP violation in the SM. CP violation beyond the SM, arising from effective operators, will be discussed in section 1.3.3.

A violation of the CP symmetry causes a difference between a particle and the corresponding anti-particle process. It can manifest itself in three different effects:

- CP violation in a decay: $A \to B \neq \bar{A} \to \bar{B}$,
- CP violation in the mixing of neutral mesons: $A^0 \longleftrightarrow \bar{A}^0$, where $A^0 \to \bar{A}^0 \neq \bar{A}^0 \to A^0$,
- CP violation in the interference between decays to a common final state, with or without mixing: $A^0(\to \bar{A}^0) \to B \neq \bar{A}^0(\to A^0) \to B$.

All three effects have been measured in B-mesons and/or kaons. For example: the difference between $B^0 \to K^+\pi^-$ and $\bar{B}^0 \to K^-\pi^+$ [13], the mixing of $K^0 \longleftrightarrow \bar{K}^0$ [14] and the interference between $K^0 \to \pi^+\pi^-$ and $\bar{K}^0 \to \pi^+\pi^-$ [15].

CP violation in the SM arises due to the unitarity of the CKM matrix. This leads to relations between the elements in the matrix, such as equation 1.10, that can be visualised with a unitary triangle shown in figure 1.1.

$$V_{ud}V_{ub}^* + V_{cd}V_{cb}^* + V_{td}V_{tb}^* = 0 \tag{1.10}$$

The area of such a triangle is proportional to the amount of CP violation in the SM. The angles γ and β change sign under CP conjugation, which lead to CP violating processes [16].

A logical way to parameterise the unitary CKM matrix is with three mixing angles (θ) and one complex phase (δ). This is done in equation 1.11 where s_{ij} and c_{ij} correspond to $\sin\theta_{ij}$ and $\cos\theta_{ij}$, respectively, and i, j denote the quark families involved.

---

[2] There is no mixing of flavours in the charged lepton sector, since the flavour of the charged lepton is defined by its mass.

[3] In order for this to be true also for the PMNS matrix, the neutrinos are assumed to be Dirac particles. If they happen to be Majorana particles then two additional phases are needed.

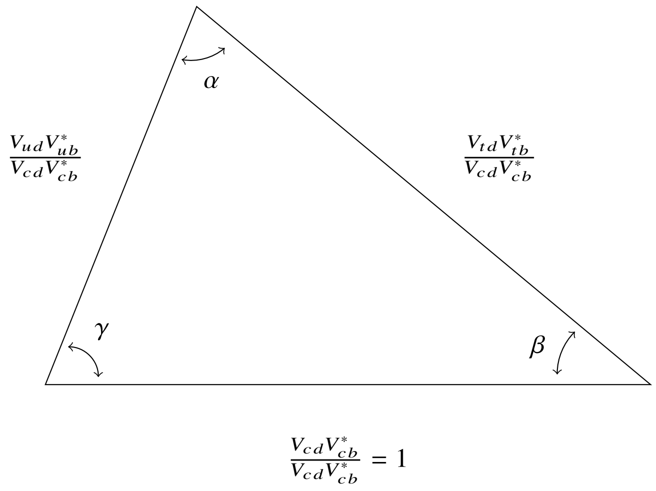

Figure 1.1: Visualisation of the unitarity relation given in equation 1.10. Its area is proportional to the amount of CP violation in the weak sector of the SM.

$$V_{CKM} = \begin{bmatrix} c_{12}c_{13} & s_{12}c_{13} & s_{13}e^{-i\delta_{13}} \\ -s_{12}c_{23} - c_{12}s_{23}s_{13}e^{i\delta_{13}} & c_{12}c_{23} - s_{12}s_{23}s_{13}e^{i\delta_{13}} & s_{23}c_{13} \\ s_{12}s_{23} - c_{12}c_{23}s_{13}e^{i\delta_{13}} & -c_{12}s_{23} - s_{12}c_{23}s_{13}e^{i\delta_{13}} & c_{23}c_{13} \end{bmatrix} \tag{1.11}$$

One can define the Jarlskog invariant, expressed in equation 1.12, which is proportional to the area of the triangle, making the connection between the complex phase (δ) and CP violation apparent [17].

$$J = c_{12}c_{13}^2c_{23}s_{12}s_{13}s_{23}\sin\delta_{13} \tag{1.12}$$

The value for J, and thus the amount of CP violation in the SM, is ten orders of magnitude too small to account for the asymmetry seen in the universe between matter and anti-matter [18]. This remains one of the most important open issues in physics.

1.2 Single Top Physics

The top quark is the heaviest known elementary particle. It forms the third generation of quarks together with the b-quark and its existence was predicted based on the observed CP violation in kaon decays [10]. About 25 years ago (in 1995) the CDF and D0 experiments discovered the top quark with a mass of about 175 GeV [19, 20]. Due to its mass being larger than the W boson, it decays before it hadronises through the weak interaction [21]. This makes the top quark the only possibility to study a quark not hidden in a hadron.

The single top quark process is of special interest since it is produced via the weak interaction, which has a V-A structure. As discussed in section 1.1.2, this chiral nature means that only left-handed top quarks are produced (and right-handed anti-top quarks). As a result, the spin of the top quark points in the direction of the spectator jet (about 96% of the time [22]). Since the top decays before hadronisation, full spin information is transmitted to its decays products and can be studied. This is a unique feature of the single top quark process.

1.2.1 Production

In the SM a single top quark is produced through an interaction with a W boson. Using the definitions from the previous section, the corresponding term in the SM Lagrangian reads:

$$\mathcal{L}_{Wtb}^{\mathrm{SM}} = -\sum_{f=d,s,b}^{3} \frac{g_w V_{tf}}{\sqrt{2}} \bar{q}_f(x)\gamma^\mu P_L t(x)\, W_\mu(x) + \text{h. c.} \tag{1.13}$$

The coupling strength is denoted by g_w and the coefficient V_{tf} is an element of the CKM matrix (equation 1.9 on the left). The fields of the top quark, W boson and lighter quarks are denoted by $t(x)$, $W_\mu(x)$ and $q_f(x)$, respectively, with $f = d, s, b$ indicating the down, strange or bottom quark. Also shown is the projection operator P_L which projects onto the left-handed (V-A) part of the top quark.

The single top quark is most dominantly produced in the t-channel, shown in figure 1.2. The Wtb vertex, both present at the production and the decay, is indicated with a red blob. In the t-channel a forward light jet is always produced (top right line in the diagram), called the spectator jet.

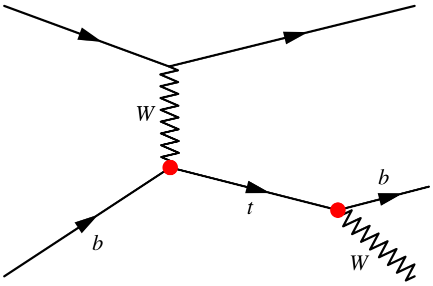

Figure 1.2: Diagram for the t-channel single top production and decay process. The Wtb vertex, both present at the production and the decay, is indicated with a red blob.

1.2.2 Decay and the W helicity states

The top quark decays almost exclusively to a b-quark ($V_{tb} \approx 1$) and a W boson, which subsequently decays to a charged lepton and the corresponding (anti-)neutrino[4]. Since the produced b-quark is effectively massless in comparison to the top quark, it has in practise an exclusively left-handed helicity. As a result, the right-handed helicity state of the W boson does not contribute to this decay based on the conservation of spin. This is schematically shown in figure 1.3, where the blue and red arrows indicate the direction of momentum and spin, respectively.

The decay of the top quark can be expressed in terms of the allowed W helicity fractions [23]:

$$\frac{1}{\Gamma}\frac{d\Gamma}{d\cos\theta_l^q} = \frac{3}{8}\left(1+\cos\theta_l^q\right)^2 F_R + \frac{3}{8}\left(1-\cos\theta_l^q\right)^2 F_L + \frac{3}{4}\sin^2\theta_l^q F_0, \tag{1.14}$$

where θ_l^q is the helicity angle defined as the angle between the W in the top rest-frame and the charged lepton (from the W decay) in the W rest-frame. Note that F_R, F_L and F_0 are fractions and that their sum must equal to unity.

When the spin axis of the top quark is known, as is the case in singly produced top quarks, a new set of coordinates can be constructed [24]:

$$\hat{q} = \frac{\vec{p_W}}{|\vec{p_W}|}, \quad \hat{N} = \frac{\vec{s_t}\times\vec{q}}{|\vec{s_t}\times\vec{q}|}, \quad \hat{T} = \hat{q}\times\hat{N}. \tag{1.15}$$

The vectors $\vec{p}_W$ and $\vec{s}_t$ are both defined in the rest-frame of the top quark and depict the direction of the W boson and that of the top quark spin, respectively. As a result, there are now three helicity angles defined as the angle between the lepton in the W rest-frame and either of these three unit vectors.

---

[4] Only the leptonic decay channels of the W boson are considered since charged leptons are better measurable as they leave a more characteristic imprint inside detectors.

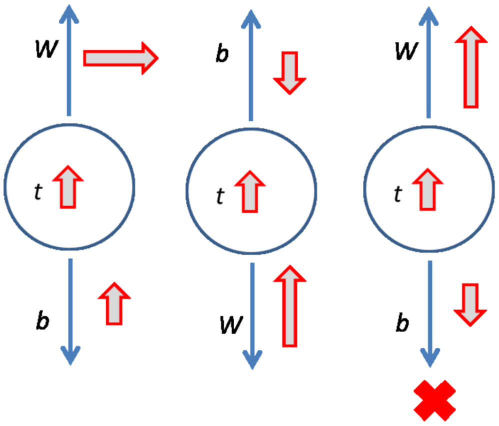

Figure 1.3: Allowed decay states of the top quark. The blue and red arrows indicate the direction of momentum and spin, respectively.

1.2.3 Polarisation

Due to the structure of the weak interaction, the polarisation of the top quark points to the direction of the spectator jet [22, 25]. Polarisation angles (θ_i^z) can be constructed that show correlations with the spin of the top quark. These angles are defined in the rest frame of the top quark between the spectator jet (S) and the direction of one of the decay products (i), as seen in figure 1.4.

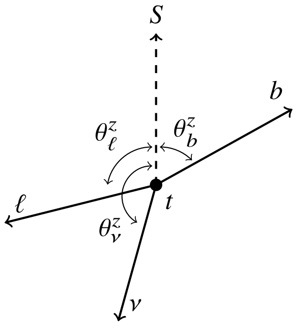

Figure 1.4: Definition of the polarisation angles in rest frame of the top quark.

$$\frac{1}{\sigma}\frac{d\sigma}{d\cos\theta_i^z} = \frac{1}{2}\left(1 + a_i P \cos\theta_i^z\right) \tag{1.16}$$

The differential expression for these polarisation angles is given in equation 1.16, where P denotes the amount of polarisation of the top and a_i the spin analysing power related to the corresponding decay product. For the charged lepton a_ℓ is close to one, indicating a nearly 100% correlation, as can be seen in figure 1.5.

The large spin analysing power of the charged lepton, which is a decay product of the W boson, can be understood by looking at the different allowed helicity states of the W boson. As shown in figure 1.3, only the longitudinal and left-handed helicity states are allowed in the decay of the top quark. It so happens that these states interfere with each other in such a way that the charged lepton becomes maximally correlated with the top polarisation [26]. This is shown in figure 1.6.

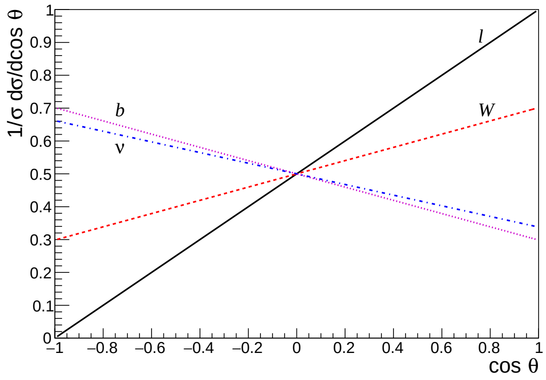

Figure 1.5: Angular correlations of the top polarisation [26].

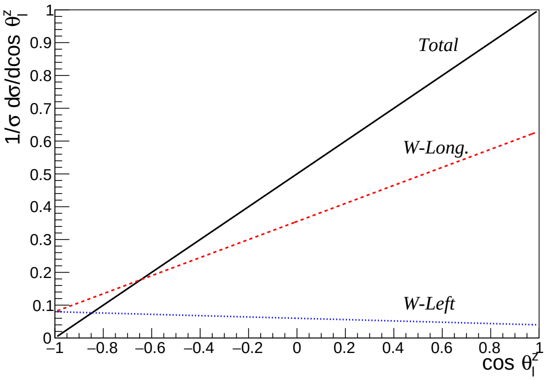

Figure 1.6: Interference between W helicity states [26].

The polarisation angle defined in equation 1.16 is one of the spin correlated angles that probes the production vertex. Again a new set of coordinates can be constructed [27]:

$$\hat{z} = \frac{\vec{p_j}}{|\vec{p_j}|}, \qquad \hat{y} = \frac{\vec{p_j} \times \vec{p_q}}{|\vec{p_j} \times \vec{p_q}|}, \qquad \hat{x} = \hat{y} \times \hat{z}, \tag{1.17}$$

where the vectors $\vec{p_j}$ and $\vec{p_q}$ are both in the top quark's rest frame and indicate the direction of the spectator- and of the initial quark, respectively. Since the initial quark cannot be known with certainty, the beam axis is used. As a result, there are now three polarisation angles defined as the angle between the charged lepton in the top quark's rest-frame and either of these three unit vectors.

The single top quark process is rich in the sense that angles can be defined that carry spin information. Most notable, three helicity angles, which are sensitive to the decay vertex of the top, and three polarisation angles which probe the production vertex.

1.3 Effective Field Theory

With the large amounts of data that the LHC is delivering, the era of precision physics is well on its way. This makes it possible to not only stress-test the Standard Model, but also to measure or constrain new physics. The framework of Effective Field Theory (EFT) provides the possibility to describe these unknown effects in a model independent way, while incorporating the symmetries of the SM.

1.3.1 The EFT Lagrangian

The EFT formalism augments the SM Lagrangian by including all possible higher dimensional operators with corresponding (Wilson) coefficients. Factors of $1/\Lambda$ are additionally present to maintain the correct dimension of the Lagrangian, i.e. four. The scale of new physics Λ, which can be seen as the mass of some unknown heavy BSM particle, is set to 1 TeV in this thesis.

$$\mathcal{L}_{\text{EFT}} = \mathcal{L}_{\text{SM}} + \sum_i \frac{C_i}{\Lambda} O_i^{[5]} + \sum_i \frac{C_i}{\Lambda^2} O_i^{[6]} + \dots \tag{1.18}$$

One can view effective operators as new allowed vertices in a Feynman diagram. A historical example of an effective theory is Fermi's contact interaction for beta decay. At low energies this model nicely describes the process, however at higher energies one could zoom in, so to speak, on the contact interaction to discover that there is an intermediate vector boson: the W (see figure 1.7).

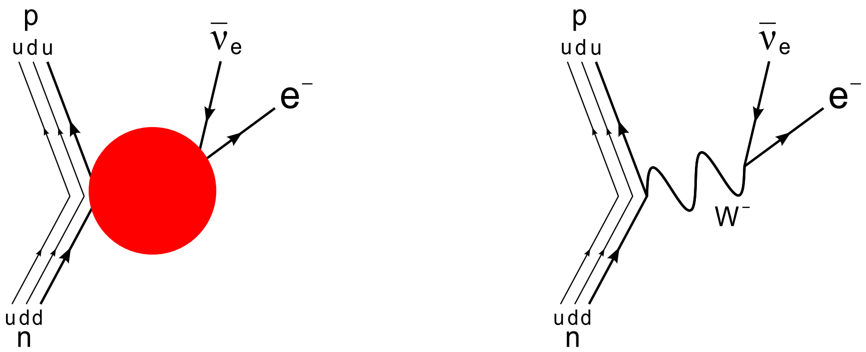

Figure 1.7: Historical example of an effective operator describing the contact interaction in beta decay before the W boson was discovered.

This highlights an important aspect of an effective theory: it is an approximation of the 'real' theory at a lower energy scale.

1.3.2 Extension to the single top sector

By their sheer number, it is impossible to include all possible effective operators at all dimensions. Assumptions to reduce this number are unavoidable. Nonetheless, one tries to be as inclusive as possible and only remove effective operators on good arguments.

The dimension 5 and 7 operators typically violate baryon and or lepton number [28], they will not be considered here due to strong existing bounds [29, 30]. The number of effective operators increases tremendously with increasing number of dimension [31]. In general it is assumed that the contribution from dimension-8 operators is sufficiently suppressed by their associated $1/\Lambda^4$ prefactor. The current focus is therefore exclusively on dimension-6 operators.

For single top quarks the production and decay both involve the Wtb vertex, as can be seen in figure 1.2. This narrows down the number of effective operators that can enter in the process. The dim-6 operators that can influence the single top process are given in table 1.2, together with the order in Λ at which they contribute. The square brackets [] indicate that the operator in question enters only at NLO in QCD.

Operator	$t\bar{t}$	single t	tW	tZ	t decay	$t\bar{t}Z$	$t\bar{t}W$
$O_{Qq}^{(3,8)}$	Λ^{-2}	Λ^{-4} [Λ^{-2}]	–	Λ^{-4} [Λ^{-2}]	Λ^{-4} [Λ^{-2}]	Λ^{-2}	Λ^{-2}
$O_{Qq}^{(3,1)}$	Λ^{-4} [Λ^{-2}]	Λ^{-2}	–	Λ^{-2}	Λ^{-2}	Λ^{-4} [Λ^{-2}]	Λ^{-4} [Λ^{-2}]
$O_{\phi Q}^{(3)}$	–	Λ^{-2}	Λ^{-2}	Λ^{-2}	Λ^{-2}	–	–
$O_{\phi tb}$	–	Λ^{-4}	Λ^{-4}	Λ^{-4}	Λ^{-4}	–	–
O_{tW}	–	Λ^{-2}	Λ^{-2}	Λ^{-2}	Λ^{-2}	–	–
O_{bW}	–	Λ^{-4}	Λ^{-4}	Λ^{-4}	Λ^{-4}	–	–
O_{tG}	Λ^{-2}	[Λ^{-2}]	Λ^{-2}	–	[Λ^{-2}]	Λ^{-2}	Λ^{-2}

Table 1.2: Effective operators in the single top sector. Showing at which order in Λ they contribute, where [] indicates NLO in QCD. Taken from [32].

In fact, at leading order in QCD and at $\mathcal{O}(1/\Lambda^2)$ only three operators with corresponding coefficients are required to parameterise new physics effects in the t-channel process: $O_{\varphi Q}^{(3)}$, O_{tW} and $O_{qQ,rs}^{(3)}$. Following the same notation and normalisation as in [33], their definitions are:

$$
\begin{aligned}
O_{\varphi Q}^{(3)} &= i\frac{1}{2}y_t^2\left(\varphi^\dagger \overleftrightarrow{D}^I_\mu \varphi\right)(\bar{Q}\gamma^\mu\tau^I Q), && (1.19)\\
O_{tW} &= y_t g_w(\bar{Q}\sigma^{\mu\nu}\tau^I t)\tilde{\varphi}W^I_{\mu\nu}, && (1.20)\\
O_{qQ,rs}^{(3)} &= \left(\bar{q}_r\gamma^\mu\tau^I q_s\right)\left(\bar{Q}\gamma_\mu\tau^I Q\right). && (1.21)
\end{aligned}
$$

As seen in table 1.2, more operators can contribute to the single top process. For example the operators involving right handed bottom quarks (O_{bW} and $O_{\phi tb}$), whose contributions are suppressed by the bottom mass at $\mathcal{O}(1/\Lambda^2)$. Additionally there is the four-fermion operator $O_{Qq}^{(3,8)}$, which has an octet colour structure. For this reason it can only contribute in the electroweak production of the top quark at NLO in QCD or at $\mathcal{O}(1/\Lambda^4)$. Another operator that can enter at NLO in QCD is O_{tG}, which represents a new vertex between top quarks and gluons. Both O_{tG} and $O_{Qq}^{(3,8)}$ will not be included here since they can be studied at tree level in $t\bar{t}$ events which leads to a better constraining power [32]. Finally there are operators that are not present in table 1.2, that could nonetheless enter in the single top production and decay. These involve flavour changing interactions [34] and four-fermion operators with right-handed light quarks [35]. They are however suppressed in the top sector if one assumes Minimal Flavour Violation [36] and will not be considered in this work.

The operators 1.19 and 1.20 modify the Wtb interaction in the following way:

$$
\begin{aligned}
\mathcal{L}_{Wtb}^{\text{dim}-6} = &-\frac{g}{\sqrt{2}}\bar{b}\gamma^\mu P_L t\, W_\mu \left(V_{tb} + \frac{C_{\varphi Q}^{(3)}y_t^2 v^2}{2\Lambda^2}\right)\\
&+ \frac{2\, g\, v\, y_t\, C_{tW}}{\Lambda^2}\bar{b}\sigma^{\mu\nu}P_R t\,\partial_\nu W_\mu + \text{h. c.}
\end{aligned}
\qquad (1.22)
$$

The coupling strength is denoted by g, and the top quark t, the bottom quark b and the W-boson W_μ fields are indicated. The Higgs doublet vacuum expectation value $v = 246$ GeV and y_t is the top quark Yukawa coupling. From now on the element of the CKM matrix V_{tb} is assumed to be equal to one. Note that the four-fermion operator of equation 1.21 introduces a contact $udtb$ interaction and does not contribute to the Wtb expression.

The impact of the three operators, $O_{\varphi Q}^{(3)}$, O_{tW} and $O_{qQ,rs}^{(3)}$, can already be seen by considering the partonic single top cross section. At $\mathcal{O}(1/\Lambda^2)$ this can be written schematically as in equation 1.23, where the k_i are known functions of θ, the angle between the incoming bottom quark direction and the top quark flight direction in the partonic centre-of-mass frame. It is important to be aware that $O_{tW} \neq O_{tW}^\dagger$ and thus its coefficient is a complex number which is expressed by two separate real coefficients: C_{tW} and C_{itW}.

$$
\frac{d\sigma_{ub\to dt}}{d\cos\theta} = \left(1 + \frac{C_{\varphi Q}^{(3)}y_t^2 v^2}{\Lambda^2}\right)k_1(\theta) + \frac{C_{qQ,rs}^{(3)}}{\Lambda^2}k_2(\theta) + \frac{C_{tW}}{\Lambda^2}k_3(\theta) + \frac{C_{itW}}{\Lambda^2}k_4(\theta) \qquad (1.23)
$$

An interesting feature of this production cross section is that each of the coefficients: $C^{(3)}_{\varphi Q}$, $C^{(3)}_{qQ,rs}$, C_{tW} and C_{itW} is associated with a specific angular dependence, enabling one to determine, or at least bound, the individual contributions experimentally.

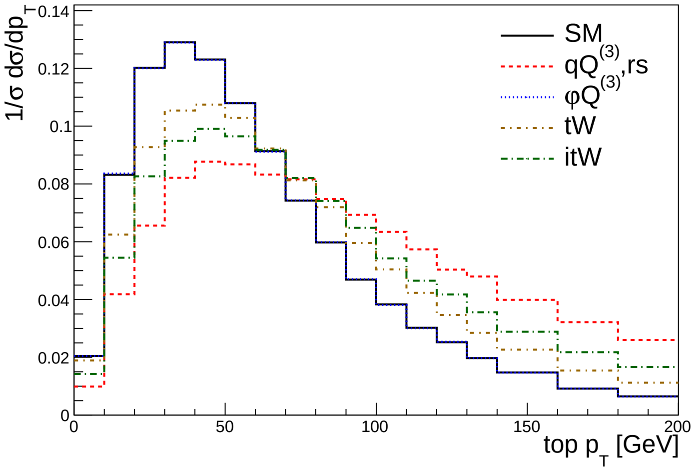

Figure 1.8: The normalised leading order parton-level differential cross section as a function of the transverse momentum of the top quark. The expectation of the SM together with the interference effects of the effective operators of interest are shown.

The operator $O^{(3)}_{\varphi Q}$ only modifies the magnitude of the Wtb interaction, as shown in equations 1.22 and 1.23, but does not change the angular dependence of the SM prediction. By contrast, the operator $O^{(3)}_{qQ,rs}$, with corresponding real coefficient $C^{(3)}_{qQ,rs}$, represents a four-quark contact interaction and noticeably affects the angular distribution of the top quark production angle. Of course, equation 1.23 addresses only the dominant lowest order parton process $u + b \to d + t$. Other partonic processes also contribute, but the different angular behaviour of the partonic cross section, predicted by the different operators, directly translates into different shapes of the top transverse momentum distribution. This is illustrated in figure 1.8, where the effect of $C^{(3)}_{qQ,rs}$ on the top p_T distribution is clearly distinguishable. Finally, the contributions of C_{tW} and C_{itW} have a shape again different from the other two operators.

1.3.3 CP violation in EFT

As discussed in section 1.1.3, a violation of the CP symmetry could be produced by a CP odd phase together with the interference between decays to a common final state. The operator O_{tW} can have an imaginary part, which resembles a phase. If this new operator exists it can interfere with the SM, completing all the ingredients for CP violation.

To show that this is the case, one needs to appreciate that the matrix element $\mathcal{M}$ is a complex number and that every observable contains the matrix element squared. The quantity to measure is therefore $|\mathcal{M}|^2 - |\bar{\mathcal{M}}|^2 \neq 0$, where $\bar{\mathcal{M}}$ indicates an anti-matter process.

The matrix element of the SM can be expressed in the following convenient way:

$$\mathcal{M}_{\text{SM}} = |\mathcal{M}_{\text{SM}}| e^{i\delta_{\text{SM}}}, \tag{1.24}$$

where $|\mathcal{M}_{\text{SM}}|$ is the amplitude and δ_{SM} is the so-called scattering- or strong phase. This phase arises from interactions between on-shell intermediate particles. Since the largest contribution comes from the strong interaction, which is CP conserving, it transforms even under CP [37]. The matrix element for the SM is therefore the same for particles and anti-particles:

$$\bar{\mathcal{M}}_{\text{SM}} = |\mathcal{M}_{\text{SM}}| e^{i\delta_{\text{SM}}} = \mathcal{M}_{\text{SM}}. \tag{1.25}$$

When an operator has an imaginary part, for example O_{tW}, things start to look different:

$$\mathcal{M}_{tW} = \mathrm{Re}[O_{tW}] + i \cdot \mathrm{Im}[O_{tW}] = |\mathcal{M}_{tW}| e^{i\theta_{tW}}. \tag{1.26}$$

The phase θ_{tW} is unknown and can in principle be CP odd. Also here a strong phase δ_{tW} should be included, making the full expression for the matrix elements:

$$\mathcal{M}_{tW} = |\mathcal{M}_{tW}| e^{i\delta_{tW}} e^{i\theta_{tW}}, \tag{1.27}$$

$$\bar{\mathcal{M}}_{tW} = |\mathcal{M}_{tW}| e^{i\delta_{tW}} e^{-i\theta_{tW}}. \tag{1.28}$$

When now the contributions of both the O_{tW} and the O_{SM} are taken into account, an asymmetry between matter and anti-matter can be present:

$$\mathcal{M} = |\mathcal{M}_{\mathrm{SM}}| e^{i\delta_{\mathrm{SM}}} + |\mathcal{M}_{tW}| e^{i\delta_{tW}} e^{i\theta_{tW}}, \tag{1.29}$$

$$|\mathcal{M}|^2 - |\bar{\mathcal{M}}|^2 = 4|\mathcal{M}_{\mathrm{SM}}||\mathcal{M}_{tW}| \sin(\delta_{\mathrm{SM}} - \delta_{tW}) \sin\theta_{tW}. \tag{1.30}$$

Note that not only the CP odd phase θ is important, also the scattering phase δ is necessary. For example, no CP violation will occur when the strong phase of the O_{SM} and the O_{tW} are the same.

The relation between θ_{tW} and the coupling strengths can be deduced from equation 1.26, leading to $|\mathcal{M}_{tW}| = \sqrt{|C_{tW}|^2 + |C_{itW}|^2}$ and $\tan\theta_{tW} = C_{itW}/C_{tW}$.

The discovery of CP violation in the top quark sector would have deep implications and could be an explanation for baryogenesis. The work presented in this thesis focuses therefore on the possibility of finding a non-zero value for C_{itW}.

Chapter 2

Monte Carlo event generation at NLO in QCD

This chapter is mainly focused on giving the reader a general idea of a Monte Carlo event generator and to introduce some key concepts. For a more complete review see for example [38] and references therein. The specific settings for the generation of the Monte Carlo simulated processes used in this work are given in chapter 3.

High energy collisions are simulated using a Monte Carlo (MC) sampling method. This technique not only solves multidimensional integrals, it also provides full information on the kinematics of the particles in the event. It is used for estimating the sensitivity of certain processes in real data and helps to optimise the selections for specific measurements.

The simulation of a proton-proton collision is divided in various steps, separated by their energy scale. The hard process contains the interactions of the partons. This is where, for example, the top quark is produced. All partons emit QCD radiation, this cascade of quark and gluon emissions are described by the parton shower. As a consequence of the strong coupling (α_s) increasing towards lower energies, the recombination of partons into hadrons starts to occur when the shower evolves towards lower energies. This, together with the decay of the unstable hadrons, is handled in the final step called the hadronisation. This chapter is structured as follows: section 2.1 gives a brief introduction into the MC method, the remaining sections cover the specific steps in the simulation of a proton-proton collision.

2.1 Monte Carlo method

The Monte Carlo method makes use of random numbers to solve multidimensional integrals, as well as to simulate processes. It is in particular suitable to describe particle collisions since they behave in a probabilistic manner and complicated integrals are involved in its calculations [40]. For instance, predictions for (differential) cross sections of the hard process (section 2.2) contain multidimensional integrals. Monte Carlo techniques sample the full phase space to numerically solve these integrals in an efficient manner, leading to an uncertainty that scales independently of the number of dimensions [41].

The technique mostly used in high energy physics is based on the VEGAS algorithm [42] and goes under the name of adaptive integration. It starts with a uniform multidimensional grid of sampling points and keeps track of the regions where the integrand is large. In the next iteration the grid is adapted so that more points are evaluated in those contributing regions. This procedure continues until an optimal grid is found from which efficient sampling points can be drawn. The calculated cross sections on this grid are used to probabilistically generate the event kinematics (section 2.2) and then add parton showers (section 2.3). The last step deals with the hadronisation and decay (section 2.4).

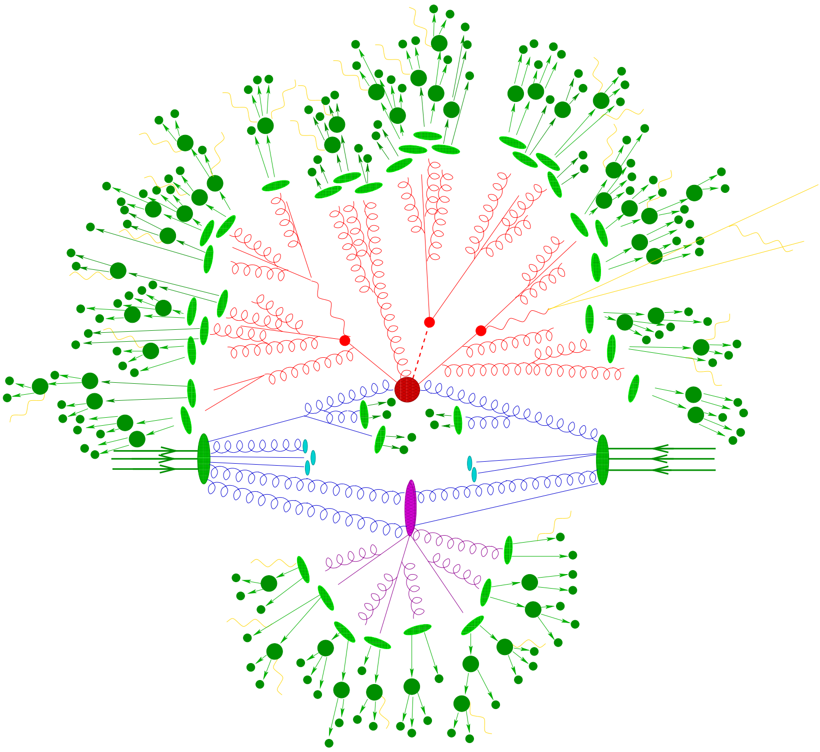

Figure 2.1: Illustration of a proton-proton collision simulated with a Monte Carlo event generator. The hard scattering process is indicated by the red blob in the middle, surrounded by the tree-like structure of the parton shower. The light green blobs signify the hadronisation of partons into hadrons. The decay of the unstable hadrons is indicated by the darker green blobs. In the lower part a purple blob can be seen which represents the underlying event. Taken from [39].

2.2 Hard process

Many effects are at play when considering proton-proton collisions. The partons inside the proton are not static and continuously interact with each other. These fluctuations appear to be almost frozen in comparison to the energy scale of the collision [43]. The calculation therefore factorises and the (differential) cross section of a proton-proton collision producing some final state can be written as [44, 45, 46]:

$$d\sigma = \sum_{a,b} \int_0^1 dx_a dx_b \, f_a(x_a, \mu_F) \, f_b(x_b, \mu_F) \, d\hat{\sigma}_{ab\to n}(x_a, x_b, \mu_F, Q), \tag{2.1}$$

where $f_a(x_a, \mu_F)$ and $f_b(x_b, \mu_F)$ are the parton distribution functions (PDF) which give the probability of finding a specific parton a or b with a certain momentum fraction x_a or x_b inside the proton. The partonic cross section (hard scattering process) is expressed by $d\hat{\sigma}_{ab\to n}$, where n stands for the final state particle(s) produced through the partons a and b with momentum transfer Q (the hard scale). The separation of the higher energy process ($d\hat{\sigma}$) from the lower ones ($f_a(x_a, \mu_F)$ and $f_b(x_b, \mu_F)$) happens, roughly speaking, at the factorisation scale μ_F which is usually taken to be of the same size as Q.

2.2.1 Parton distribution function

The PDF describes the parton density in the proton at an energy scale μ_F. It contains soft QCD effects that cannot be calculated using perturbative QCD. An important property of the PDF is that it is universal, it does not depend on the hard scattering processes. For this reason, the PDF can be extracted from dedicated experiments (electron-proton collisions, for instance) and used in other proton related calculations. The DGLAP equations [47, 48, 49, 50] are used to evolve the extracted PDF to the energy scale to be evaluated by the MC generation.

A careful approach is required when massive quarks, in particular the b-quark, are treated in the PDF. At a low energy scale the mass of the b-quark cannot be neglected in the hard interaction and the b-quark cannot be treated as a parton, leading to the 4 flavour scheme (FS). At a high energy scale, for instance the top quark production at the LHC, the b-quark can assumed to be massless and a 5 FS is an option [51].

2.2.2 Partonic cross section

The partonic cross section ($\hat{\sigma}$) contains all high energy physics and is proportional to $|\mathcal{M}|^2$, where $\mathcal{M}$ is computed from the sum of all Feynman diagrams. Calculations are based on perturbative QCD and suffer from divergences when going beyond leading order (LO). These divergences manifest themselves in two different types: the infrared (IR) and the ultraviolet (UV).

The IR divergences have so-called real and virtual components. The real component of the IR divergences refers to the soft and collinear splitting of a gluon, whereas the virtual component corresponds to the momentum of a particle in a loop becoming collinear or going to zero. As a matter of fact, both real and virtual terms cancel with each other according to the Kinoshita-Lee-Nauenberg theorem [52, 53]. To ensure this, partons should always be clustered in a IR safe jet to accommodate these cancellations and remain with a finite prediction [54].

The UV divergences are caused by unbounded momentum of virtual particles in loop diagrams. They are solved using the renormalisation of couplings and masses, which gives rise to another scale μ_R [55].

Both scales (μ_F and μ_R) are arbitrary and the predictions should not depend on them. Hypothetically this would be true if the entire perturbation sum in QCD is included, although this is in practise impossible. For fixed order calculations the impact of missing higher-orders is estimated by varying the scales (usually a factor of two is taken) and included as an uncertainty on the prediction. An expected decrease of scale dependence is observed when LO and next-to-leading order (NLO) calculations are compared. The choice for the values of the scales cannot be derived from first principles. They are usually set close to the physical energy scale of the process under study [38]. For example, in the production of the single top quark the mass of the top quark is most often used.

When intermediate unstable particles are part of the hard scattering process, such as the production and decay of the top quark, a technicality arises that is important to mention. A resonant divergence appears due to the finite width of the intermediate particle, specifically when its energy comes close to its on-shell mass value. There are two methods to properly handle this: the complex-mass scheme [56] and the narrow width approximation [57]. In the complex-mass scheme, as the name indicates, the mass of the unstable particle is continued in the complex plane solving the divergence while maintaining gauge invariance. In the narrow width approximation (NWA), another factorisation can take place when the total decay width (Γ) of the intermediate particle is much smaller than its mass. It allows to calculate the production cross section and decay branching ratio separately.

2.3 Parton shower

Partons emit QCD radiation which can further split into more partons creating a cascade (or shower), depicted by the red, blue and purple tree like structures in figure 2.1. These radiative effects involve QCD processes at relatively low energies that are best not described by the hard process but by the parton shower (PS). Monte Carlo techniques are in particular suitable to simulate the stochastic nature of the parton shower.

The process of (collinear) QCD radiation is described by the Altarelli-Parisi splitting functions [50]. Since the probability of an emission does not depend on the history of the parton, all splittings are independent and can be treated separately (iteratively). After each parton radiation, the energy decreases and the shower continues until the hadronisation scale (~ 1 GeV) is reached.

Unstable elementary particles, like the top quark and W boson, are decayed in the showering process. It is important to note, however, that in most parton shower implementations no spin information is conveyed to the decay products. If such information is required, as is the case in measuring the polarisation of the top quark, the unstable particles should be decayed before entering the parton shower. It could be part of the hard process or an intermediate program such as MADSPIN [58] can be exploited[1]. Especially when an NLO calculation is used for the hard process, MADSPIN offers an efficient solution to include the spin information in the MC prediction.

The combination of an NLO partonic cross section calculation with a parton shower could lead to the double counting of terms. For instance, the emission of an additional parton could be described by the parton shower or be part of the hard partonic scattering process. In order to not count these contributions twice, a certain matching scheme should be exploited. Usually the first parton shower emission is subtracted [59], leading to some events obtaining a negative event weight. As a consequence, the hard process calculation is tailored for a specific parton shower and only the sum of events after the parton shower provides reliable results.

2.4 Hadronisation and decay

Hadronisation is the process where partons combine to form hadrons, illustrated by the light green blobs in figure 2.1. This happens at such low energies that non-perturbative QCD models have to be employed to describe it. One method is the string model [38], where the colour connection between partons is represented by a string. The further away the partons move from each other, the more this string gets stretched and the larger the potential energy in the string becomes. After a certain distance (typically 1-5 fm [38]), the string breaks and partons are created which are connected via new strings. This procedure continues until all partons are confined into colourless hadrons. Most hadrons are unstable and decay inside the detector volume, indicated by the darker green blobs in figure 2.1. For their correct simulation, the branching ratios are taken from the Particle Data Book [60].

This concludes the simulation of proton-proton collisions with a Monte Carlo event generator. The produced final state particles, after hadronisation and decay, can in principle be observed. This stage of the generator is referred to as the “particle level”.

---

[1] It should be noted that MADSPIN only handles the decay, it is no substitute for the parton shower as no QCD emissions are included. Furthermore, it can only be used if the NWA holds as the production and decay processes are handled separately.

Chapter 3

Effective operators in t-channel single top production and decay

The phenomenological study in this chapter has been published as [1]. For readability, the paper is not presented in its entire form. The first two sections in the paper, as well as information on and the equations of the W helicity fractions and the top polarisation angles, will not be duplicated here as it is already discussed in chapter 1. Additionally some minor adjustments haven been made: the distributions of a non-zero C_{itW} are included in the figures and the normalised K-factor distributions are shown[1].

3.1 Introduction

This chapter assesses the effect of the limited set of dimension-6 operators, discussed in chapter 1, on single top quark production in the t-channel (for brevity only results for top production are shown, but the same observations can be made in anti-top production). It is done at next-to-leading order (NLO) in QCD, including top quark decay to W and b, both in the narrow top width approximation (NWA), and by producing the Wb directly, including non-resonant contributions. For general information on Monte Carlo event generation see chapter 2.

To study the impact of the three operators (defined in equations 1.19, 1.20 and 1.21) on single top production, the corresponding contributions are computed at LO and NLO matched to the parton shower (PS). The computation is performed within the MadGraph5_aMC@NLO (MG5_aMC) framework [61], and uses the NLO EFT implementation of [33]. While [33] produces results for stable top quarks, here also the top quark decays are considered . This can be achieved by either decaying the top-quark in MadSpin [58] or by following the procedure of resonance-aware PS matching presented in [62], to produce a Wbj final state. By decaying the W boson in MadSpin, the spin information is retained. The setup is fully differential and allows to assess the impact of NLO corrections as well as the impact of the operators entering either in the production or in the decay, or both, for any observable.

First the notation is fixed to facilitate discussion. Assuming one insertion of each operator, the matrix element for single top production can be written in the form:

$$\mathcal{M} = \mathcal{M}_{\rm SM} + \sum_i \frac{1{\rm TeV}^2}{\Lambda^2} C_i \, \mathcal{M}_i \,, \tag{3.1}$$

where the $\mathcal{M}_i$ are defined as having precisely one insertion of operator O_i in all possible ways. The new physics scale Λ is normalised in units of TeV. In physical observables, such as the production cross section and the top width, the matrix element enters squared. The squared amplitude takes the form:

$$|\mathcal{M}|^2 = |\mathcal{M}|^2_{\rm SM} + \sum_i \frac{1{\rm TeV}^2}{\Lambda^2} C_i \, 2{\rm Re}\left(\mathcal{M}^*_{\rm SM} \mathcal{M}_i\right) + \sum_{i\leq j} \frac{1{\rm TeV}^4}{\Lambda^4} C_i C_j \, |\mathcal{M}|^2_{i,j} \,, \tag{3.2}$$

---

[1] The published paper showed the unnormalised K-factor distributions.

assuming for simplicity real operator coefficients. From here onwards the contribution to the cross section from the interference term with the SM $\left(\propto 2\mathrm{Re}\left(\mathcal{M}^*_{\mathrm{SM}}\,\mathcal{M}_i\right)\right)$ will be denoted by σ_i, while the additional squared terms $\left(\propto |\mathcal{M}|^2_{i,j}\right)$ will be denoted by $\sigma_{i,j}$. In this notation, the cross section can be parameterised as:

$$\sigma = \sigma_{\mathrm{SM}} + \sum_i \frac{1\mathrm{TeV}^2}{\Lambda^2} C_i\,\sigma_i + \sum_{i\leq j} \frac{1\mathrm{TeV}^4}{\Lambda^4} C_i C_j\,\sigma_{i,j}. \tag{3.3}$$

The results for all three terms will be presented. Recall here the remark made in section 1.3.2 that the $O(1/\Lambda^4)$ terms represented by the $\sigma_{i,j}$ are far from complete. They are included only to estimate uncertainties in the EFT expansion.

3.2 Inclusive single top production

To start, the total single top production cross section for stable top quarks is computed for the relevant operators at LO and NLO for the LHC at 13 TeV. These results are also available in [33], but they are reproduced here in table 3.1 for completeness. In the computation of these results, the normalisation and factorisation scales, μ_R and μ_F, are both set to $m_t = 172.5$ GeV. The five-flavour number scheme is exploited, in combination with the usage of the NNPDF3.0 LO and NLO sets [63] for the LO and NLO predictions, respectively. A minimum of kinematic cuts are applied: $p_T^j > 5$ GeV and $|\eta_j| < 5$, where j stands for jets. To show the impact of the NLO corrections, table 3.1 presents the K-factors which are defined as the ratio $\sigma_{\mathrm{NLO}}/\sigma_{\mathrm{LO}}$ for each contribution.

	LO		NLO		
Operator	σ [pb]	$\frac{\sigma}{\sigma_{\mathrm{SM}}}$ [%]	σ [pb]	$\frac{\sigma}{\sigma_{\mathrm{SM}}}$ [%]	K
σ_{SM}	123	-	137	-	1.12
$\sigma_{qQ,rs^{(3)}}$	-92.3	-75.3	-102	-74.7	1.11
$\sigma_{\varphi Q^{(3)}}$	14.6	11.9	16.3	11.9	1.12
σ_{tW}	3.05	2.49	3.57	2.6	1.17
σ_{itW}	0	0	0	0	-
$\sigma_{qQ,rs^{(3)},\,qQ,rs^{(3)}}$	77.3	63.1	80.8	58.9	1.05
$\sigma_{\varphi Q^{(3)},\varphi Q^{(3)}}$	0.434	0.354	0.485	0.354	1.12
$\sigma_{tW,tW}$	0.758	0.619	1.03	0.752	1.36
$\sigma_{itW,itW}$	0.761	0.616	1.03	0.752	1.35
$\sigma_{qQ,rs^{(3)},\,\varphi Q^{(3)}}$	-5.49	-4.48	-6.08	-4.43	1.11
$\sigma_{qQ,rs^{(3)},\,tW}$	-2.34	-1.91	-2.84	-2.07	1.22
$\sigma_{\varphi Q^{(3)},tW}$	0.182	0.148	0.212	0.155	1.17

Table 3.1: Contributions to the cross section in pb for t-channel single top production at 13 TeV, as parameterised in equation 3.3. These values have been extracted from fitting equation 3.3, to a hundred computed cross sections with randomly chosen coupling strengths for the effective operators, both for LO and NLO separately. The statistical errors for each contribution in the table is below 1% except for the $\sigma_{qQij,tW}$ term at NLO, which is at 1.1%. The right-hand-side column shows the K-factor, which is defined for each row as the ratio of the NLO over the LO prediction. The subscripts tW and itW denote the contributions of the real and imaginary parts of O_{tW}, respectively.

It is observed that for the single top process the squared terms and interference between the operators, i.e. the $O(1/\Lambda^4)$ terms, are suppressed for coefficients of $O(1)$ for the O_{tW} and $O_{\varphi Q^3}$ operators but are not negligible for the 4-fermion operator. Taking its coefficient to be of order one a large cancellation between the interference and squared contributions is seen. Additionally, the K-factors vary considerably between the various operators and can be quite different from the SM contribution. This underlines the importance of including genuine NLO corrections in predictions, since a universal K-factor does not summarise the table. In the table also the contribution of the imaginary part of O_{tW} are included, which only enters squared at $O(1/\Lambda^4)$ as it does not interfere with the SM or the other operators. Its contribution will be discussed in detail in section 3.6.

Total cross-section results give a good first indication on the impact of the operators on the single top production process, but more information can be extracted by considering differential distributions. To demonstrate the effect of the operators on the differential distributions a set of benchmark scenarios are selected. The benchmark coupling values that will be used throughout this chapter are presented in table 3.2. The EFT analyses of [33, 64] are followed to ensure that the coupling values fall within the current limits. The effects on the inclusive cross section and the top width are also given for both LO and NLO. The predicted deviations from the SM predictions lie within the uncertainty of recent single top measurements: $\sigma = 156 \pm 35$ pb and $0.6 \leq \Gamma_{\text{top}} \leq 2.5$ GeV [65, 66, 67, 68]. The table also includes the scale uncertainties obtained by varying the central normalisation and factorisation scale by a factor of two up and down, and the PDF uncertainties. Note the significant decrease in the scale and PDF uncertainties going from LO to NLO, a well-known feature of NLO computations. At NLO the combined uncertainty is only of the order of 3%, in agreement with previous results [61]. For this reason the uncertainty bands will not be shown in the differential distributions, even though these can be straightforwardly computed with the setup.

The stable[2] top quark transverse momentum and pseudorapidity distributions for the SM and the benchmarks of table 3.2 are shown in figure 3.1. Computing these distributions, only one operator coefficient is allowed to be non-zero at a time. The interference with the SM as well as the square terms are included.

In the distributions it is seen that the 4-fermion operator in particular has an effect on the shapes in both the transverse momentum and rapidity distributions, leading to more energetic and more central tops. The impact of the other operator coefficients on the shape of these distributions is milder. It is also observed that the shape difference between LO and NLO (the K-factor distribution) has its largest effect in the regions where largest difference between $O^{(3)}_{qQ,rs}$ and the SM occurs, highlighting again the importance of NLO predictions for experimental analyses of this process.

---

[2] This top is selected based on its particle ID (i.e. in this example it is not reconstructed from its decay products), and therefore stable.

		LO		NLO	
Operator	Coupling value	σ[pb] ±scale ±PDF	Γ_{top} [GeV]	σ[pb] ±scale ±PDF	Γ_{top} [GeV]
SM	-	$123^{+9.3\%}_{-11.4\%} \pm 8.9\%$	1.49	$137^{+2.7\%}_{-2.6\%} \pm 1.2\%$	1.36
$O^{(3)}_{qQ,rs}$	-0.4	$172^{+8.7\%}_{-10.8\%} \pm 8.9\%$	1.49	$190^{+2.4\%}_{-1.8\%} \pm 1.1\%$	1.35
$O^{(3)}_{\varphi Q}$	1	$137^{+9.3\%}_{-11.4\%} \pm 8.9\%$	1.67	$154^{+2.3\%}_{-2.3\%} \pm 1.2\%$	1.52
O_{tW} (Re)	2	$132^{+9.3\%}_{-11.4\%} \pm 8.8\%$	1.83	$148^{+2.3\%}_{-2.5\%} \pm 1.2\%$	1.68
O_{tW} (Im)	1.75i	$125^{+9.2\%}_{-11.4\%} \pm 8.8\%$	1.51	$140^{+2.3\%}_{-2.5\%} \pm 1.2\%$	1.38

Table 3.2: The benchmark choices for the coupling values of the effective operators, together with the corresponding t-channel single top cross section and the width of the top quark. The scale and PDF uncertainties are shown, whereas the statistical errors, which are in the order of a few percent, are not given.

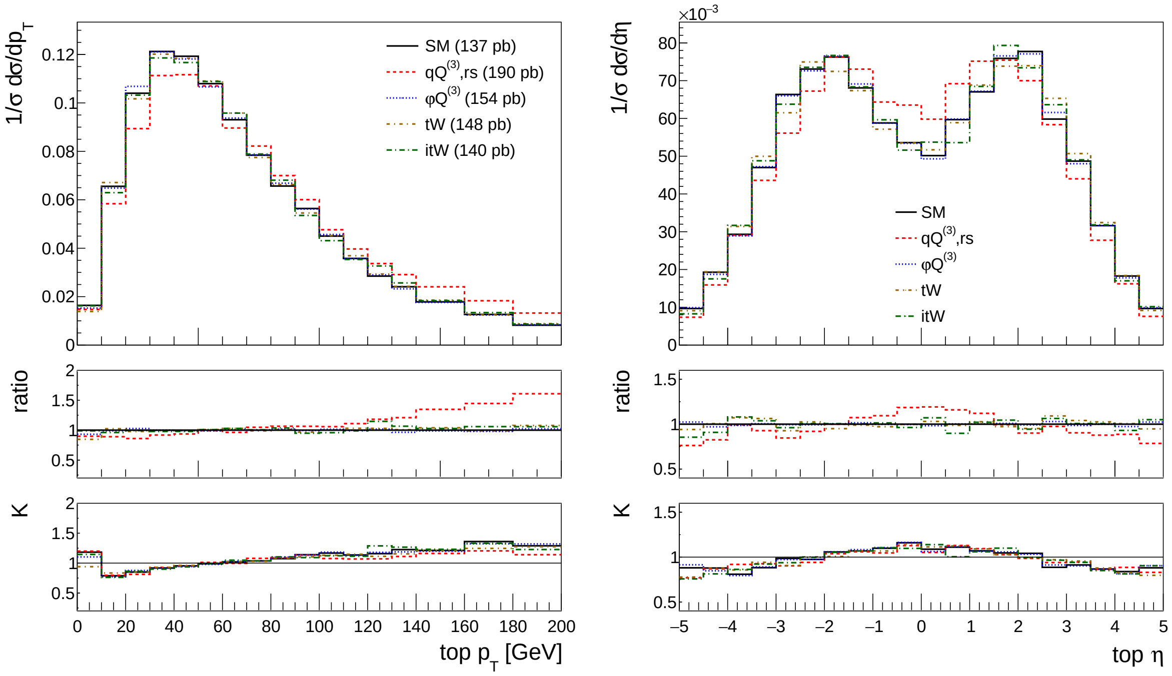

Figure 3.1: The NLO distributions of the stable top quark transverse momentum (left) and rapidity (right) for the SM and the four effective operator coefficients of interest set to the benchmark values of table 3.2. In the left figure the corresponding inclusive cross sections from this table are quoted. The ratio shown in the first inset is defined as the effect of the operator over the SM, the second inset shows the K-factor, the ratio of the NLO over the LO predictions.

3.3 Single top production and decay

To study the process in more detail and extract maximal information on the impact of the operators, the distributions of the top decay products should be considered. This requires studying the full process of $pp \to b\ell\nu j$, where it is assumed that the top quark decays leptonically. In such a computation several difficulties arise compared to the inclusive $pp \to tj$ computation.

The first being that in order to obtain a consistent single top event sample, the full process $pp \to b\ell\nu j$ has to be generated, including both the off-shell top effects and the interference with all the irreducible backgrounds. A NLO generation of the full process, though possible, is computationally too demanding for this purpose. Therefore approximations involving the presence of either an intermediate top quark or a W boson are adopted. However, one should ensure that no information about spin correlations is lost. Thus, the following samples are generated:

- The full matrix element up to the leptons ($b\nu lj$) in MG5_AMC (*fullchain*).
- Wbj production in MG5_AMC and decay the W in MADSPIN (*halfchain*).
- Single top production (tj) in MG5_AMC and decay the top and W in MADSPIN (*nochain*).

The differences between the three methods are investigated at LO, where all are straightforward to implement. In particular, given that one wishes to retain spin correlations in all three approaches, the differences involving the polarisation angle θ_i^z, defined in equation 1.16, are examined.

All three options show good agreement, as seen in figure 3.2. It has been verified to be the case for other observables as well. Given the level of agreement found at LO between the Wbj and $l\nu bj$ distributions, the *halfchain* method will be followed for the NLO results, i.e.: Wbj is produced and the W is decayed in MADSPIN, employing the relatively narrow W-width. A similar agreement is expected to hold at NLO, in particular as the leptonic decay of the W is not sensitive to higher order QCD corrections.

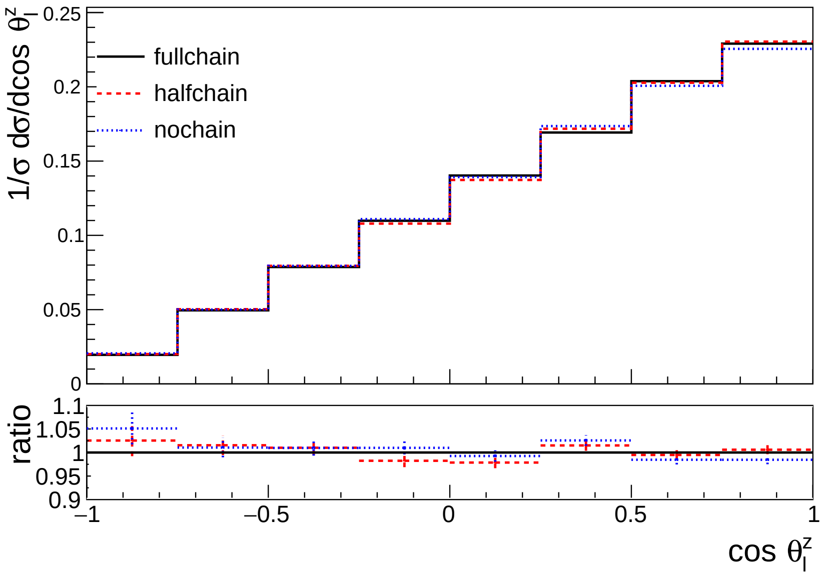

Figure 3.2: The SM top polarisation angle at LO for the three different generation options, as described in the text. The ratios with respect to the fullchain method are shown in the lower pane.

3.4 Treatment of top quark width and impact of multiple operator insertions

In addition to the difficulties already present in the SM calculation for single top production and decay at NLO, the following EFT related subtleties affect the computation as well:

i) The width of the top enters in the production of the Wbj final state. The effective operators affect the numerical value of this width, which has to be computed accordingly. Modifications of the width value are examined as well as its impact on the validity of the narrow width approximation for the top decay.

ii) By considering the Wbj production matrix elements, the effective operators can now enter both in top production and in top decay. Allowing more insertions in the amplitude generates higher order terms in $1/\Lambda^2$. These higher-order terms are expected to be suppressed but it will be checked explicitly. Studying the Wbj final state moreover implies that configurations without top quarks contribute. The dimension-6 operators can affect also these irreducible backgrounds, hence their contributions should be included and their impact studied.

These two subtleties are addressed in turn. i) As discussed in equation 3.2, the effect of one effective operator on the width of the top can be described by a second order polynomial $1/\Lambda^2$, e.g. for O_{tW} (real C_{tW}) the width takes the form:

$$\Gamma_{\text{top}}(C_{tW}) = \Gamma_{\text{SM}} + \frac{1\text{TeV}^2}{\Lambda^2} C_{tW}\,\Gamma_{tW} + \frac{1\text{TeV}^4}{\Lambda^4} C_{tW}^2\,\Gamma_{tW,tW}\,. \tag{3.4}$$

Figure 3.3 shows how the top width, computed at LO, varies as a function of the operator coefficient C_{tW}, demonstrating the quadratic functional dependence. It is important to stress here that there are experimental constraints on the value of the width by both CMS and ATLAS [67, 68], as well as theoretical proposals [69] to extract more information about the top width.

When the width is small compared to the total mass of the particle, one can factorise the total cross section for a given decay channel into the production cross section multiplied by the branching ratio corresponding to that particular decay channel. This narrow width approximation (NWA) rests upon the following approximation for the denominator of the squared top quark propagator [57]:

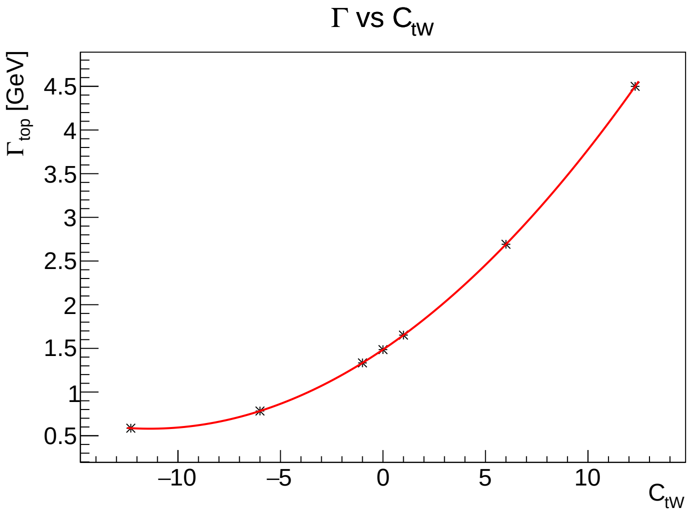

Figure 3.3: The top width as a function of the effective coupling C_{tW} for $\Lambda = 1$ TeV. The quadratic dependence on C_{tW} is predicted by equation 3.4. At the indicated points the width is computed for the corresponding C_{tW} values, while the line is a quadratic fit.

$$\frac{1}{\left(p^2 - M_{\text{top}}^2\right)^2 + M_{\text{top}}^2 \Gamma_{\text{top}}^2} \xrightarrow{\Gamma_{\text{top}}/M_{\text{top}} \to 0} \frac{\pi}{M_{\text{top}} \Gamma_{\text{top}}} \delta\left(p^2 - M_{\text{top}}^2\right). \tag{3.5}$$

The inclusive cross section of the single top production and decay to a W boson and a b quark is then approximated by:

$$\sigma(pp \to Wbj) \to \sigma(pp \to tj) \frac{\Gamma(t \to Wb)}{\Gamma_{\text{top}}} = \sigma(pp \to tj)\, \text{BR}(t \to Wb). \tag{3.6}$$

Since for top decays the branching ratio $\text{BR}(t \to Wb) \approx 1$, a direct way of testing the range of NWA validity in equation 3.6 is to calculate $\sigma(pp \to Wbj)$ at different numerical values of Γ_{top}, with SM couplings. This is shown in figure 3.4 where the linear dependence on $1/\Gamma_{\text{top}}$ can be observed for small Γ_{top}, whilst for $\Gamma_{\text{top}} > 50$ GeV the linear dependence breaks down. For non-excluded values of the operator coefficients the modifications of the width are moderate and therefore the NWA is expected to hold.

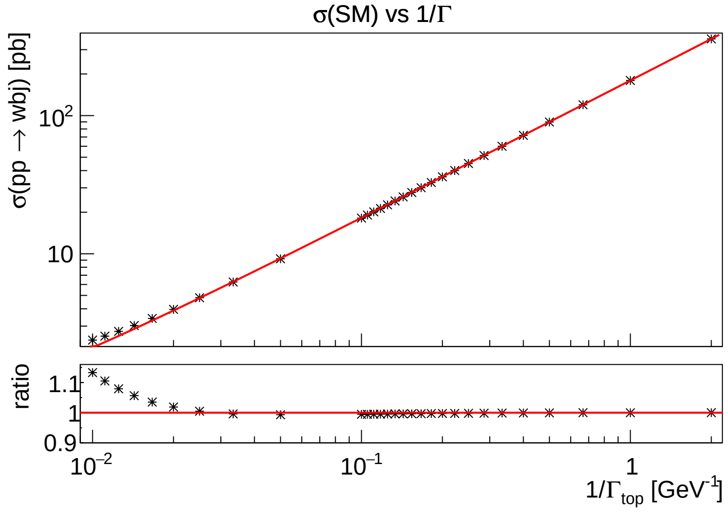

Figure 3.4: The SM cross section as a function of the width of the top. The NWA is valid when the relation is linear.

ii) The same interactions occur, at leading order, in the production and the decay of the single top quark, hence the amplitudes for the process $\sigma(pp \to Wbj)$ can contain up to two insertions of an effective operator (to be precise of O_{tW} or $O^{(3)}_{\varphi Q}$). The behaviour of the cross section as a function of the coefficient requires then a more complicated functional form than the one predicted by equation 3.3, in part due to the presence of more insertions, and in part due to the dependence of the top width on the coefficient, which enters in the Wbj calculation. The situation is however simplified in the NWA since the cross section for the production and the decay of a single top quark with two insertions of the effective coupling C_{tW} can then be written schematically as:

$$\sigma^{pp\to Wbj}_{\mathrm{EFT=2}}(C_{tW}, \Gamma(C_{tW})) \sim \left(\sigma_{\mathrm{SM}} + C_{tW} \cdot \sigma_{tW} + C^2_{tW} \cdot \sigma_{tW,tW}\right)_{(\mathrm{tj})}, \tag{3.7}$$

where $\Lambda = 1$ TeV to avoid notational clutter. This is also done for equation 3.8 below. The subscript (tj) is there to indicate that the dependence of the partial Wb width and total width on C_{tW} (and therefore in the branching fraction) cancels in equation 3.6. In other words, in the NWA the C_{tW} dependence is as for producing a stable top quark plus jet. Figure 3.5 compares the case where the width is fixed to its SM value (1.5 GeV) with the case where the width is computed based on the coefficient value. In both cases two insertions are allowed in the amplitude. When working in the NWA, the width, being a function of the coefficient, eventually leads to a quadratic dependence of the cross section on C_{tW} in 3.7. When one takes the width fixed there is no cancellation in the partial and total top width, and the dependence is quartic.

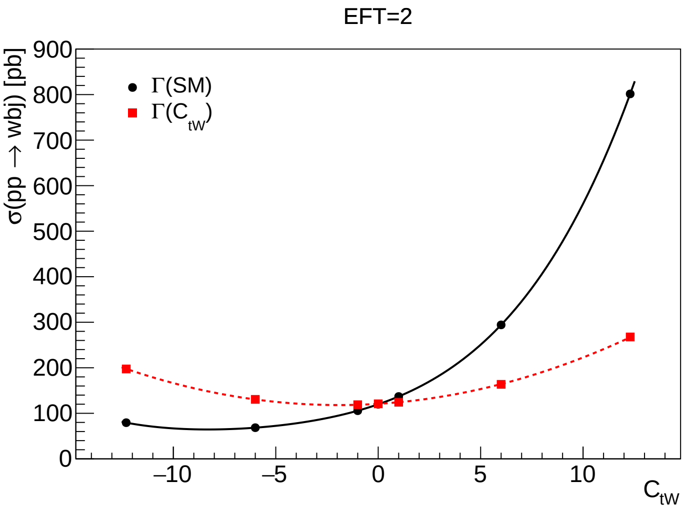

Figure 3.5: The cross section of the Wbj production as a function of C_{tW} with two EFT insertions for the width of the top fixed to the SM value of 1.5 GeV (quartic dependence), or computed according to the value of the operator (quadratic dependence).

When only one insertion of an effective coupling is allowed (still in the NWA), it can enter either in the production or in the decay. The simplified form of the cross section in this case becomes:

$$\sigma^{pp\to Wbj}_{\mathrm{EFT=1}}(C_{tW}) \sim \frac{\sigma_{\mathrm{SM}} + C_{tW}\,\sigma_{tW} + C^2_{tW}\,\sigma_{tW,tW}}{\Gamma_{\mathrm{SM}} + C_{tW}\,\Gamma_{tW} + C^2_{tW}\,\Gamma_{tW,tW}}, \tag{3.8}$$

where σ indicates that the Wbj final state is generated, with only one operator insertion. The Γ in the denominator indicates that the cross section is described by the narrow width approximation. Since the terms in the numerator are different in their $1/\Lambda^2$ dependence from the terms in the denominator, no cancellations occur. The impact of how the width is treated can be seen in figure 3.6 for the one-insertion calculations, where as expected a quadratic behaviour is observed when the width of the top is fixed, and a higher order polynomial is required to describe the behaviour when the width is computed with C_{tW} dependence.

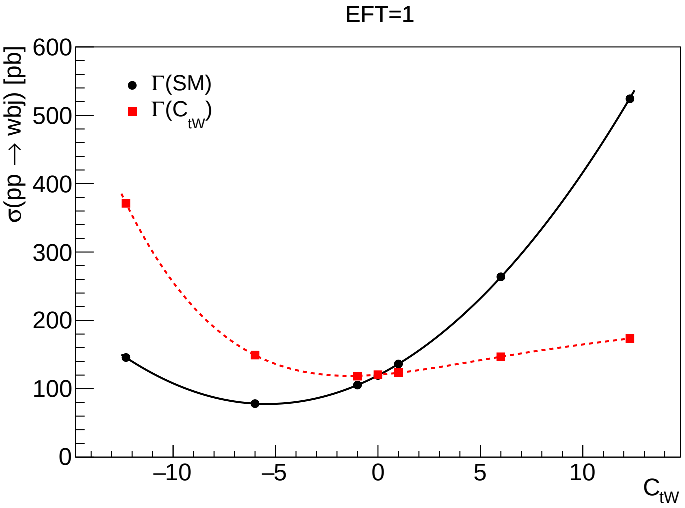

Figure 3.6: The cross section of Wbj production as a function of C_{tW} with one insertion with the width of the top fixed to the SM value (quadratic behaviour) or computed according to the value of the operator (higher-order polynomial).

Finally, figure 3.7 compares the behaviour of the total cross section with one operator insertion (EFT=1) or two insertions (EFT=2). It can be observed that for small values of the coupling, the linear term dominates and the cross sections coincide, as they only differ by higher order terms in $1/\Lambda^2$. Notice that figure 3.7 also shows that the production cross section $\sigma(pp \to tj)$ is very close to the Wbj cross section with two insertions of the couplings, as is expected from the NWA.

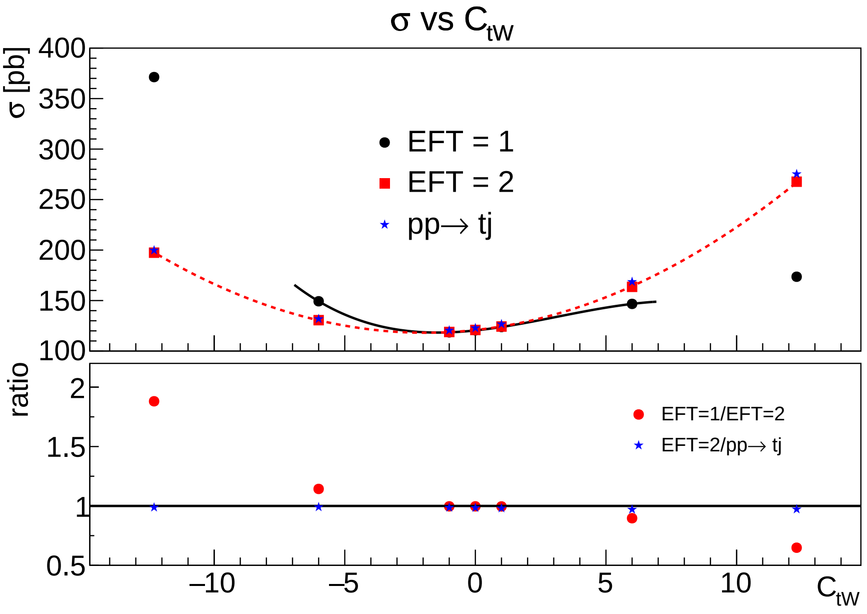

Figure 3.7: Comparing the different behaviour of the Wbj cross section with one C_{tW} insertion (EFT=1) or two C_{tW} insertions (EFT=2). Both effects have been discussed separately in figs. 3.5 and 3.6. Additionally the production cross section $(pp \to tj)$ is shown which is reproduced by Wbj with two insertions when the right width is taken into account.

In order to examine whether the conclusions reached so far apply to differential distributions as well, figure 3.8 shows the top polarisation angle, defined in equation 1.16, obtained for two different values of the coefficient for one and two EFT insertions. The left pane shows both EFT options for $C_{tW} = 1$. One can observe that the two distributions coincide within statistical errors. The right pane shows the case of $C_{tW} = 6$, here the impact of higher order terms are important and these cannot be described by a global normalisation factor as shown in the ratio inset. This indicates that higher order effects in the EFT can be non-negligible. Therefore, for consistency with the production cross section and to avoid missing large higher order effects, all distributions in the rest of this chapter have been obtained by generating Wbj allowing up to two EFT insertions, with the top width computed as a function of the coupling.

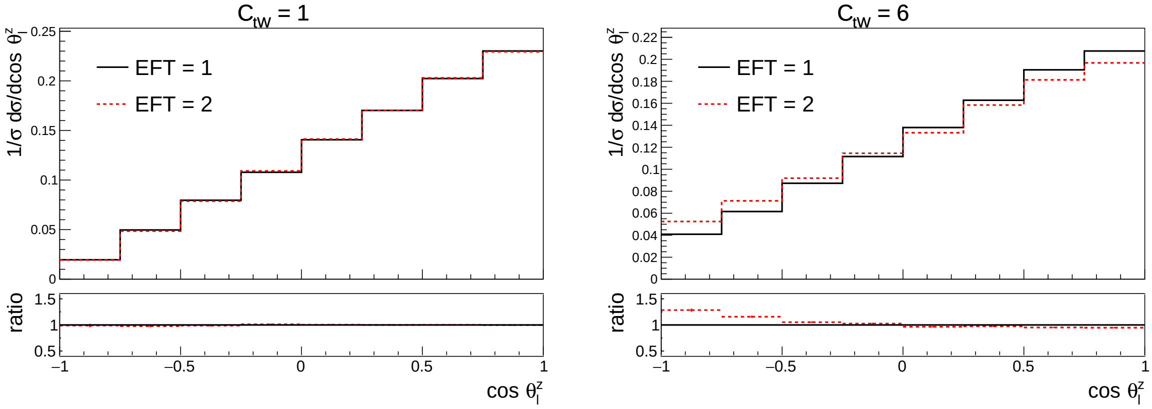

Figure 3.8: The top polarisation angle at LO with different values for the O_{tW} effective operator. On the left hand side results for $C_{tW} = 1$ are shown, whilst $C_{tW} = 6$ on the right hand side. The comparison between one and two EFT insertions is shown.

It should be mentioned here that the leading-order results have been validated with the ones discussed in [27] for the top-quark polarisation (P), analysing power (a_i) and lepton angular distributions. A detailed comparison has been performed by allowing all possible insertions of the operators and matching all parameters of the computation with the one implemented in the generator PROTOS [70], and perfect agreement was found.

3.5 Results at NLO

Having studied the various effects at LO, the next step is to compute the Wbj cross section at NLO in QCD in the presence of the dimension-6 operators. The W boson is decayed leptonically through MADSPIN, and PYTHIA8 [71] is used for parton showering and hadronisation. Since this setup also generates the irreducible backgrounds, a loose invariant mass cut is imposed on the Wb system, centred on the top mass $100\,\text{GeV} < M_{Wb\text{-jet}} < 250\,\text{GeV}$ [62]. Jet clustering is done using FASTJET [72] and the anti-k_t algorithm [73], with the jet radius parameter set to 0.4. All other generator settings and kinematic cuts are the same as in section 3.2.

The top quark transverse momentum and rapidity distributions are shown in figure 3.9 for the SM and the four benchmark operator coefficients, along with the ratio over the SM prediction and the corresponding K-factor. The top quark is now reconstructed from its semi-leptonic decay products, consisting of the hardest electron, the associated neutrino and a b-jet. The light spectator jet is identified as well. When more than one b-jet is present, the one yielding the best reconstructed top mass is chosen. The results in figure 3.9 are in excellent agreement with those in figure 3.1.

Other observables of interest are the kinematic distributions of the lepton and b-jet from the decay of the top, shown in figure 3.10. Their p_T distributions show a harder tail for the 4-fermion operator, whilst all contributions show a non-flat K-factor, with QCD corrections being larger in the high-p_T region, for both the b-jet and the lepton.

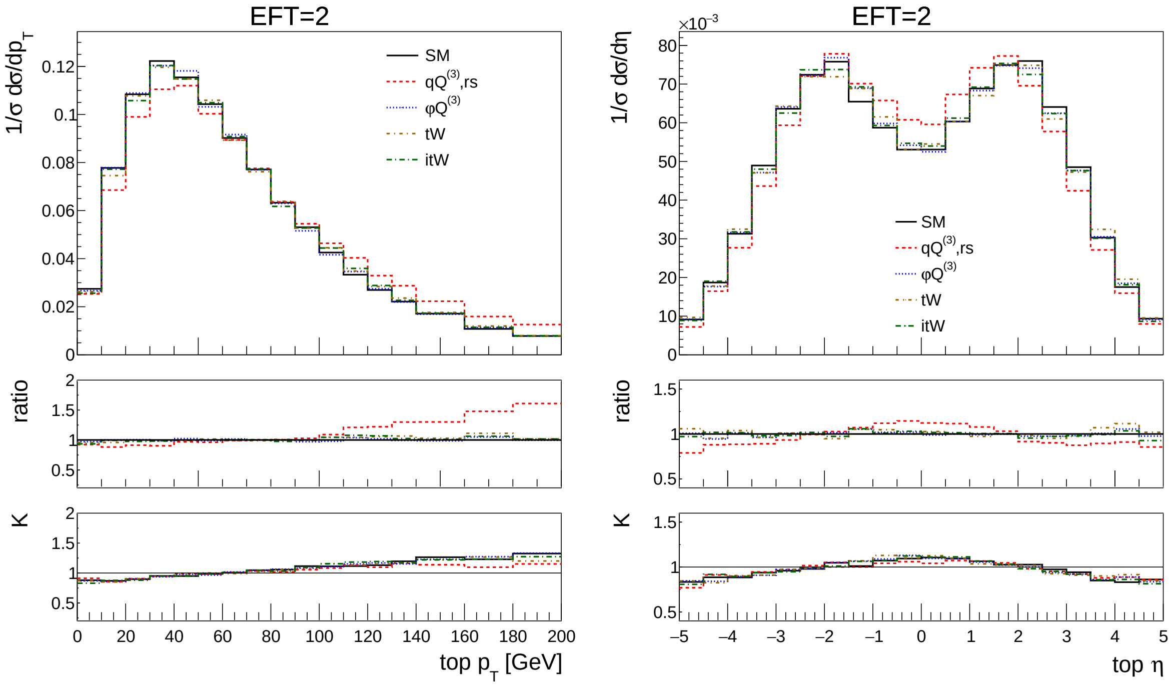

Figure 3.9: The NLO distributions of the reconstructed top transverse momentum (left) and rapidity (right) for the SM and the four effective operator coefficients of interest set to the benchmark values of table 3.2. The ratio shown in the first inset is defined as the effect of the operator over the SM, the second inset shows the K-factor.

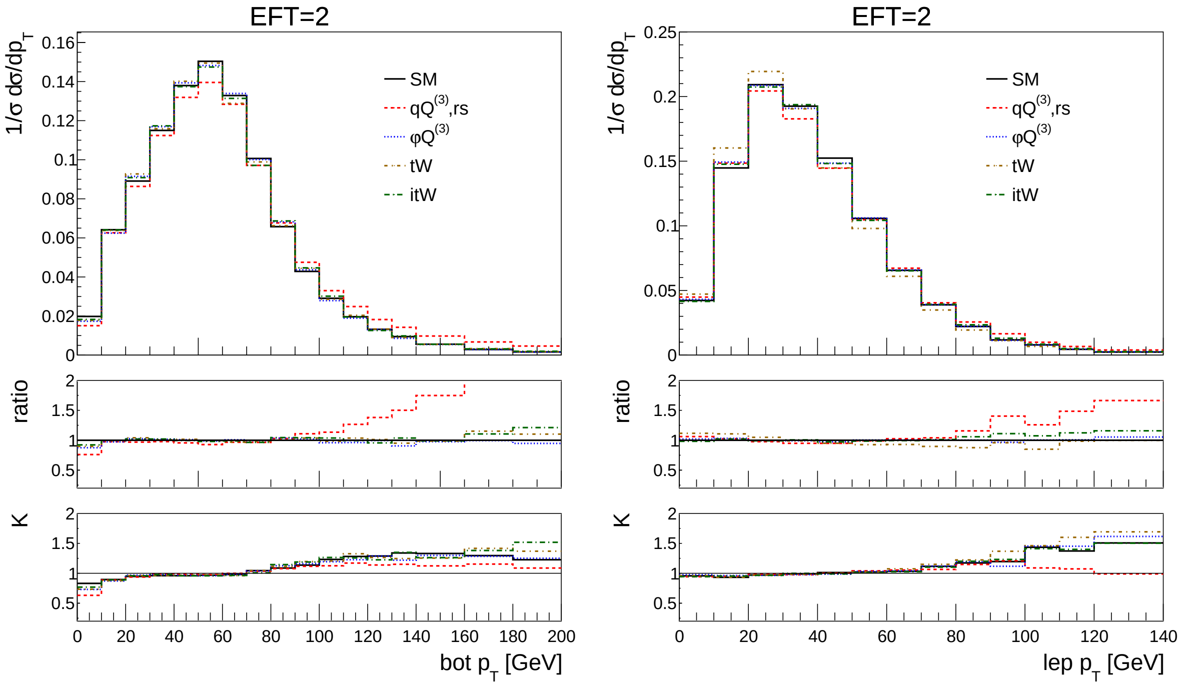

Figure 3.10: The NLO distributions of the b−jet (left) and electron (right) transverse momentum for the SM and the four effective operator coefficients of interest set to the benchmark values of table 3.2. The ratio shown in the first inset is defined as the effect of the operator over the SM, the second inset shows the K-factor.

As was discussed in section 1.2, a rich set of angular observables showing spin correlations can be exploited. In general, based on the choice of reference frame, it is possible to probe the production- and decay vertex of the single top separately. In any frame, a new set of coordinates can be defined based on the spin axis of the top. These additional coordinate axes provide the ability to construct other angles that contain spin information. For brevity, only the angular distributions that show the most sensitivity to the real parts of the effective operators will be presented in this section. The angular distribution that has sensitivity to the Wilson coefficient related to CP violation (C_{itW}) will be discussed in section 3.6.

The angle of the charged lepton with respect to the three axes defined in equation 1.17 is affected most by the polarisation of the top [26]. Here and in the remainder of this work will the subscript l, indicating the charged lepton, be left out in the notation of the polarisation angles for simplicity. Figure 3.11 (left) shows the NLO distributions for $\cos\theta_x$, where θ_x is the angle between the lepton and direction $\hat{x}$. Notice that the real coefficient of the dipole operator (C_{tW}) leads to a different distribution compared to the SM and the other operator coefficients.

The angle of the lepton in the W rest-frame with respect to the three axes defined in 1.15 probes the decay vertex. Figure 3.11 (right) shows the NLO distributions for $\cos\theta_l^q$ where the sensitivity to the real part of the dipole interaction comes mainly in the $\theta_l^q \sim \pi$ region.

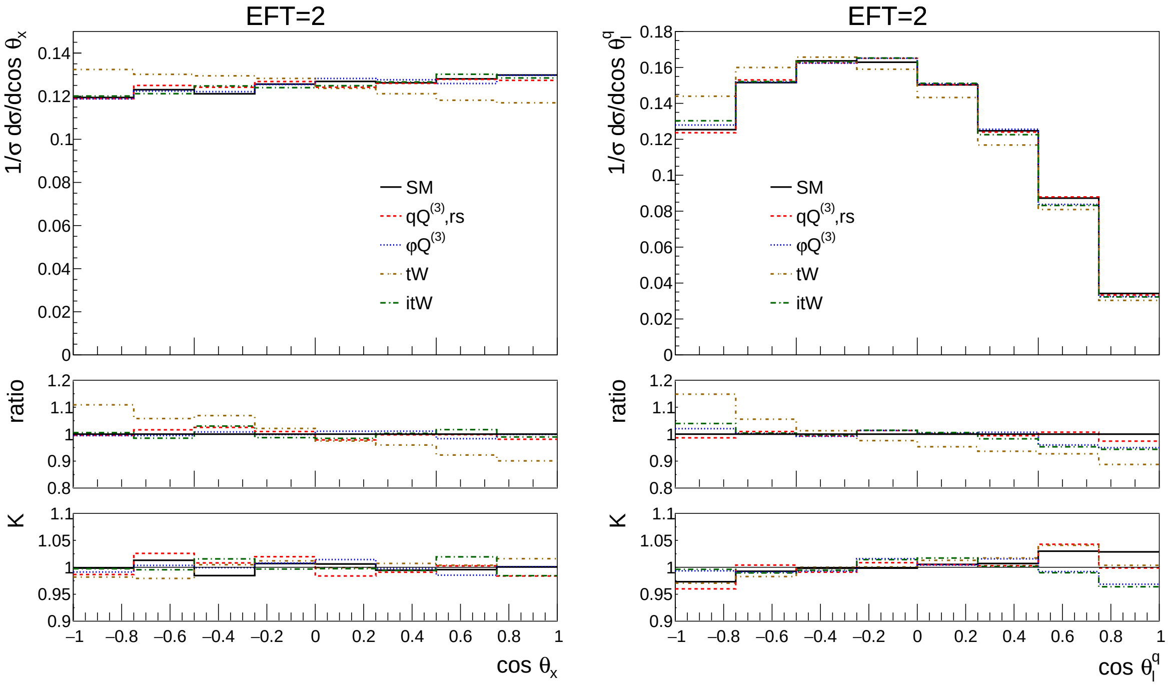

Figure 3.11: The NLO distributions of the top polarisation angle (left) and W helicity (right) for the SM and the four effective operator coefficients of interest set to the benchmark values of table 3.2. The ratio shown in the first inset is defined as the effect of the operator over the SM, the second inset shows the K-factor.

To show more realistic distributions, figure 3.12 shows the same observables as figure 3.11, only here additional cuts have been applied resembling the acceptance of the ATLAS detector. Namely, charged leptons must lie inside the $|\eta| < 2.47$ region and have a transverse momentum of at least 10 GeV, whereas jets should have a transverse momentum larger than 20 GeV and lie inside the $|\eta| < 4.5$ region. Note here that experimental selection cuts can potentially be more stringent in both rapidity, transverse momentum or angular separation observables of the different particles. The aim here is not to reproduce the setup of the experimental analyses, but just to provide an indication of how selection cuts can affect the sensitivity to the dimension-6 effects.

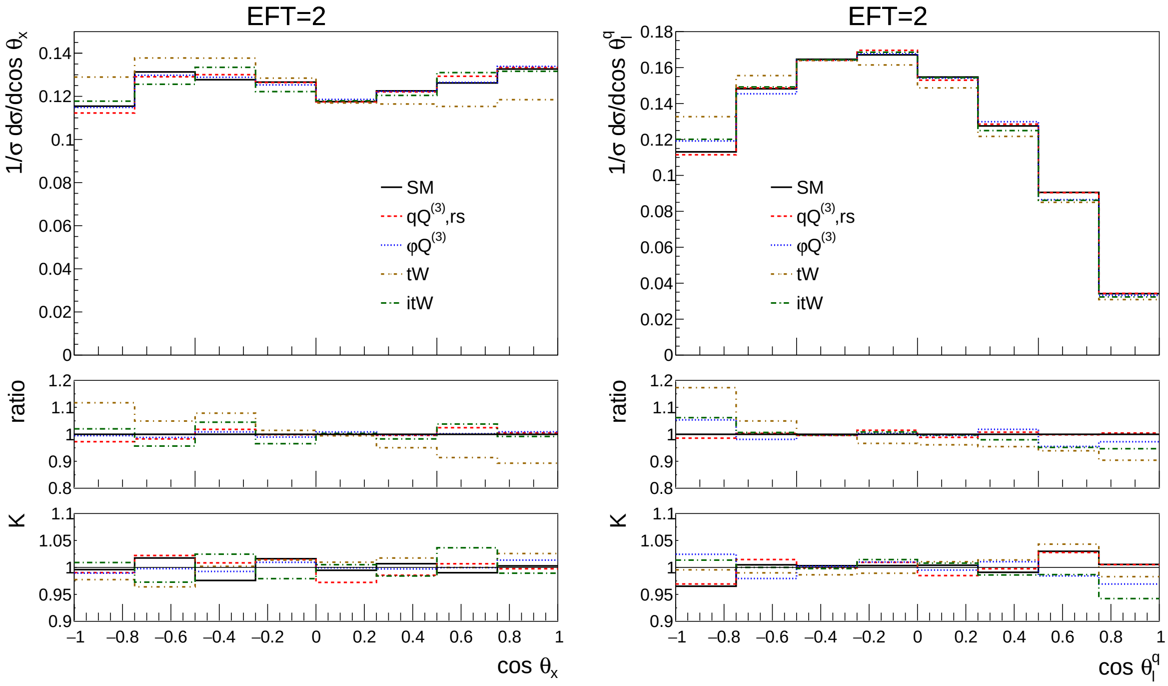

Figure 3.12: The NLO distributions of the top polarisation angle (left) and W helicity (right) for the SM and the four effective operator coefficients of interest set to the benchmark values of table 3.2. The ratio shown in the first inset is defined as the effect of the operator over the SM, the second inset shows the K-factor. Here additional cuts are applied on the leptons: $p_T^l > 10$ GeV and $|\eta^l| < 2.47$ and jets: $p_T^j > 20$ GeV and $|\eta^j| < 4.5$.

It is found that the additional cuts lead to a significant reduction of the statistics and to a weakened sensitivity to the dimension-6 effects for the angular observables considered here. Despite the reduction in the sensitivity, the shape difference in the $\cos\theta_x$ distribution (figure 3.12 left) between the real part of the dipole and other operators persists. This shape difference can be measurable as an asymmetry between positive and negative values of $\cos\theta_x$ as can be seen in figure 3.13.

Event samples where the operators were only allowed to enter in the production of the top quark have also been examined. Here it was observed that for the W helicity angles, equations 1.14 and 1.15, no deviation for the SM was observed. This validates that these angles probe the decay vertex only.

3.6 CP-violation in single top

In the SM CP violation is too small for baryogenesis, which motivates the search for new sources of CP-violation. Within the EFT, the coefficient of the O_{tW} operator can have an imaginary part, leading to a new CP-violating interaction, as was shown in section 1.3.3. This section studies how large this effect could be and identifies observables sensitive to it.

As discussed in [27], the polarisation angle $\cos\theta_y$ defined in equation 1.17 shows a sensitivity to the phase of O_{tW}. This can indeed be observed in figure 3.14, where an asymmetry is clearly visible for C_{itW}. The SM, charged current, four-fermion operator and real part of the dipole operator show no asymmetry in this distribution.

In order to focus on the effects of the imaginary part of O_{tW}, figure 3.15 shows results for a range of coupling values that are within the current global limits [64]. It is interesting to see that this observable is sensitive to both the size and the sign of C_{itW}. Additionally the asymmetry suggested in [74] has been studied, but it was found to be less sensitive than $\cos\theta_y$.

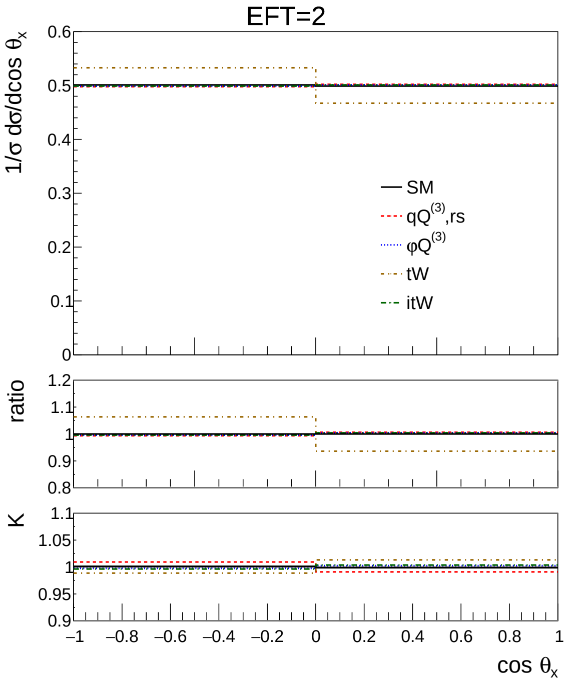

Figure 3.13: The asymmetry between positive and negative values of the top polarisation angle ($\cos\theta_x$) by presenting figure 3.12 (left) in 2 bins.

3.7 Conclusions

Single top production provides an excellent opportunity of probing top quark couplings. The SMEFT is a framework which allows one to parameterise deviations from the SM couplings in a consistent and model-independent way. Predictions in the SMEFT can be systematically improved by computing higher-order corrections. In this work single top production and decay at NLO in QCD, in the presence of dimension-6 operators, have been computed for the first time.

The impact of these QCD corrections has been studied, both at the inclusive and differential level. It was found that NLO effects affect both the total rates and the differential distributions in a non-trivial way, with different operator contributions receiving different K-factors. NLO effects can be large and are therefore needed to reliably predict the impact of the dimension-6 operators. All relevant contributions at $O(1/\Lambda^2)$ (and some $O(1/\Lambda^4)$ terms) were computed, and their relative importance examined.

Additionally the decay of the top was included, examining the validity of the NWA and the impact of the top width in computing results for the Wbj final state. It was found that the impact of the dimension-6 operators on the top width needs to be taken correctly into account to ensure that the Wbj and tj cross sections are consistent. Then the top production and decay at NLO matched to the parton shower using the resonance-aware matching within MG5_aMC was computed, including off-shell and interference effects. NLO distributions were obtained for both the top and its decay products for the SM and a series of benchmarks with non-zero operator coefficients. It was found that the weak dipole and four-fermion operators can lead to harder tails in the distributions.

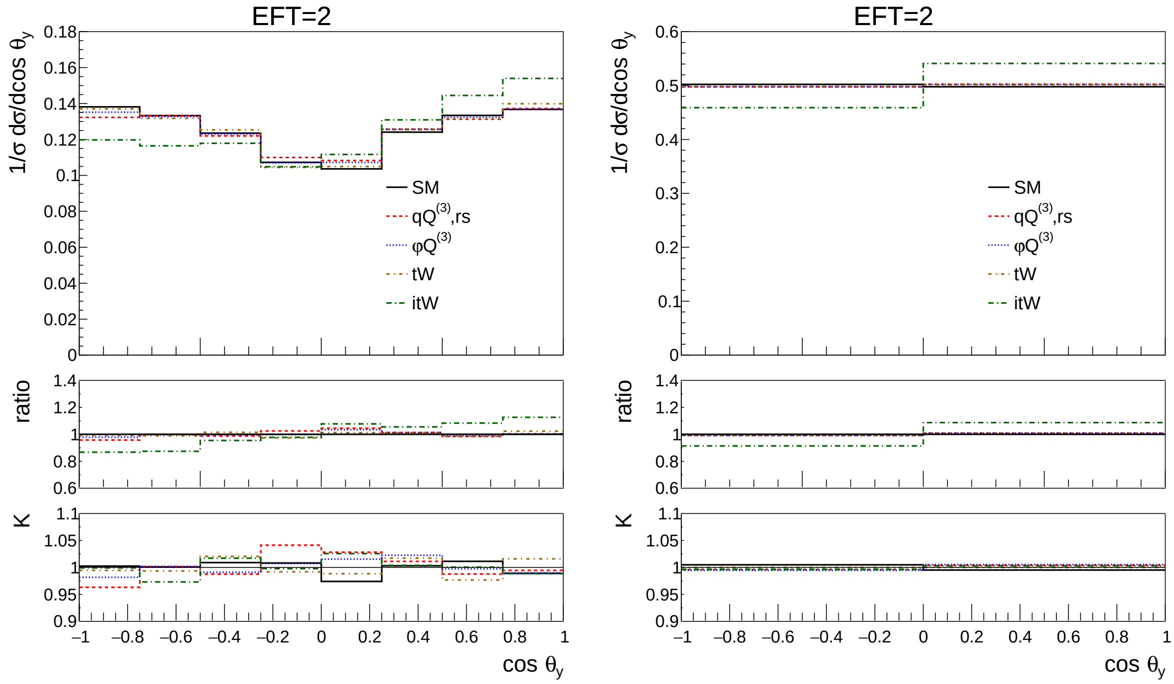

Figure 3.14: The NLO distributions of the top polarisation angle for the SM and the four effective operator coefficients of interest set to the benchmark values of table 3.2. On the left the shape of the distribution can be seen, on the right the same distribution is shown in two bins where the asymmetry is clearly observed. The ratio shown in the first inset is defined as the effect of the operator over the SM, the second inset shows the K-factor. Here additional cuts are applied on the leptons: $p_T^l > 10$ *GeV and* $|\eta^l| < 2.47$ *and jets:* $p_T^j > 20$ *GeV and* $|\eta^j| < 4.5$.

In order to fully exploit the power of spin correlations, a series of angular observables were explored that can be used to probe new physics couplings in either the production or decay of the top. These include the so-called polarisation angles and W helicity fractions. These angular distributions are found to be sensitive to different operators. The sensitivity becomes weaker when cuts are applied on the top decay products, but new physics couplings can still be probed by defining the corresponding asymmetries. Finally, CP-violating effects coming from the imaginary part of the dipole operator coefficient were considered and an angular distribution was studied that can be used to identify such an interaction.

The study in this chapter is an example of using an accurate and realistic simulation framework to compute deviations from the SM within SMEFT for a limited number of operators. The results can be used in combination with the experimental results to obtain reliable constraints on the operator coefficients as part of the on-going effort of EFT interpretations of LHC top-quark measurements [75]. That is also the target of the analysis in this thesis, where the focus is on the extraction of C_{tW} and C_{itW} from single top events measured with the ATLAS detector.

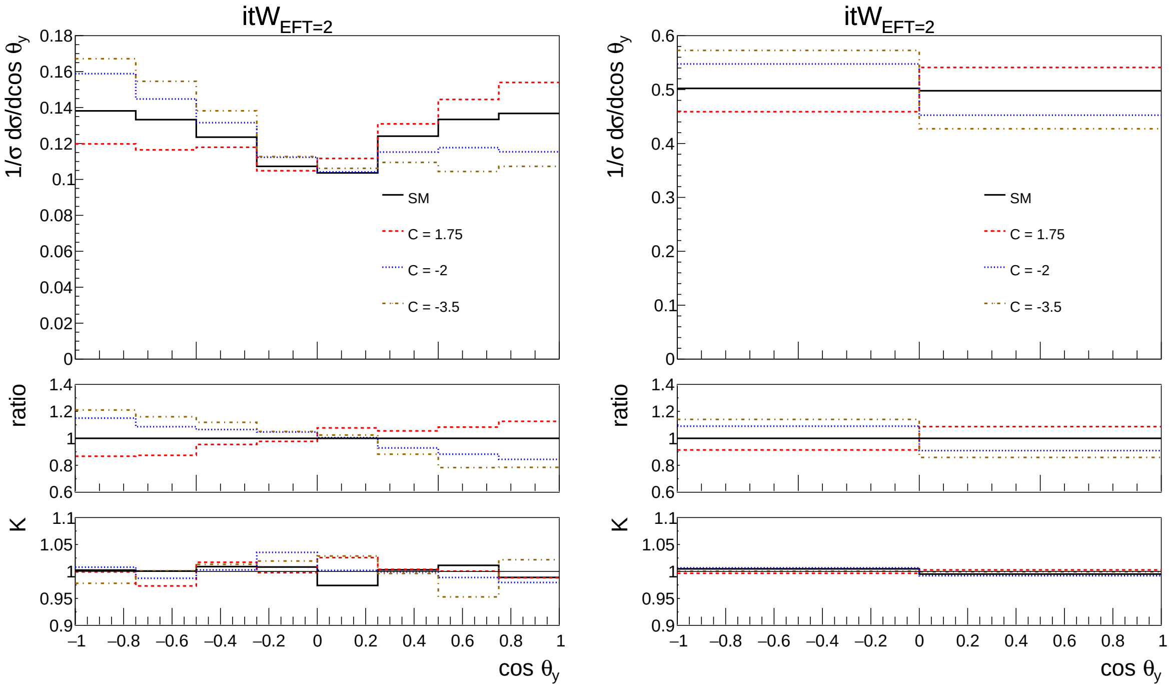

Figure 3.15: The NLO distributions of the top polarisation angle for the SM and different values for the imaginary part of O_{tW}*. On the left the shape of the distribution can be seen, on the right the same distribution is shown in two bins where the asymmetry is clearly observed. The ratio shown in the first inset is defined as the effect of the operator over the SM, the second inset shows the K-factor. Here additional cuts are applied on the leptons:* $p_T^l > 10$ *GeV and* $|\eta^l| < 2.47$ *and jets:* $p_T^j > 20$ *GeV and* $|\eta^j| < 4.5$.

Part II

Unfolding analysis

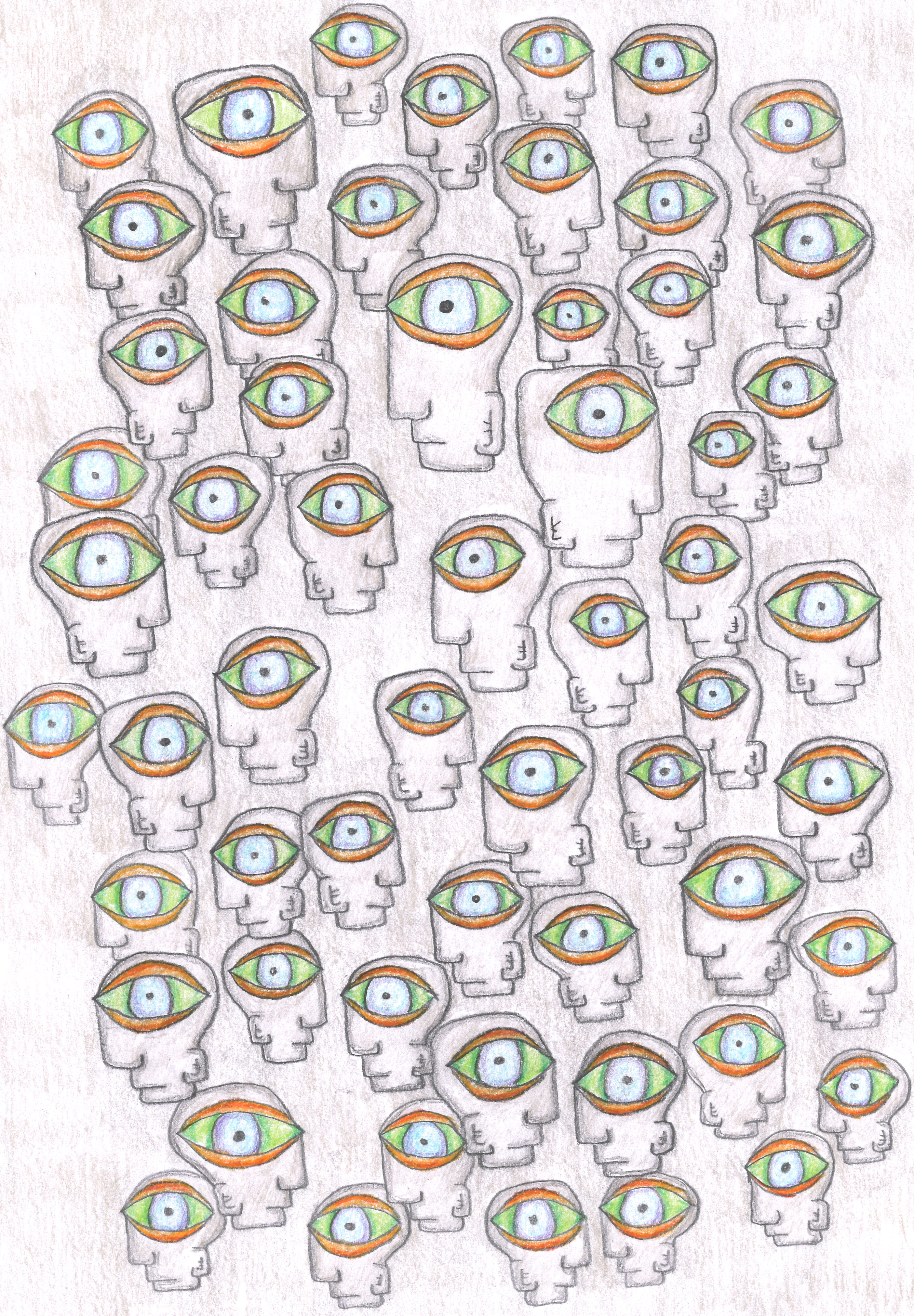

PJOT

Chapter 4

Instrumentation

4.1 CERN and the LHC

CERN (Conseil Européen pour la Recherche Nucléaire) is a European research center located on the border of France and Switzerland near the city of Geneva. It is a huge international collaboration with 23 member states and over 600 institutes and universities make use of its facilities. It is mostly known for hosting the largest particle accelerator in the world: the Large Hadron Collider (LHC).

The LHC is a hadron-hadron accelerator and collider built inside a tunnel of 27 km in circumference. It contains two separate rings with particle beams travelling in opposite directions. Most of the time the LHC is operated with protons, where in addition heavy ion beams (lead) can be run. The maximum designed luminosity for proton-proton collisions is $1 \cdot 10^{34} cm^{-2} s^{-1}$ at a center of mass energy of 14 TeV [76].

The accelerator complex at CERN is schematically shown in figure 4.1. The protons are extracted from a bottle of hydrogen gas and accelerated in a number of steps to reach their final energy. This procedure starts at the LINAC, goes through the Proton Synchotron Booster (BOOSTER), the Proton Synchotron (PS) and the Super Proton Synchotron (SPS) before finally reaching the LHC.

There are four points along the LHC where the two beams cross and collide. At these locations large detectors are stationed to study the collisions in detail. Two general-purpose detectors: ATLAS and CMS, both designed to investigate the full spectrum of in particular proton-proton physics, and two dedicated experiments: ALICE and LHCb, that focus on studying the quark gluon plasma and rare b-quark decays, respectively.

4.2 ATLAS detector

ATLAS (A Toroidal LHC ApparatuS) is the largest detector at the LHC. It is described in detail elsewhere [78][79][80], here only a general overview is presented.

The ATLAS detector is designed to measure and identify all particles in the full 4π solid angle. It makes use of an onion like structure consisting of separate sub-detector systems: the inner detector, two calorimeters and the muon spectrometer. Each subsystem is divided in a cylindrical barrel and two end-caps covering the forward regions. A superconducting solenoid magnet encloses the inner detector providing it with a 2 T axial magnetic field. The much larger superconducting toroid magnets produce a magnetic field between 0.5 and 1 T in the muon spectrometer. Figure 4.2 shows a cut-away view of the complete detector and figure 4.3 depicts the signatures of different particles when traversing through the subsystems of ATLAS.

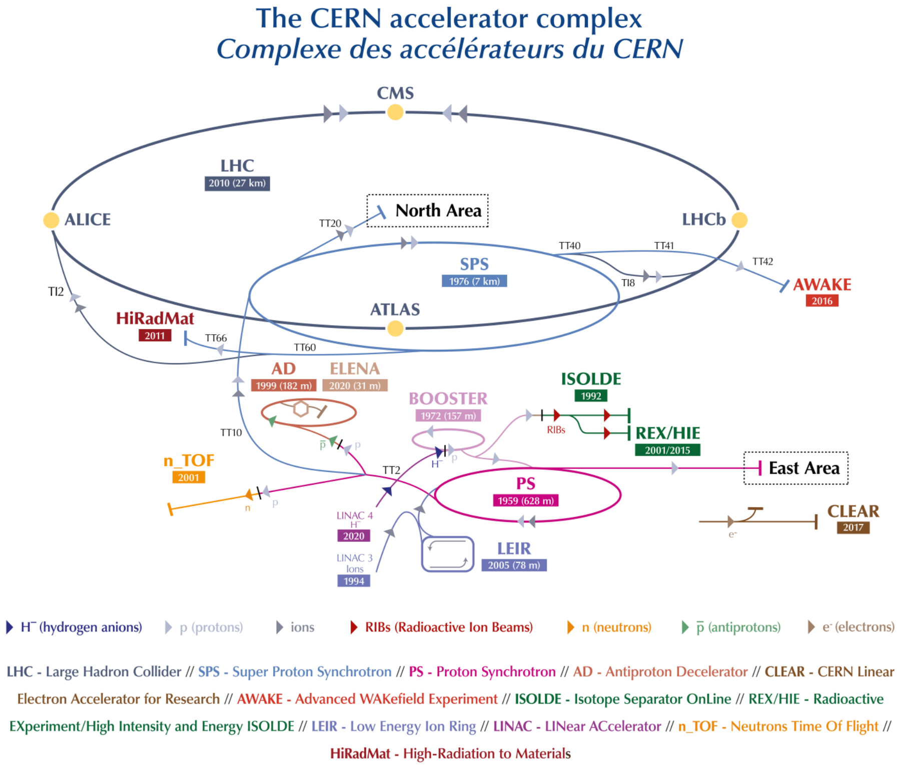

Figure 4.1: Accelerator complex at CERN. Taken from [77].

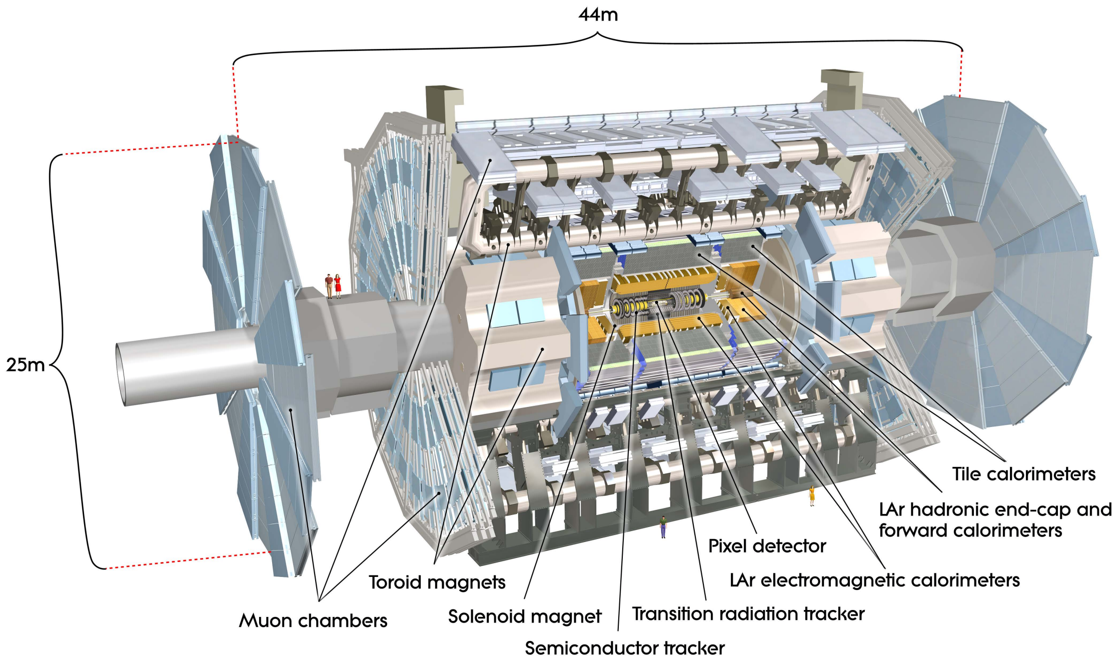

Figure 4.2: A cut-away view of the ATLAS detector [78].

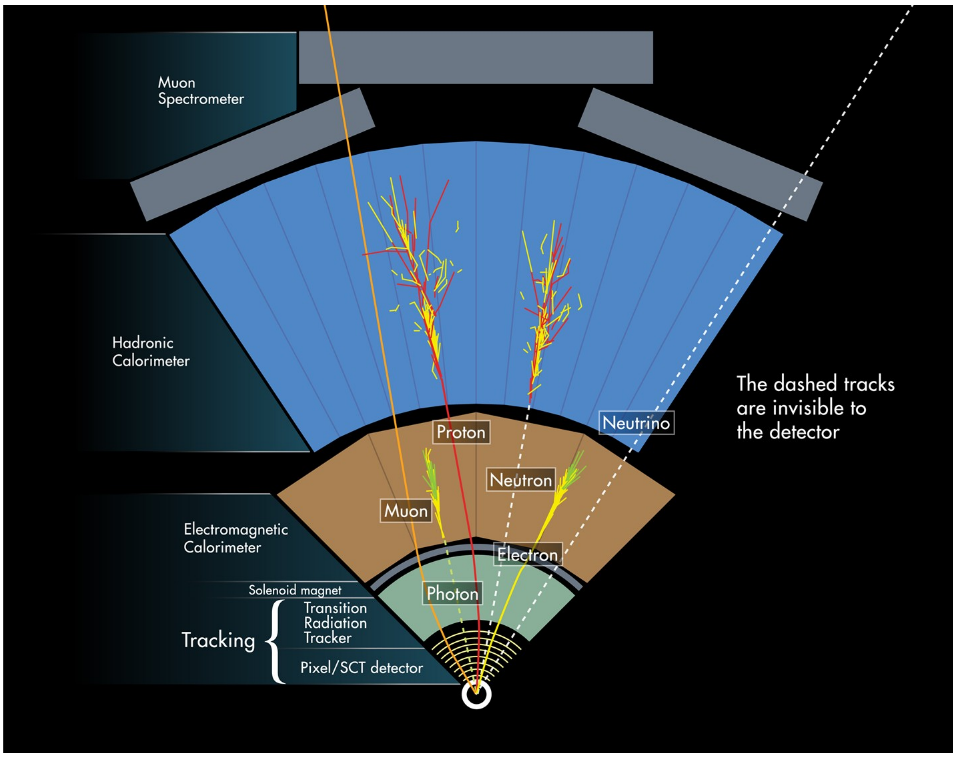

Figure 4.3: Particle signatures depicted in ATLAS. All sub detectors work complementary to provide the best identification of particles [81].

4.2.1 Inner Detector

The inner detector (ID) is the subsystem closest to the interaction point. It consists of four layers: the insertable B-Layer (IBL), silicon pixel detectors, silicon trackers (SCT) and transition radiation trackers (TRT). Charged particles leave a hit in each layer from which its track and point of origin (vertex) can be reconstructed. The magnetic field bends their tracks enabling a measurement of the particle's momentum.

The resolution of each layer is different due to the different granularity of the detector systems. Closer to the beam line the resolution is the highest, ranging from 8 μm for the IBL to 130 μm for the TRT [82, 83].

Of particular importance in this analysis is the identification of jets containing b-quarks, which arise from the decay of the top quark. The addition of the IBL improves the resolution on the primary vertex leading to a significant increase (factor 1.8) in light jet rejection when tagging b-jets with an efficiency of 60% [83].

4.2.2 Calorimeters

Calorimeters are used to stop and measure the energy deposit of incident particles. The sampling method is exploited, where alternating layers of passive and active material are placed after each other. The dense passive material acts as an absorber where only particles with enough energy can pass through to leave a hit in the active layer. There are two separate systems: the hadronic calorimeter and the electromagnetic (EM) calorimeter, both designed to contain either hadrons or electrons and photons, respectively.

The EM calorimeter is made out of liquid argon (LAr) and lead for the active and passive layers, respectively. It covers up to $|\eta| < 3.2$, from which the barrel ($|\eta| < 1.475$) and end-caps ($1.375 < |\eta| < 3.2$) are separated by inactive material ($1.37 < |\eta| < 1.52$) which can not be used for reconstructing electrons or photons.

The hadronic calorimeter contains steel for the passive layers and scintillating tiles or LAr for the active layers in the barrel and end-caps, respectively. It covers a total of $|\eta| < 4.9$, with the barrel ($|\eta| < 3.2$) and end-cap ($3.1 < |\eta| < 4.9$) regions slightly overlapping to be able to use the full coverage.

The measurement uncertainty related to measuring the energy of jets, for which the hadronic calorimeter is responsible, has a large contribution to the total uncertainty in this analysis. The reconstructed jets are corrected and calibrated making use of Monte Carlo simulations which increases the performance on the measurement of the jet energy [84].

4.2.3 Muon Spectrometer

The subsystem making up the outer layer of the ATLAS detector is the muon spectrometer (MS). It consists of four different kind of chambers: Monitored Drift Tubes (MDT), Cathode Strip Chambers (CSC), Resistive Plate Chambers (RPC) and Thin Gap Chambers (TGC). Each chamber contains a mixture of gas that gets ionised when a charged particle (muon) passes through. The RPC and TGC are designed for fast response and are used solemnly for triggering. The MS covers a total of $|\eta| < 2.7$ consisting of three cylinders in the barrel ($|\eta| < 1.05$) and four wheels in the end-cap ($1.05 < |\eta| < 2.7$).

The measurement of muons and their momentum are important in this analysis as they are needed to reconstruct the top quark. Additionally, the direction of the muon is correlated to the observable of interest: the polarisation of the top quark. The MS improves the momentum of muons measured by the inner detector, especially at higher momentum. For example, the MS is capable to measure muons of 1 TeV with an accuracy of 10% [85].

4.2.4 Trigger System

The rate at which the LHC delivers proton-proton collisions is orders of magnitude larger than the 1 kHz with which data can be written to permanent storage. A fast and efficient triggering system is therefore crucial. ATLAS uses a two level system: the Level-1 online trigger (L1) and the software based High Level Trigger (HLT). The L1 combines information from the calorimeters with hits in the RPC and TGC chambers in the muon spectrometer. It reduces the event rate to about 100 kHz. The HLT makes use of dedicated algorithms to reduce the rate further to a manageable stream.

In this analysis exactly one charged lepton is expected among the final state particles. For that reason the so called single lepton triggers are exploited. These triggers are optimised to fire when either one electron or one muon passes through the detector.

Chapter 5

Measurement of the top quark polarisation angles with the ATLAS detector

The experimental analysis on measuring the polarisation angles from the single top quark in the t-channel with data from the ATLAS detector has been presented at the LHCP-2021 conference and a conference note is under review. A paper by the ATLAS collaboration is in preparation. A summary of that work will be presented in this chapter focusing on the $\cos\theta_x$ and $\cos\theta_y$ distributions which are later used to analyse the effects of O_{tW}.

5.1 Data and Monte Carlo samples

The measurement has been done with data recorded by the ATLAS detector in the years 2015 till 2018, corresponding to a luminosity of about 139 fb^{-1} as can be seen in figure 5.1. In this period the LHC delivered proton-proton collisions, with 25 ns spacing between the bunches, at a centre of mass energy $\sqrt{s} = 13$ TeV.

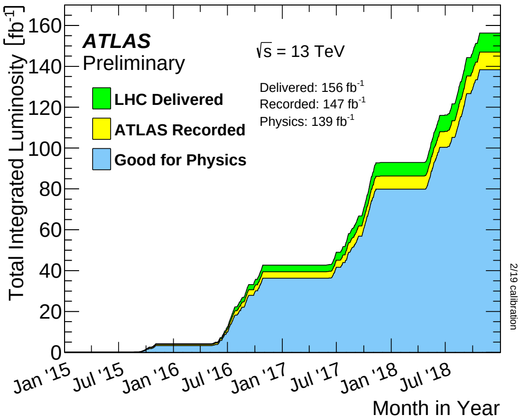

Figure 5.1: Total Integrated Luminosity and Data Quality in 2015-2018. Taken from [86].

Monte Carlo simulations are employed to study the detector response with respect to the signal sample and its background processes[1]. All top related samples (single top and $t\bar{t}$) are generated using Powheg for the hard process interfaced with Pythia8 for the showering and hadronisation. Processes that contain only vector bosons (W+jets or di-boson, for instance) are simulated with Sherpa[2]. The rare top processes with an associated vector or Higgs boson ($t\bar{t}Z$ and tHq for instance) are produced with aMC@NLO for the hard process together with Pythia8 for the parton shower, apart from $t\bar{t}H$ where Powheg is used for the hard process. All samples are generated at NLO precision.

5.2 Object definition

In this section the physical objects that are required to identify signal events, with a single top t-channel signature, are briefly described.

5.2.1 Triggers

Triggers are extremely important to obtain a manageable data stream. The triggers employed in this analysis are based on single charged leptons, the decay product of the W boson, and make use of both the hardware (L1) and software (HLT) trigger systems. Due to changes in the pile-up[3] conditions in the different years of data taking, corresponding trigger sets are used. The full trigger menu with their ATLAS names can be found in table 5.1, where data events that pass one of the listed triggers will be taken into consideration.

Year	Single-electron trigger	Single-muon trigger
2015	HLT_e24_lhmedium_L1EM20VH HLT_e60_lhmedium HLT_e120_lhloose	HLT_mu20_iloose_L1MU15 HLT_mu50
2016-2018	HLT_e26_lhtight_nod0_ivarloose HLT_e60_lhmedium_nod0 HLT_e140_lhloose_nod0	HLT_mu26_ivarmedium HLT_mu50

Table 5.1: The trigger selections, with their ATLAS names, per year of data taking. Data events that pass one of the listed triggers are taken into consideration. Taken from [87].

The electron triggers make use of the information from the EM calorimeter matched to a track in the ID. In 2015 a minimum of 20 GeV transverse energy (E_T) deposit is required at L1. At HLT a medium identification criterion is demanded, based on a likelihood discriminant, together with an E_T of at least 24 GeV. In order to increase the trigger efficiency of electrons with higher E_T, two more triggers are exploited where the requirement at L1 is relaxed. One with $E_T > 60$ GeV and medium identification, the other with $E_T > 120$ GeV and loose identification. In 2016-2018 a tight identification is demanded together with a loose isolation criterion and an E_T of at least 26 GeV. Again two additional triggers are used dedicated to higher E_T: one that demands $E_T > 60$ GeV and medium identification, the other $E_T > 140$ GeV and loose identification. The trigger efficiencies for electrons are around 95% [88].

The muon triggers combine information from the MS and the ID. In 2015 a p_T of at least 15 GeV is required at L1, combined with loose isolation and $p_T > 20$ GeV at HLT. In 2016-2018 the requirement at L1 is relaxed, but at HLT a tighter isolation is required (medium) with at least $p_T > 26$ GeV. In both periods of data taking a trigger for muons with $p_T > 50$ GeV is exploited to enhance the trigger efficiency of high energy muons. The trigger efficiencies for muons are around 70% in the barrel and 90% in the end-caps [88]. The differences in efficiencies are a consequence of the different geometric acceptance of the MS between the barrel and the end-caps[4].

---

[1] A process different from the signal that could resemble the signal signature in a measurement is commonly referred to as a background.

[2] Sherpa takes care of the hard process as well as the showering and hadronisation.

[3] Where pile-up refers to low momentum transfers proton-proton collisions.

[4] The calorimeters, used in the electron triggers, have a much better acceptance with respect to the MS and for that reason the efficiencies for triggering on an electron are higher.

5.2.2 Muons

The reconstruction of muons is most efficient (~97% [89]), since they penetrate the whole detector. The candidates are defined by combining information from the inner detector and the muon spectrometer. Only those that pass $p_T > 7$ GeV and $|\eta| < 2.5$ are considered. There is always a balance between background rejection and selection efficiency of a candidate. Three different working points are therefore classified: *Loose*, *Medium* and *Tight*, with increasing background rejection power ranging from 90 to about 98% [90]. Additionally criteria on the isolation of the candidate in a cone with radius $\Delta R = 0.2$ are requested[5]. Here the *Gradient* isolation working point is used, where the isolation efficiency increases with the p_T of the candidate.

5.2.3 Electrons

Electrons are reconstructed combining information from the tracker and the EM calorimeter. They are required to pass $p_T > 7$ GeV and $|\eta| < 2.47$, excluding the region between the barrel and the end-cap ($1.37 < |\eta| < 1.52$). Again three working points are classified: *LooseAndBLayerLH*, *MediumLH*, and *TightLH*, with increasing background rejection power ranging from 80 to about 95% [91]. Additionally a similar *Gradient* isolation working point is applied as is done for the muons.

5.2.4 Jets

Jets are reconstructed from the calorimeters making use of the anti-k_t clustering algorithm [73] with a jet radius of 0.4. Only those that pass $p_T > 20$ GeV and $|\eta| < 4.5$ are considered. Furthermore, a so-called jet-vertex-tagger (JVT) [92] discriminant is defined to identify jets coming from the hard scatter vertex as opposed to those coming from pile-up. It is based on the fact that the p_T sum of jet tracks from pile-up is close to zero. When imposing criteria on the JVT the suppression of pile-up jets with $20 < p_T < 50$ GeV and $|\eta| < 2.4$ becomes about 97%, while keeping the selection efficiency of hard scattered jets at 95%.

5.2.5 B-tagging

Jets containing a b-quark have a relatively long lifetime with respect to other jets and can thus be identified by a displaced decay vertex. The MV2c10 continuous algorithm [93] is used to tag these candidates with a threshold value of 0.94 that corresponds to an efficiency of 60%. It is based on a Boosted Decision Tree (BDT) with input variables from the vertex (impact parameters) and secondary vertex finding algorithms.

5.2.6 Missing Transverse Energy

To have a handle on the neutrinos in an event, the so-called missing transverse energy ($E_{\mathrm{T}}^{\mathrm{miss}}$) is defined as the negative sum of all the energy deposits in the calorimeters [94]. This includes electrons, muons, hight p_T jets and soft terms that have not been identified as jets due to their low momentum. The resolution of $E_{\mathrm{T}}^{\mathrm{miss}}$ ranges from about 15 to 20 GeV, depending on the pile-up activity [95].

5.2.7 Overlap Removal

The removal of overlapping objects is applied to prevent double counting of the same physical particle. Electron candidates that share a track with a muon are removed. Jets that are within a cone radius $\Delta R = 0.2$ with an electron are removed. Jets are also removed when they are within the same cone radius ($\Delta R = 0.2$) with a muon, unless three or more tracks originate from its primary vertex. Finally, to reduce the mis identification of a jet for an electron or muon, the charged lepton candidates that are within $\Delta R = 0.4$ cone radius of the surviving jets are removed.

---

[5] Where ΔR is defined as $\sqrt{\Delta\eta^2 + \Delta\phi^2}$ with η and θ indicating the pseudorapidity and azimuthal angle, respectively.

5.3 Event selection

The signal of interest contains a top quark, produced in the t-channel, that decays to a b-quark and a W boson. The W boson subsequently decays leptonically, either to an electron or a muon with the corresponding neutrino. As was shown in figure 1.2, additionally a spectator jet is present in the t-channel process. In this work top quarks as well as anti-top quarks are considered.

The are three different selection regions defined in this analysis: the signal region (SR) and two control regions (CRs). The SR is optimised to measure the top quark polarisation in the t-channel. The CRs are defined so that one background process is dominant, while being orthogonal to the other regions to prevent the double counting of events. They are used to evaluate the predictions of the MC simulations. All regions contain common selection criteria which are addressed in the preselection (PR). Table 5.2 summarises the definitions of all regions, the subsections below provide substantiating information.

5.3.1 Preselection region

To distinguish signal events from other scattering processes exactly one charged lepton is required with significant $E_{\mathrm{T}}^{\mathrm{miss}}$(for the neutrino) together with two jets of which one is b-tagged.

To suppress contributions from multijet events a requirement on the transverse mass of the charged lepton-$E_{\mathrm{T}}^{\mathrm{miss}}$system, defined in equation 5.1, is applied. Here $\Delta\phi(p_T(\ell), E_{\mathrm{T}}^{\mathrm{miss}})$ is the difference in azimuthal angle between the p_T of the charged lepton (ℓ) and $E_{\mathrm{T}}^{\mathrm{miss}}$.

$$m_T(l, E_{\mathrm{T}}^{\mathrm{miss}}) = \sqrt{2p_T(\ell)E_{\mathrm{T}}^{\mathrm{miss}}\left(1 - \cos\Delta\phi(p_T(\ell), E_{\mathrm{T}}^{\mathrm{miss}})\right)} \tag{5.1}$$

Additionally a more stringent requirement on the isolation of the lepton is applied when its position is further away from the jet with the largest p_T (also known as the leading jet). It is defined in equation 5.2, where $\Delta\phi(j_1, \ell)$ indicates the difference in the azimuthal angle between the leading jet (j_1) and the charged lepton.

$$p_T(\ell) > 50\left(1 - \frac{\pi - |\Delta\phi(j_1, \ell)|}{\pi - 1}\right)\mathrm{GeV} \tag{5.2}$$

5.3.2 Signal region

Additional requirements are applied, with respect to those in the PR, to purify the signal in the SR. To reduce the contribution from events without a (on shell) top quark, criteria on three sets of mass systems are imposed. Namely on the reconstructed mass of the W boson ($m_{\ell b}$), on the mass of the reconstructed top quark ($m_{\ell E_{\mathrm{T}}^{\mathrm{miss}} b}$) and on the mass of the jet-top quark system ($m_{j\ell E_{\mathrm{T}}^{\mathrm{miss}} b}$).

Two additional selection criteria have been defined by studying the simulations of the signal sample with respect to the backgrounds:

- A cut on the sum of all the values for the p_T of the final state particles (H_T).
- The so-called trapezoidal requirement that removes events which have a forward jet while the top is central. Its definition is given in equation 5.3, where the values have been obtained through optimisation. A visualisation of this selection criteria is given in figure 5.2, where red corresponds to signal events, blue to background events and green represents the trapezoidal requirement. Its effect is shown on the right, where it is observed that mostly signal (red) events remain.

$$\begin{aligned}
&\eta_j < (4\,\eta_{\ell E_{\mathrm{T}}^{\mathrm{miss}} b} + 10) \qquad \& \\
&\eta_j > (4\,\eta_{\ell E_{\mathrm{T}}^{\mathrm{miss}} b} - 10) \qquad \& \\
&(\eta_j > (0.44\,\eta_{\ell E_{\mathrm{T}}^{\mathrm{miss}} b} + 2) \quad \mathrm{OR} \\
&\eta_j < (0.44\,\eta_{\ell E_{\mathrm{T}}^{\mathrm{miss}} b} - 2))
\end{aligned} \tag{5.3}$$

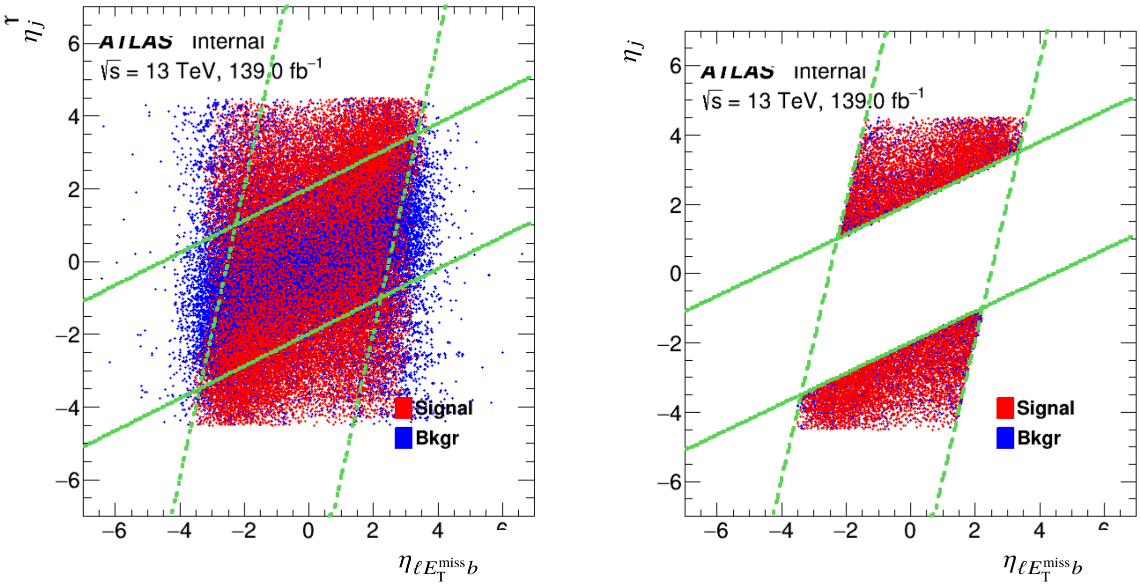

Figure 5.2: The two dimensional correlation between η_j and $\eta_{\ell E_{\mathrm{T}}^{\mathrm{miss}} b}$ with the trapezoidal requirement (equation 5.3) overlain in green and applied on the right. Taken from [87].

5.3.3 Control regions

Two specific control regions are defined for the most dominant background processes:

- The $t\bar{t}$ control region requires the same criteria as the PR except that both jets must be b-tagged and inside $|\eta| < 2.5$.
- The W+jets control region is basically the anti-selection region as it requires the PR with additionally all the criteria from the SR but then reversed.

5.3.4 Summary

Table 5.2 summarises the definitions of all regions. For explicit information see the subsections above that correspond to specific selection regions.

Preselection region	Signal region	$t\bar{t}$ control region	W+jets control region
=1 charged tight lepton ($p_T > 30$ GeV and $\lvert\eta\rvert < 2.5$)			
Veto secondary low-p_T charged loose leptons ($p_T > 10$ GeV and $\lvert\eta\rvert < 2.5$)			
=2 jets ($p_T > 30$ GeV and $\lvert\eta\rvert < 4.5$; $p_T > 35$ GeV within $2.7 < \lvert\eta\rvert < 3.5$)			
$E_{\mathrm{T}}^{\mathrm{miss}} > 35$ GeV			
$m_T(l, E_{\mathrm{T}}^{\mathrm{miss}}) > 60$ GeV			
$p_T(\ell) > 50\left(1 - \frac{\pi - \lvert\Delta\phi(j_1,\ell)\rvert}{\pi - 1}\right)$ GeV			
=1 b-jet ($\lvert\eta\rvert < 2.5$; 60%WP)		=2 b-jet ($\lvert\eta\rvert < 2.5$; 60%WP)	=1 b-jet ($\lvert\eta\rvert < 2.5$; 60%WP)
	$m_{lb} < 153$ GeV $m_{\ell E_{\mathrm{T}}^{\mathrm{miss}} b} \in [120.6, 234.6$ GeV $m_{j\ell E_{\mathrm{T}}^{\mathrm{miss}} b} > 320$ GeV $H_T > 190$ GeV trapezoidal requirement (eq. 5.3)		$m_{lb} > 153$ GeV $m_{\ell E_{\mathrm{T}}^{\mathrm{miss}} b} \notin [120.6, 234.6]$ GeV $m_{j\ell E_{\mathrm{T}}^{\mathrm{miss}} b} < 320$ GeV $H_T < 190$ GeV veto trapez. requirement

Table 5.2: Summary of the selection criteria for defining the preselection, signal and control regions. Taken from [87].

5.4 Background estimation

For the single top quark in the t-channel the possible backgrounds are: $t\bar{t}$, single top s-channel and Wt production modes, multijets, W+jets, Z+jets, di-boson (WW, ZZ and WZ) and associated vector boson or Higgs production ($t\bar{t}Z$, $t\bar{t}W$, $t\bar{t}H$, tZq, tHq and tWZ). The estimation of these backgrounds are discussed in this section.

5.4.1 Monte Carlo

Apart from the multijet background, discussed later on, all backgrounds are modelled using MC sampling methods. In general MC methods reproduce the shapes of distributions relatively well. However, the rates are theoretically and experimentally more difficult to match. For this reason, the shape of these predictions are verified in the dedicated CRs, see the definitions in section 5.3.3, and a small scale factor could be assigned to adjust the normalisation (rate). At a later stage also systematic variations are applied to account for possible differences in the shape. The distributions of the polarisation angles in the $t\bar{t}$ and W+jets control regions can be found in figures 5.3 and 5.4, respectively. Overall a good modelling of the shape can be observed.

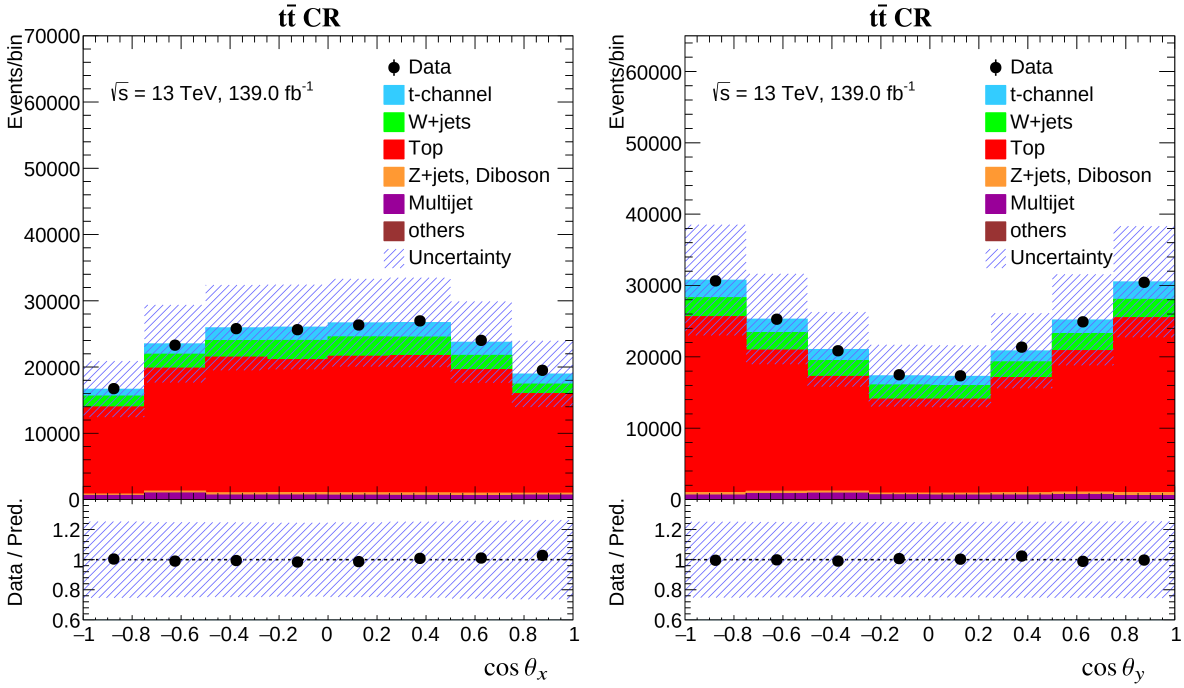

Figure 5.3: Distributions of $\cos\theta_x$ *(left) and* $\cos\theta_y$ *(right) in the* $t\bar{t}$ *control region. The prediction is compared to data, shown as the black points with statistical and systematic uncertainties. The lower inset shows the ratio of data over the prediction. Taken from [87].*

The normalisation of the MC predictions are addressed by introducing scale factors shown in table 5.3. They are obtained from a fit to both control regions together with the event yield from the signal region, where all background processes containing top quarks have been merged to reduce statistical fluctuations. All the backgrounds not in the table (Z+jets, di-boson, multijet and vector or Higgs boson associated production) are fixed in the extraction of the scale factors.

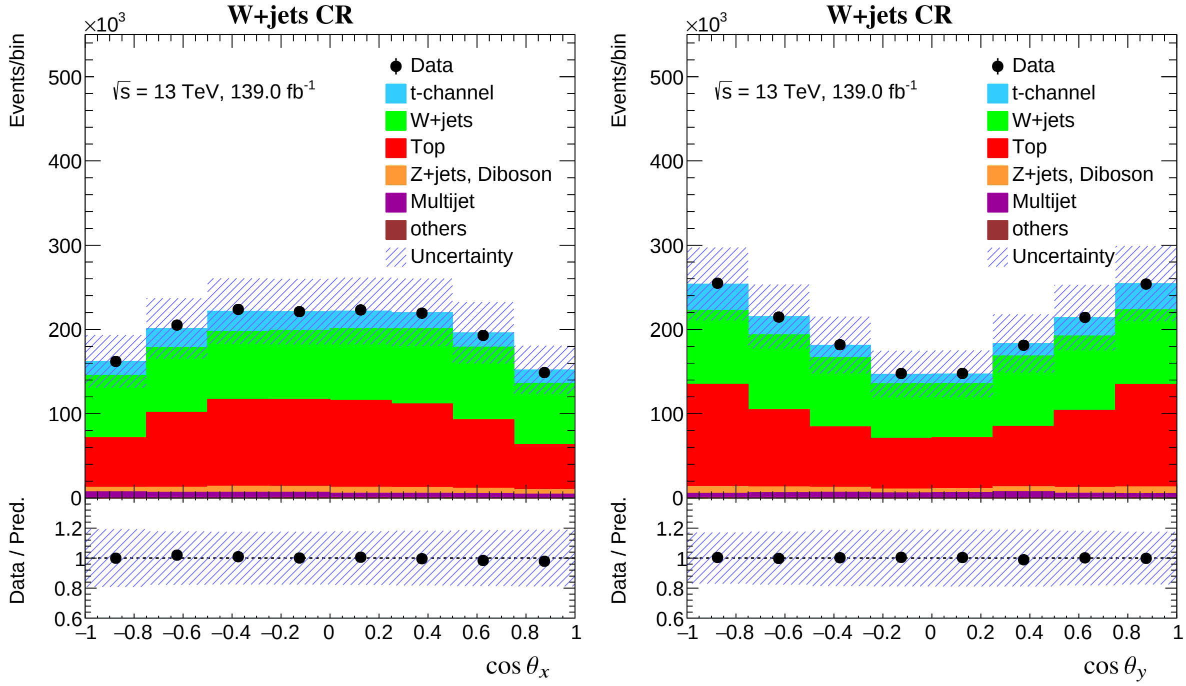

Figure 5.4: Distributions of $\cos\theta_x$ *(left) and* $\cos\theta_y$ *(right) in the* W*+jets control region. The prediction is compared to data, shown as the black points with statistical and systematic uncertainties. The lower inset shows the ratio of data over the prediction. Taken from [87].*

Process	Scale factor
t-channel	1.050
W+jets	1.114
$t\bar{t}$,Wt,s-channel	0.983

Table 5.3: Scale factors extracted for the normalisation of the MC predictions. They are obtained from a fit to both $t\bar{t}$ *and* W*+jets control regions together with the event yield from the signal region. All background processes containing top quarks have been merged to reduce statistical fluctuations. Taken from [87].*

5.4.2 Multijet

A different approach is needed for estimating multijet events containing a "fake" charged lepton[6]. Fake leptons originate from four sources: the mis identification of a narrow jet, a leptonic decay of a hadron, leptons from cosmics that overlap with a QCD event and the conversion of a photon to an electron. Even though the probability for reconstructing a fake lepton is sizeable, the overwhelming production rate of multijets in hadron collisions makes the contribution of this background significant. The estimation of the multijet background is done differently when considering electrons or muons.

The shape of the fake electron distribution is obtained from simulated di-jet events where one jet should fake an electron in order to be selected. This is called the jet-electron method [96]. Its normalisation is obtained from fitting $E_{\mathrm{T}}^{\mathrm{miss}}$ simultaneously in the $t\bar{t}$ CR and a dedicated electron multijet enriched region. This fake electron region is defined as the preselection (PR) where the isolation requirement (equation 5.2) is relaxed together with the cut on $E_{\mathrm{T}}^{\mathrm{miss}}$. A distinction is made between the central ($|\eta| < 1.37$) and forward ($1.52 < |\eta| < 2.5$) regions, excluding the region between the barrel and the end-cap of the EM calorimeter.

For the fake muons the shape is estimated via the fully data-driven anti-muon method [96]. Here requirements to identify the muon are inverted to obtain data events that are populated with fake muons. The normalisation of the fake muons is extracted by fitting the $m_T(l, E_{\mathrm{T}}^{\mathrm{miss}})$ parameter simultaneously in the $t\bar{t}$ control region and a dedicated muon multijet enriched region. This fake muon region is defined as the preselection (PR) where the isolation requirement (equation 5.2) is relaxed together with the cut on $m_T(l, E_{\mathrm{T}}^{\mathrm{miss}})$.

Figure 5.5 shows the distributions of $E_{\mathrm{T}}^{\mathrm{miss}}$ in the fake electron enriched regions and $m_T(l, E_{\mathrm{T}}^{\mathrm{miss}})$ in the fake muon enriched region. A reasonable agreement is observed.

5.5 Event yields

Figure 5.6 provides a visualisation of how the t-channel signal and background processes populate the different selection regions. The numbers, with statistical uncertainties, are given in table 5.4 together with the amount of data events. Additionally the ratios signal over background and data over prediction are presented.

Process	Preselection region	Signal region	$t\bar{t}$ control region	W+jets control region
t-channel	229667 ± 259	74180 ± 147	14156 ± 65	155487 ± 213
$t\bar{t}$	623005 ± 314	37928 ± 78	137402 ± 146	585077 ± 304
tW	92721 ± 165	4196 ± 35	4436 ± 36	88525 ± 161
s-channel	8642 ± 17	361 ± 3	3448 ± 11	8280 ± 17
W+heavy-jets	600815 ± 1891	26445 ± 490	17451 ± 160	574370 ± 1826
W+light-jets	36296 ± 1062	1342 ± 228	428 ± 82	34954 ± 1037
Z+jets and diboson	52891 ± 334	2121 ± 68	2617 ± 38	50785 ± 327
Others	528 ± 3	31 ± 1	91 ± 1	497 ± 3
Multijet	88708 ± 1128	6643 ± 234	8266 ± 396	82064 ± 1104
Total prediction	1733273 ± 2505	153249 ± 616	188296 ± 466	1580038 ± 2428
Data	1750918 ± 1323	154361 ± 392	188326 ± 433	1596557 ± 1263
Signal/Background	0.15	0.94	0.08	0.11
Data/Prediction	1.01	1.01	1.00	1.01

Table 5.4: Event yields in the preselection, signal region, the $t\bar{t}$ control and W+jets control regions. The predicted yield, with statistical uncertainties, per process is given together with the number of data events. Additionally the ratios signal over background and data over prediction are presented. Taken from [87].

---

[6] To be clear, the name "fake" lepton can also refer to an actual lepton. However, as long as they do not originate from the hard process they are called fake in this analysis.

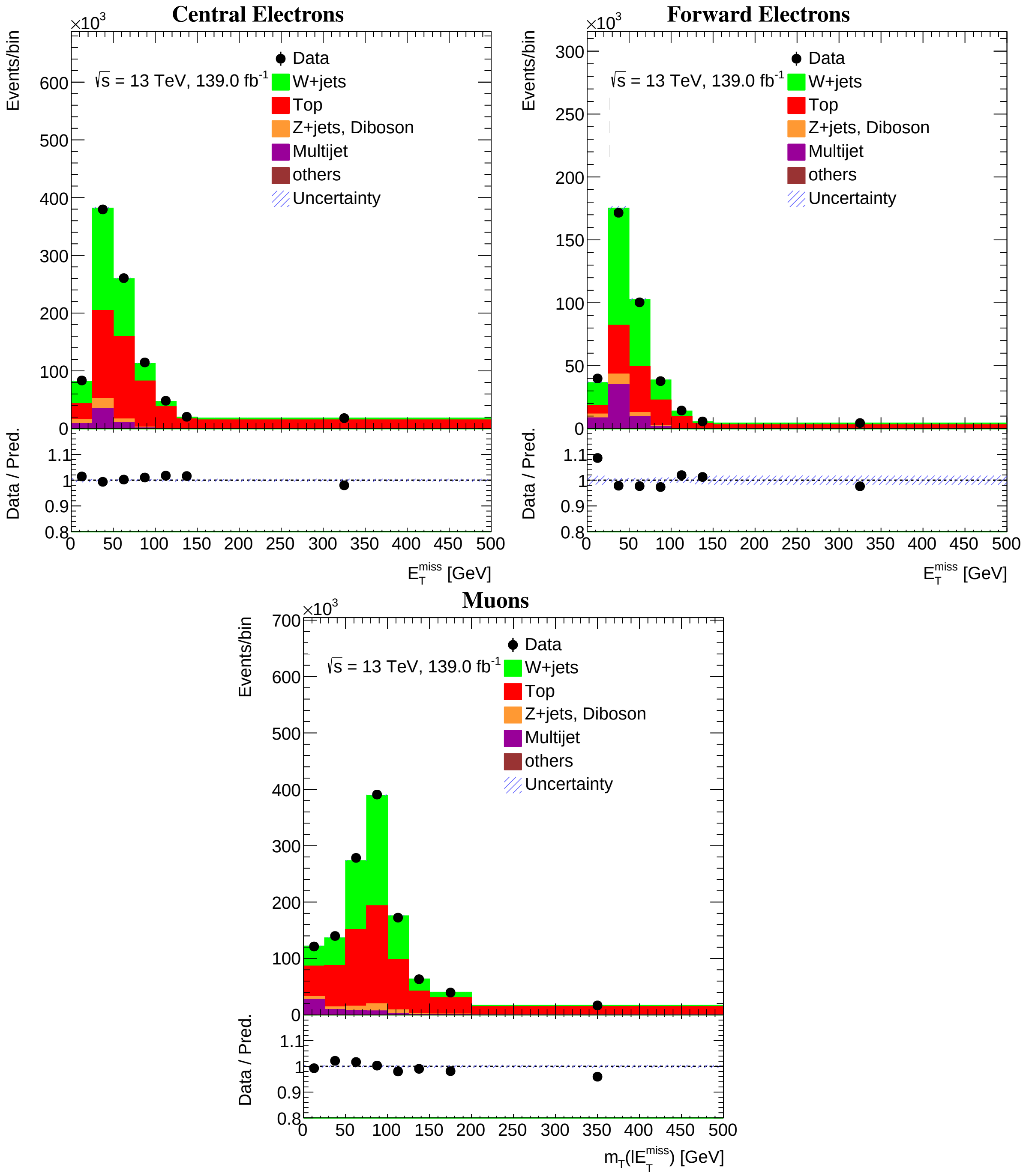

Figure 5.5: Distributions of the $E_{\mathrm{T}}^{\mathrm{miss}}$ *in the fake lepton enriched region for the central electron channel (top left), the forward electron channel (top right), and the* $m_T(l, E_{\mathrm{T}}^{\mathrm{miss}})$ *distribution in the muon channel (bottom). The error bars only contain statistical contributions and are smaller than the dots. Taken from [87].*

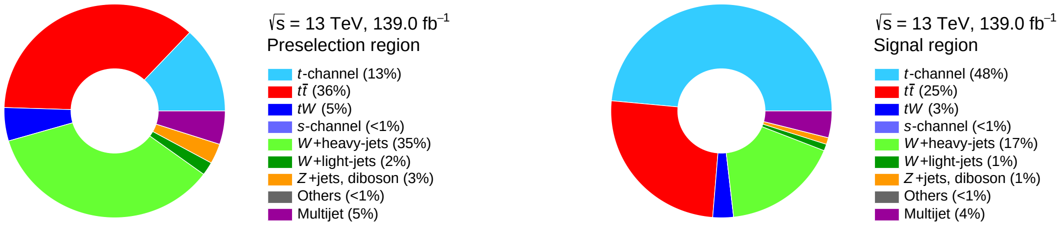

(a) Preselection region *(b) Selection region*

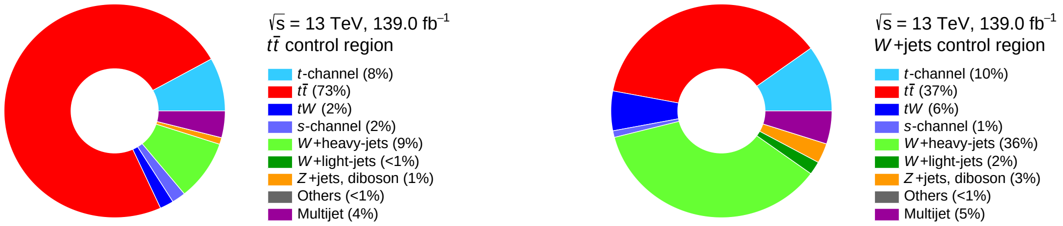

(c) $t\bar{t}$ control region *(d) W+jets control region*

Figure 5.6: The relative contributions of the t-channel signal and the background processes in the (a) preselection region, (b) signal region, and in the (c) $t\bar{t}$ and (d) W+jets control regions. Taken from [87].

5.6 Sources of systematic uncertainties

Systematic uncertainties can be divided into two categories: experimental and theoretical. The experimental sources consist of: luminosity, pile-up reweighting[7], missing energy reconstruction, charged lepton reconstruction, the momentum scale and resolution of charged leptons and measuring jets: reconstructing jet vertices, determining the jet energy scale (JES), the resolution on the jet energy (JER) and b-tagging. The theoretical uncertainties consist of: modelling uncertainty related to the choice for the hard process generator and parton shower, the dependence on the factorisation and renormalisation scales (μ_F and μ_R), the effect from different choices for the PDF set and the normalisation of the backgrounds (scale factors).

The impact of each systematic uncertainty is evaluated by comparing different variations with respect to the nominal prediction for the polarisation angles. All uncertainties are estimated separately and are added in quadrature to obtain the total uncertainty. The most dominant sources of uncertainties are the modelling of the signal sample (generator ~10% and parton shower ~8%) and the jet energy resolution (JER ~7%).

5.7 Results

The polarisation angles in the signal region are shown in figure 5.7, where the uncertainty band corresponds to the statistical and systematic uncertainties added in quadrature. A good agreement between the data and the prediction is observed.

---

[7] A procedure to improve the agreement between simulation and data by weighting MC events according to the distribution of the average number of interactions per bunch crossing observed in the data.

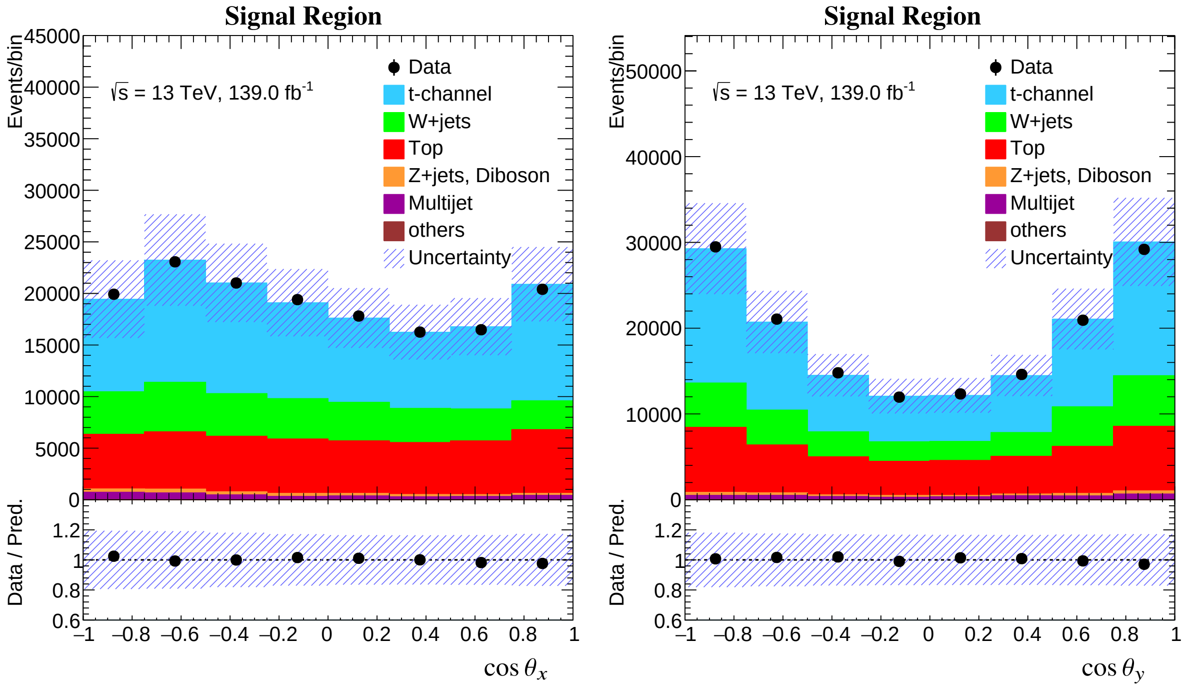

Figure 5.7: Distributions of $\cos\theta_x$ *(left) and* $\cos\theta_y$ *(right) in the signal region. The prediction is compared to data, shown as the black points with statistical and systematic uncertainties. The lower inset shows the ratio of data over the prediction. Taken from [87].*

Chapter 6

Unfolding the top quark polarisation angles to particle level

This chapter presents the unfolding analysis of the polarisation angles from the single top quark in the t-channel measured with the ATLAS detector as discussed in chapter 5. The results have been presented at the LHCP-2021 conference and a conference note is under review. A paper by the ATLAS collaboration is in preparation. A summary will be presented here focusing on the $\cos\theta_x$ and $\cos\theta_y$ distributions which are later used to analyse the effects of O_{tW}.

6.1 The principle

Monte Carlo generation of proton-proton collisions can not be directly compared to data measured with a detector. The effects from particles propagating through material has to be taken into account, which is done by simulating the detector response. This process could be expressed by a migration matrix that encodes the propagation from particle level (MC simulation) to reco level (after detector simulation and reconstruction). Another possibility is to remove these detector effects from the measured data, a technique that is commonly referred to as unfolding.

In this work the data measured with the ATLAS detector (reco level) will be unfolded to particle level (sometimes indicated as truth). Some analyses, usually LO QCD, unfold back to parton level, where individual quarks are identified[1]. That is not the case here, the measured data is unfolded to particle level where all the partons, after hadronisation, are isolated detectable particles or have been clustered into jets. In part III of this work only the shapes of the polarisation angles are exploited, not the rate (cross section). Therefore, the distributions of $\cos\theta_x$ and $\cos\theta_y$ are separately normalised to unity after unfolding.

The unfolding procedure is given in expression 6.1, where reco level bins r are transported to their particle level bin p counterparts. First all backgrounds (B) are subtracted from the data (N^{data}). Then the remaining signal-like data is corrected for events that pass the selection at reco level but fail those at particle level ($C_r^{\text{reco!particle}}$). The transformation to particle level is done with the migration matrix (M), using the iterative Bayesian method [97]. Finally the result is corrected for events that pass the selection at particle level but fail the selection at reco level ($C_p^{\text{particle!reco}}$).

$$N_p^{\text{particle}} = C_p^{\text{particle!reco}} \sum_r M_{pr}^{-1} C_r^{\text{reco!particle}} (N_r^{\text{data}} - B_r) \tag{6.1}$$

---

[1] The definition of the parton level gets diluted due to higher order QCD effects and corrections used in the calculation.

The correction factors arise from a different response of the selection criteria to particle level or reco level distributions. They are defined in equation 6.2, where as an example: $S_p^{\text{particle!reco}}$ indicates the number of events in bin p that pass the selection at particle level but fail those after detector simulation and reconstruction (reco). A visualisation is shown in figure 6.1, where the two squares correspond to the phase space of reco and particle level events. The grey overlapping region is from which the migration matrix (M) is obtained and the remaining white areas miss either events at reco or particle level for which a correction factor is applied.

$$C_r^{\text{reco!particle}} = \frac{S_r^{\text{reco}} - S_r^{\text{reco!particle}}}{S_r^{\text{reco}}} \qquad C_p^{\text{particle!reco}} = \frac{1}{\epsilon_p} = \frac{S_p^{\text{particle}}}{S_p^{\text{particle}} - S_p^{\text{particle!reco}}}. \tag{6.2}$$

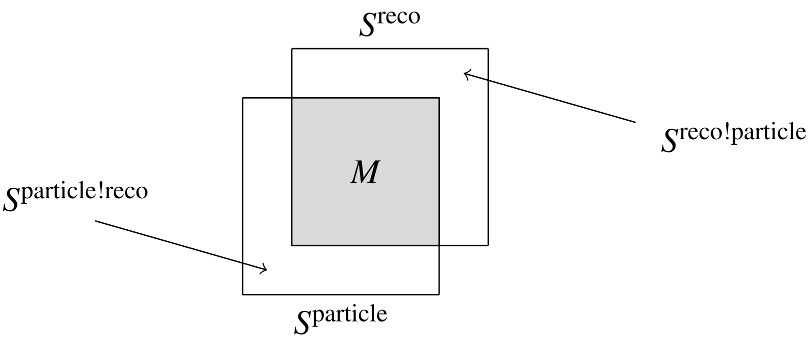

Figure 6.1: Visualisation of event classes based on passing (or failing) selection criteria at particle and/or reco level.

6.2 Unfolding in single top

The migration between particle level (y-axis) and reconstructed events (x-axis) for $\cos\theta_x$ and $\cos\theta_y$ of the single top quark are shown in figure 6.2. They are obtained from MC generated t-channel events that pass through a simulated ATLAS detector. It is verified that with the current choice of binning, the migration is modest as the diagonal elements contain at least 70% of the events.

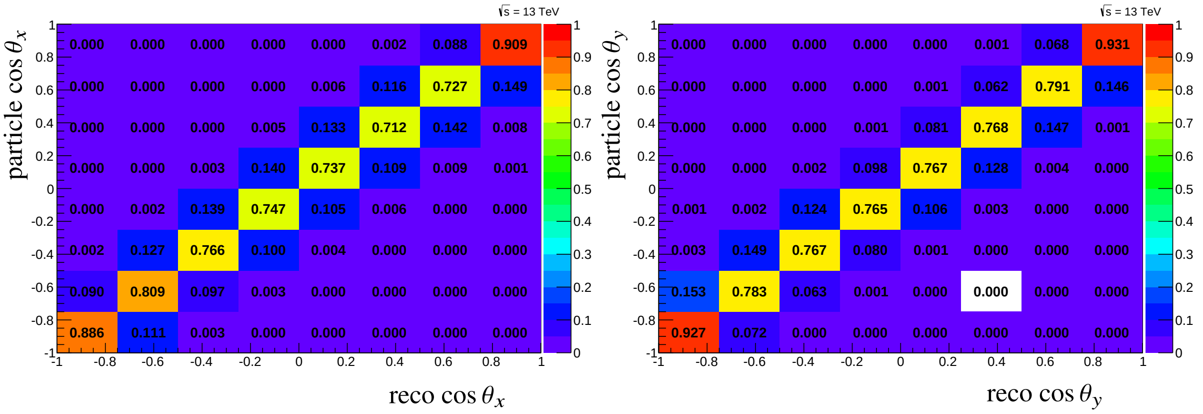

0.000	0.000	0.000	0.000	0.000	0.002	0.088	0.909
0.000	0.000	0.000	0.000	0.006	0.116	0.727	0.149
0.000	0.000	0.000	0.005	0.133	0.712	0.142	0.008
0.000	0.000	0.003	0.140	0.737	0.109	0.009	0.001
0.000	0.002	0.139	0.747	0.105	0.006	0.000	0.000
0.002	0.127	0.766	0.100	0.004	0.000	0.000	0.000
0.090	0.809	0.097	0.003	0.000	0.000	0.000	0.000
0.886	0.111	0.003	0.000	0.000	0.000	0.000	0.000

0.000	0.000	0.000	0.000	0.000	0.001	0.068	0.931
0.000	0.000	0.000	0.000	0.001	0.062	0.791	0.146
0.000	0.000	0.000	0.001	0.081	0.768	0.147	0.001
0.000	0.000	0.002	0.098	0.767	0.128	0.004	0.000
0.001	0.002	0.124	0.765	0.106	0.003	0.000	0.000
0.003	0.149	0.767	0.080	0.001	0.000	0.000	0.000
0.153	0.783	0.063	0.001	0.000	0.000	0.000	0.000
0.927	0.072	0.000	0.000	0.000	0.000	0.000	0.000

Figure 6.2: Migration matrices for $\cos\theta_x$ (left) and $\cos\theta_y$ (right). The angular variable at particle level is shown on the y-axis while the reconstructed angular variable is shown on the x-axis. Taken from [87].

It is also useful to investigate the distribution of the unfolding corrections defined in equation 6.2 from various MC generators. These are shown in figures 6.3 and 6.4, where the nominal sample (black) is compared to aMC@NLO (blue) and the LO generator Protos (red). Additionally, the green lines show the nominal MC generator (Powheg) where a less detailed detector simulation[2] has been employed (AFII). Across the board a rather flat behaviour is observed independent of the choice of MC generator. Powheg has in general somewhat higher values for $S^{\text{reco!particle}}$, but evenly lower values of $S^{\text{particle!reco}}$. This effect is rather uniform and since this analysis exploits the normalised angular distributions, only the shape is important. No large differences in the shape between the various MC generators is observed, they appear to be within the statistical uncertainties, which is best seen in the ratio defined with respect to the nominal (black) shown in the lower insets. In the final unfolded $\cos\theta_x$ and $\cos\theta_y$ distributions, the difference between modelling the signal process with either Powheg or aMC@NLO is included as a systematic uncertainty.

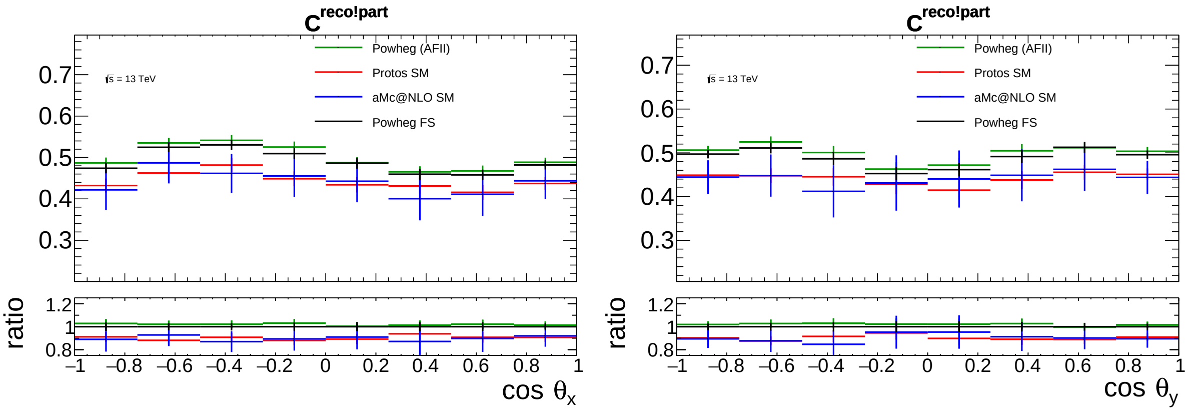

Figure 6.3: Reconstruction level efficiencies for $\cos\theta_x$ (left) and $\cos\theta_y$ (right) from various MC generators, where the ratio is with respect to the nominal Powheg FS (black). Taken from [87].

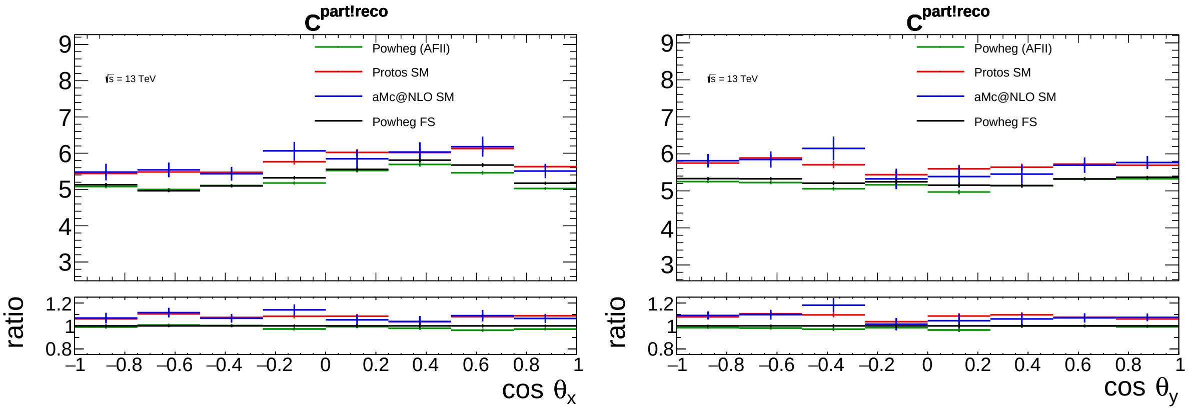

Figure 6.4: Inverse of particle level efficiencies for $\cos\theta_x$ (left) and $\cos\theta_y$ (right) from various MC generators, where the ratio is with respect to the nominal Powheg FS (black). Taken from [87].

---

[2] The difference with respect to the full detector simulation (FS) is that AFII employs a parametrisation for the calorimeters [98].

6.2.1 Validation

The black lines in figure 6.5 show the results for unfolding the $\cos\theta_x$ and $\cos\theta_y$ distributions of the SM aMC@NLO sample using the migration matrix and corrections obtained from the nominal Powheg sample. The unfolded (solid lines) are in good agreement with the expectation (dashed lines), where the black uncertainty band includes the limited MC statistics together with the systematic modelling uncertainty related to the choice of the MC generator.

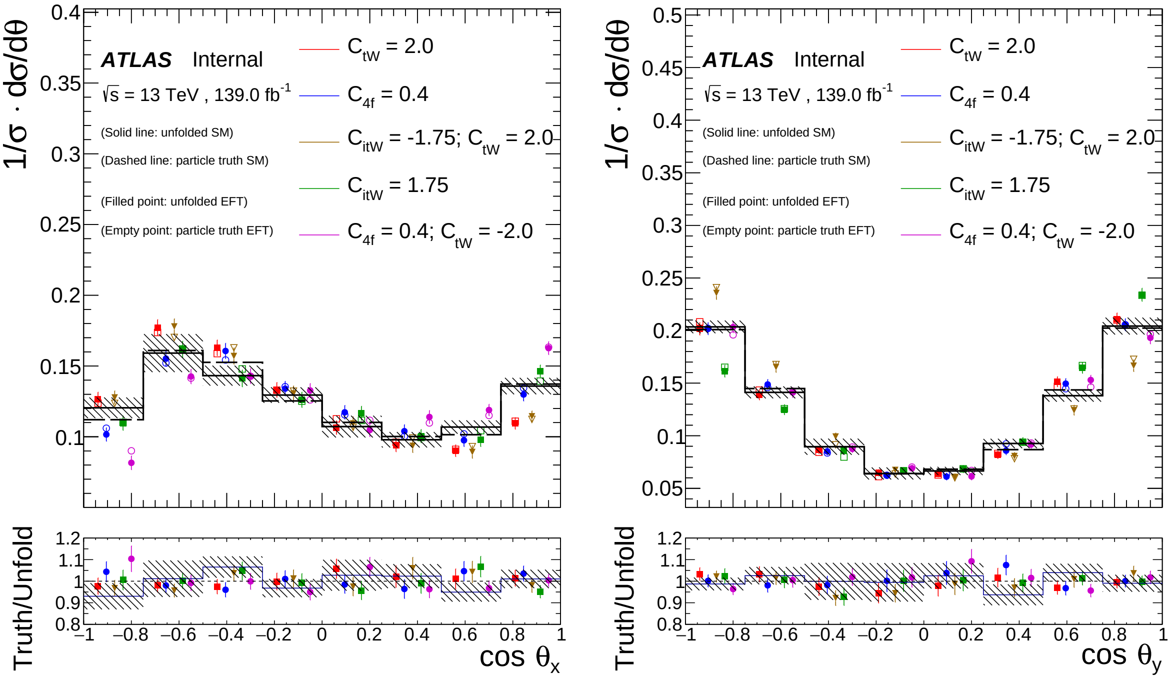

Figure 6.5: Unfolding $\cos\theta_x$ *(left) and* $\cos\theta_y$ *(right) of aMC@NLO SM (black) and new physics samples (coloured) using the migration matrix and corrections obtained from Powheg. The black solid lines and the open coloured markers correspond to the particle level distributions, while the black dashed lines and the filled coloured markers represent the unfolded ones. The lower insets shows the ratio between the particle level and unfolded distributions and the uncertainty is computed from the statistical error on the unfolded histograms, where the black uncertainty band additionally contains the systematic modelling uncertainty related to the choice of the MC generator.*

The ultimate target of this analysis is to extract the Wilson coefficients of O_{tW} from the measured data. The unfolding procedure should not depend on effects caused by O_{tW} or any other effective operator. Therefore the linearity test is conducted, where Powheg SM is used to unfold the aMC@NLO samples that contain EFT operators. The coloured markers in figure 6.5 show the linearity, where the filled points (unfolded) should be compared with the open points (particle level) of the same colour. The lower insets presents the ratio between the open and the filled points, which clearly show that, even for these rather large values of the coefficients, all fluctuations are consistent within the statistical uncertainties of the MC simulation. This indicates that the unfolding is not sensitive to EFT operators within the precision of the current analysis.

6.3 Uncertainties

Due to the unfolding procedure, correlations arise between the bins of the unfolded distributions of $\cos\theta_x$ and $\cos\theta_y$. For this reason, all uncertainties and correlations are given in the covariance matrix (Σ) found in table 6.1. Its size is 16 by 16 and includes the correlations between the two polarisation angles from the same dataset. This section explains how these uncertainties are obtained at particle level.

6.3.1 Constructing the covariance matrix

The covariance matrix that contains all bin-to-bin uncertainties and correlations is obtained by adding multiple separately created matrices. The statistical matrix is obtained by multiplying the statistical bin uncertainty (from data) with the correlations extracted from a bootstrap method [99]. The matrix containing most of the systematic uncertainty sources, excluding the generator modelling and PDF, is estimated using pseudo-experiments (toys) produced at reco level. A toy distribution is created by scaling each data bin (N_r^{obs}) with the relative variation from systematic uncertainties:

$$\mathrm{toy}_r^k = N_r^{\mathrm{obs}} \cdot \left(1 + \sum_s^{\mathrm{systematics}} |\lambda_s| \cdot \Delta_{rs} \right). \tag{6.3}$$

For each systematic uncertainty an independent random number λ is drawn from a standard normal distribution. According to the sign of λ, the corresponding up (positive) or down (negative) variation is taken coherently for all bins. These systematic shifts are generally asymmetric, where in the case of a one-sided systematic its variation is symmetrised. The relative systematic variation is defined as the relative difference between the signal plus background of the varied (sys) and nominal distributions:

$$\Delta_{rs} = \frac{B_{rs}^{\mathrm{sys}} + S_{rs}^{\mathrm{sys}} - B_r^{\mathrm{nominal}} - S_r^{\mathrm{nominal}}}{B_r^{\mathrm{nominal}} + S_r^{\mathrm{nominal}}}. \tag{6.4}$$

For each such toy, the bins of the MC signal and background samples, apart from the multijet, are fluctuated within the corresponding MC error in all selection regions (SR and CRs) and unique scale factors for the background rates are obtained according to section 5.4. The scaled backgrounds are subtracted from the toy distribution, obtained with equation 6.3, and the signal-like toy is unfolded using the nominal migration matrix and corrections. The covariance matrix is build from 50k pseudo-experiments according to:

$$\Sigma(i,j) = \langle (d\sigma_i - \langle d\sigma_i \rangle_n) \cdot (d\sigma_j - \langle d\sigma_j \rangle_n) \rangle_n, \tag{6.5}$$

where $d\sigma_i$ and $d\sigma_j$ are the values of the angular bins (differential cross sections) and $\langle \ldots \rangle_n$ indicates the averaging over n toys.

The uncertainties related to the generator modelling and PDF are not included in the toy production. Their contributions to the covariance matrix are obtained by fully correlating the difference between the unfolded variation V and the unfolded nominal N across all 16 bins:

$$\begin{aligned} \Delta &= V - N, \\ \Sigma_{\mathrm{sys}} &= \Delta \cdot \Delta^T. \end{aligned} \tag{6.6}$$

Only for the modelling of the t-channel signal the bins of the $\cos\theta_x$ and $\cos\theta_y$ distributions are decorrelated. The uncertainty related to the PDF is estimated by taking the average of multiple different PDF sets, following the recommendation [100]:

$$\Sigma_{\mathrm{PDF}} = \frac{1}{N} \sum_i^N \Sigma_i. \tag{6.7}$$

6.3.2 Normalisation and the full covariance matrix

Individual uncertainty sources are not correlated and the separately created covariance matrices are added together to obtain the full combined covariance matrix. However, normalisation causes an overall correlation between the bins, across all uncertainty sources. It is therefore desirable to apply the normalisation at the end, after all uncertainty sources are combined. This is done by exploiting another set of toys where each toy, produced from the combined covariance matrix, is normalised separately. The full covariance matrix, containing all bin-wise uncertainties and correlations on the unfolded and normalised $\cos\theta_x$ and $\cos\theta_y$ measured distributions, is obtained from these normalised toys according to equation 6.5. The result is given in table 6.1.

$\cos\theta_x$	473.7	214.5	-21.28	29.96	-133.0	-129.5	-186.3	-248.1	5.171	-94.4	43.85	79.44	47.16	50.47	25.72	-157.4
	214.5	244.6	15.31	35.07	-113.6	-107.9	-108.2	-179.7	11.12	-66.54	28.23	37.14	8.168	22.42	59.8	-100.4
	-21.28	15.31	82.17	-28.36	7.559	-5.089	-17.76	-32.55	-1.647	15.98	2.272	-10.38	-11.75	-17.39	4.22	18.69
	29.96	35.07	-28.36	90.48	-72.65	-47.74	-1.227	-5.534	-1.891	-30.15	2.677	1.927	8.263	8.875	51.61	-41.31
	-133.0	-113.6	7.559	-72.65	184.2	83.44	-8.382	52.49	31.69	38.1	-36.39	-14.48	-18.71	0.646	-112.0	111.2
	-129.5	-107.9	-5.089	-47.74	83.44	129.9	19.4	57.5	38.47	24.0	-37.51	-13.29	-21.54	0.756	-75.11	84.21
	-186.3	-108.2	-17.76	-1.227	-8.382	19.4	172.1	130.3	-44.63	58.66	5.908	-36.79	-16.84	-44.21	45.84	32.06
	-248.1	-179.7	-32.55	-5.534	52.49	57.5	130.3	225.5	-38.28	54.35	-9.034	-43.57	5.247	-21.57	-.047	52.91
$\cos\theta_y$	5.171	11.12	-1.647	-1.891	31.69	38.47	-44.63	-38.28	96.06	-47.14	-29.5	9.868	-16.42	20.73	-48.38	14.77
	-94.4	-66.54	15.98	-30.15	38.1	24.0	58.66	54.35	-47.14	97.0	-3.466	-22.07	-14.13	-32.24	-19.61	41.66
	43.85	28.23	2.272	2.677	-36.39	-37.51	5.908	-9.034	-29.5	-3.466	47.09	-1.259	11.59	-13.1	33.17	-44.52
	79.44	37.14	-10.38	1.927	-14.48	-13.29	-36.79	-43.57	9.868	-22.07	-1.259	33.38	2.775	14.91	-12.27	-25.34
	47.16	8.168	-11.75	8.263	-18.71	-21.54	-16.84	5.247	-16.42	-14.13	11.59	2.775	39.6	7.058	3.763	-34.23
	50.47	22.42	-17.39	8.875	0.646	0.756	-44.21	-21.57	20.73	-32.24	-13.1	14.91	7.058	47.75	-25.49	-19.61
	25.72	59.8	4.22	51.61	-112.0	-75.11	45.84	-0.047	-48.38	-19.61	33.17	-12.27	3.763	-25.49	151.1	-82.31
	-157.4	-100.4	18.69	-41.31	111.2	84.21	32.06	52.91	14.77	41.66	-44.52	-25.34	-34.23	-19.61	-82.31	149.6
	$\cos\theta_x$								$\cos\theta_y$							

Table 6.1: Full normalised covariance matrix ($\cdot 10^{-5}$)

6.4 Results

Figure 6.6 shows the unfolded and normalised data distributions compared with various particle level predictions from different MC generators. The uncertainty band, which contains the statistical and systematic contributions, covers the differences among the MC predictions. In some bins the uncertainty is smaller than seen in the result before unfolding, figure 5.7. The reason for this is that the normalisation reduces the effect from some uncertainty sources, i.e. the modelling uncertainty for the generator choice becomes less than 5% as opposed to 10% before normalisation. Finally, figure 6.7 compares the unfolded result with new physics samples. It is observed that, with the current precision, there is sensitivity to the real and imaginary part of the coefficient of O_{tW}.

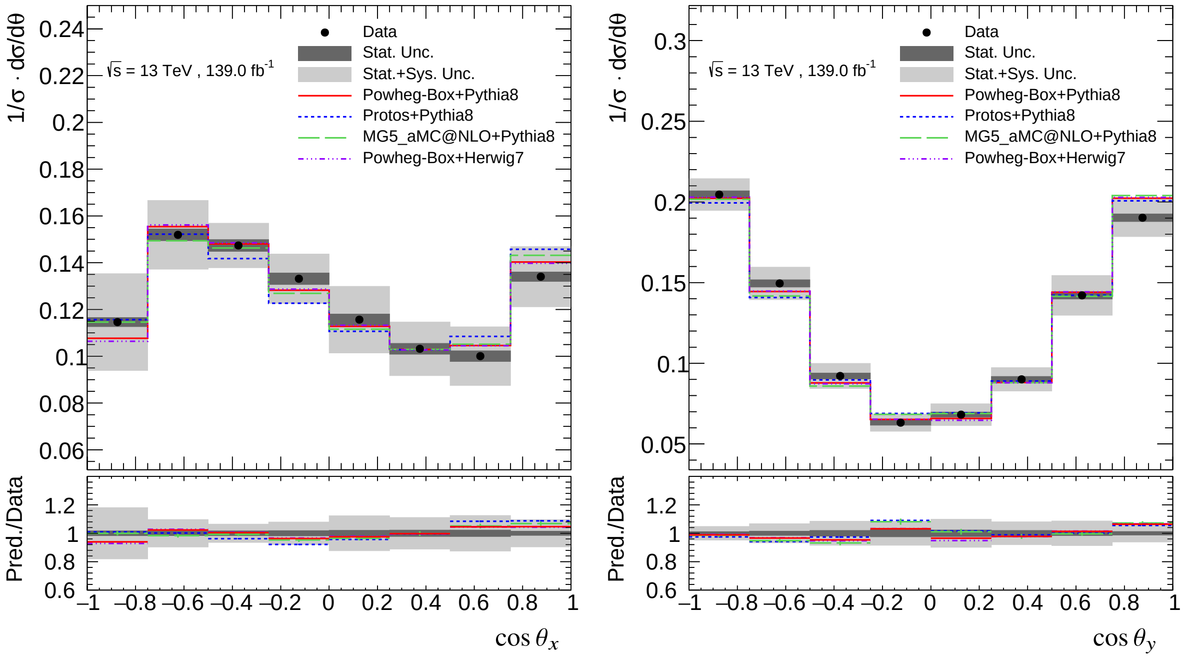

Figure 6.6: The unfolded normalised angular distributions for $\cos\theta_x$ (left) and $\cos\theta_y$ (right) together with particle level predictions from various MC generators. The uncertainty bands includes the statistical and systematic uncertainties. Taken from [87].

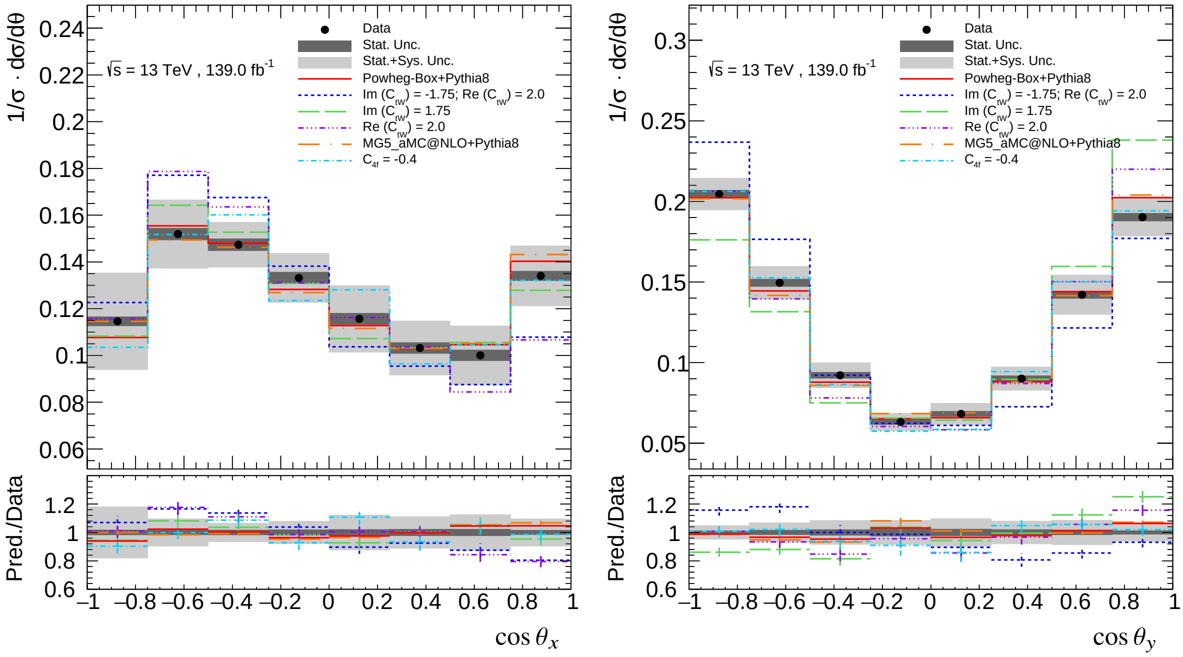

Figure 6.7: The unfolded normalised angular distributions for $\cos\theta_x$ *(left) and* $\cos\theta_y$ *(right) together with new physics samples. The uncertainty bands includes the statistical and systematic uncertainties. Taken from [87].*

Part III

EFT interpretation


PJOT

Chapter 7

Parametric description of the EFT signal

To confront predictions with data, a model with Wilson coefficients as parameters is needed. The parametrisation used in this analysis is based on templates as no analytic description is available (beyond LO). A technique called morphing [101, 102] will be exploited, whose feature is that it requires only a minimal number of templates. These templates consist of the (differential) cross sections obtained from MC samples that have been generated as described in section 3.1.

7.1 Morphing: the principle

The matrix element that needs to be parametrised has an important feature, namely that it can be expressed as an expansion of Wilson coefficients with unique terms that depend on the EFT operators. These terms are the basis of the morphing technique.

As an example, the simplest case will be presented where only the real part of O_{tW} contributes to the production vertex. The cross section can then be described by three individual terms: the SM part, the pure O_{tW} part and the interference between them. This is shown in equation 7.1, where in fact the underlined O terms on the right-hand side are unknown numbers.

$$\sigma(C_{\mathrm{SM}}, C_{tW}) = \left| C_{\mathrm{SM}} \cdot O_{\mathrm{SM}} + \frac{C_{tW}}{\Lambda^2} \cdot O_{tW} \right|^2 = C_{\mathrm{SM}}^2 \cdot \underline{O_{\mathrm{SM}}^2} + \frac{C_{\mathrm{SM}} C_{tW}}{\Lambda^2} \cdot 2\, \underline{O_{\mathrm{SM}} O_{tW}} + \frac{C_{tW}^2}{\Lambda^4} \cdot \underline{O_{tW}^2} \qquad (7.1)$$

In this particular case there are three unknowns leading to the requirement of three equations to solve for them. This is where the templates come in. Each MC sample can be generated with a chosen set of Wilson coefficients and therefore produces a template cross section at different values for the coefficients. Each template is thus its own version of equation 7.1. One choice for the three templates, needed to solve for the three unknowns in this example, could be the following: the SM ($C_{\mathrm{SM}} = 1, C_{tW} = 0$), only tW ($C_{\mathrm{SM}} = 0, C_{tW} = 1$) and a mix where both the SM and tW contribute ($C_{\mathrm{SM}} = 1, C_{tW} = 1$). This is schematically made visible in figure 7.1, where the three generated templates (on the left) are used to extract the three unknown terms (on the right).

Once the unknown terms are solved, predictions for cross sections at different values of C_{tW} are straightforwardly obtained. A more convenient way of writing equation 7.1 is as a weighted sum over all the morphing templates. This is given in equation 7.2 where w_t and σ_t correspond to the weight and cross section of template t, respectively.

$$\sigma(C_{\mathrm{SM}}, C_{tW}) = \sum_{t}^{\text{templates}} w_t(C_{\mathrm{SM}}, C_{tW}) \cdot \sigma_t \qquad (7.2)$$

Solving for the weights is a linear problem and they are obtained by inverting the so called coupling matrix[1]. For the example at hand, table 7.1 shows the three templates with their values for the coefficients (on the left) and the corresponding coupling matrix (on the right).

---

[1] In the case of $C_{\mathrm{SM}} = 1$ this is known as the Vandermonde matrix.

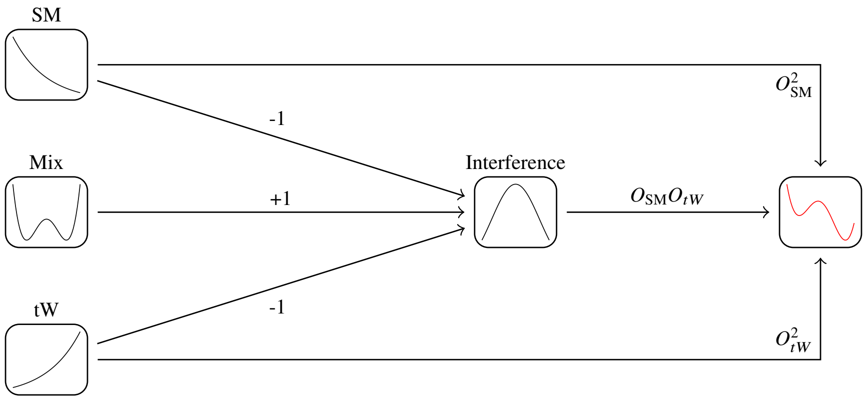

Figure 7.1: A simple example of the morphing principle. Just three contributing terms are present and therefore only three templates are required. The three templates (on the left) are used to extract the three unknown terms (on the right). In this example the following three templates are depicted: the SM ($C_{SM} = 1, C_{tW} = 0$), only tW ($C_{SM} = 0, C_{tW} = 1$) and a mix where both the SM and tW contribute ($C_{SM} = 1, C_{tW} = 1$). Taken from [102].

Template name	C_{SM}	C_{tW}
SM	1	0
Mix	1	1
tW	0	1

→

C^2_{SM}	$C_{\mathrm{SM}}\cdot C_{tW}$	C^2_{tW}
1	0	0
1	1	1
0	0	1

Table 7.1: The values for the coefficients of the templates for a simple morphing example (left) and the corresponding coupling matrix (right).

Inverting the coupling matrix provides the weights that are needed to construct the prediction for σ as a function of C_{SM} and C_{tW}:

$$\begin{aligned}\sigma(C_{\mathrm{SM}}, C_{tW}) = \sum_{t}^{\text{templates}} w_t(C_{\mathrm{SM}}, C_{tW}) \cdot \sigma_t = \underbrace{\left(1 \cdot C^2_{\mathrm{SM}} - 1 \cdot C_{\mathrm{SM}}C_{tW} + 0 \cdot C^2_{tW}\right)}_{w_{\mathrm{SM}}} \cdot \sigma_{\mathrm{SM}} \\ + \underbrace{\left(0 \cdot C^2_{\mathrm{SM}} + 1 \cdot C_{\mathrm{SM}}C_{tW} + 0 \cdot C^2_{tW}\right)}_{w_{\mathrm{Mix}}} \cdot \sigma_{\mathrm{Mix}} + \underbrace{\left(0 \cdot C^2_{\mathrm{SM}} - 1 \cdot C_{\mathrm{SM}}C_{tW} + 1 \cdot C^2_{tW}\right)}_{w_{tW}} \cdot \sigma_{tW}.\end{aligned} \tag{7.3}$$

The benefit of this method is that these weights only depend on the coefficients and the numerical values for the coefficients used to create the templates. For this reason, the same weights can be used for all differential cross sections (bins) of all observables (p_T, $\cos\theta_x$, etc.).

The uncertainty on the morphed prediction requires the propagation of uncertainties coming from the limited MC statistics of the templates. When all templates are independent, this leads to the following expression:

$$\delta_\sigma(C) = \sqrt{\sum_{t}^{\text{templates}} w_t^2(C) \cdot \delta^2_{\sigma_t}}, \tag{7.4}$$

where δ_σ indicates the uncertainty on the cross section. Large uncertainty can arise from the interpolation/extrapolation of templates, corresponding to large weights. To reduce this effect a proper choice of templates is important. Note that the morphing technique makes use of a matrix inversion to solve for its unknowns and therefore one can not add more templates to the morphing setup to decrease the uncertainty. The morphing procedure works with a fixed (minimal) number of unique templates.

7.2 Morphing in single top production and decay

The simple example discussed in equation 7.1 is not complete when it comes to studying the single top quark inclusively. As presented in section 1.3, there are merely three effective operators that contribute at leading order in QCD and at $O(1/\Lambda^2)$. One of these ($O_{\varphi Q}^{(3)}$) only affects the cross section and the 4-fermion ($O_{qQ,rs}^{(3)}$) has almost no effect on the polarisation angles of interest (see figures 3.12 and 3.14). As a result, only one operator (O_{tW}) remains with Wilson coefficients C_{tW} and C_{itW}.

The contribution of O_{tW} is included in the production and decay of single top quarks (figure 1.2), leading to 15 independent terms in the cross section expressed as:

$$\begin{aligned}\sigma(C_{tW}, C_{itW}) = \left| O_{\text{SM}} + \frac{C_{tW}}{\Lambda^2} \cdot O_{tW} + \frac{C_{itW}}{\Lambda^2} \cdot O_{itW} \right|^2_{\text{production}} \cdot \left| O_{\text{SM}} + \frac{C_{tW}}{\Lambda^2} \cdot O_{tW} + \frac{C_{itW}}{\Lambda^2} \cdot O_{itW} \right|^2_{\text{decay}} = \\ \tilde{O}_1 + C^1_{tW} \cdot \tilde{O}_2 + C^2_{tW} \cdot \tilde{O}_3 + C^3_{tW} \cdot \tilde{O}_4 + C^4_{tW} \cdot \tilde{O}_5 + C^1_{itW} \cdot \tilde{O}_6 + C^2_{itW} \cdot \tilde{O}_7 + C^3_{itW} \cdot \tilde{O}_8 + C^4_{itW} \cdot \tilde{O}_9 \\ + C^1_{tW} C^1_{itW} \cdot \tilde{O}_{10} + C^1_{tW} C^2_{itW} \cdot \tilde{O}_{11} + C^1_{tW} C^3_{itW} \cdot \tilde{O}_{12} + C^2_{tW} C^1_{itW} \cdot \tilde{O}_{13} + C^3_{tW} C^1_{itW} \cdot \tilde{O}_{14} + C^2_{tW} C^2_{itW} \cdot \tilde{O}_{15}.\end{aligned} \tag{7.5}$$

To reduce notational clutter, C_{SM} is set to one and all orders of Λ are absorbed in the $\tilde{O}$ terms, together with the numerical factors originating from the squaring. The inclusion of all 15 terms leads to orders in Λ that reflect the leading terms of effective operators up to dimension twelve[2]. In principle their contribution are expected to be negligible, due to the large Λ suppression. Nonetheless, all 15 terms are taken into account in order to study how the result is affected when such terms are ignored. For instance, one could question if all interference terms in the full expression of the matrix element are required. This can directly be tested using the morphing technique as is done explicitly for the interference of C_{itW} with the SM in appendix A.

The challenge is to obtain 15 samples, corresponding to the 15 terms, that allow to predict distributions for any value of the Wilson coefficients with the highest (statistical) precision. An optimisation procedure is therefore developed which is the topic of the next section.

7.3 Optimisation of the morphing templates

Deciding which set of morphing templates is best raises two important questions: what needs to be optimised and how is that implemented? In this analysis it is chosen to optimise the relative uncertainty on the total cross section, given by 7.4. This answers the first question. The second question is the focus of the remainder of this section.

In principle, a diagonal coupling matrix implies that each individual template describes one of the unknown O terms, leading to unitary weights in the morphing expression. However, these types of templates are not obtainable at NLO, they will not be gauge invariant for instance. Continuing along this reasoning, a coupling matrix that is more diagonal is expected to provide smaller uncertainties on the predictions given by the morphing. It has been shown that this is not necessarily the case [103], the reason being that large uncertainties arise when numerical values of similar size are subtracted. Hence, a robust procedure needs to be developed to select an optimal set of templates matched to relevant values of Wilson coefficients.

The adopted procedure compares the uncertainties on the predictions from different sets of morphing templates. A numerical search algorithm is exploited that minimises the maximum relative error on the cross sections in a pre-defined parameter region of interest: $-10 \leq C \leq 10$ for both C_{tW} and C_{itW}. At the point in parameter space that corresponds to the maximum relative error, a new template is created. With this new template a total of 15 additional morphing setups are constructed. This is done by replacing the new template one by one with each of the 15 existing templates, each time creating a new morphing setup. At each such setup the maximum relative error is calculated in the parameter region of interest. If one of the setups that contains the new template provides a lower maximum relative error, that setup will be used in the next iteration of the optimisation routine. This procedure continues until no further decrease in the maximum relative error is observed.

---

[2] As an example, the term $C^2_{tW} C^2_{itW} \cdot \tilde{O}_{15}$ contains a factor of $1/\Lambda^8$ which is on equal footing in terms of the EFT expansion as the interference between the SM and an effective operator of dimension twelve.

Creating a new template for each iteration takes a lot of time. To substantially reduce this time, the morphing procedure itself is exploited. Thus, instead of generating a MC template, predictions from the morphing technique are used to produce the template for the optimisation routine. This “morphed template” is ready in a matter of seconds. Both types of templates show equivalent behaviour in terms of the relative uncertainties in the parameter space of interest, as can be seen in appendix B.

An initial morphing setup is required to start the optimisation process. This initial set of templates is generated with LO precision as no large differences in terms of relative uncertainties are seen when comparing sets of morphing templates that are generated with LO or NLO precision. The verification of this can be found in appendix B.

Figure 7.2 shows the relative uncertainty on the cross section per point in the parameter space of interest for both the C_{tW} (y axis) and C_{itW} (x axis), where the red and green dots correspond to the values used for the templates. The darker regions have a larger uncertainty than the lighter regions. Two sets of morphing setups are compared. The left figure shows the setup with the templates obtained from the optimisation routine discussed above. On the right the SM is included in the templates instead of the template indicated with the green dot in the left figure. This comparison is done since a SM sample exists with large statistics and including it in the templates will remove the interpolation at the SM and thus reduce the uncertainty related to the morphing at that point in parameter space. Both setups show very similar behaviour, except that the setup with the SM, shown on the right, has a lower uncertainty near the SM (as is expected). This setup is therefore taken and the 15 templates used to extract C_{tW} and C_{itW} from the unfolded data are given in table 7.2.

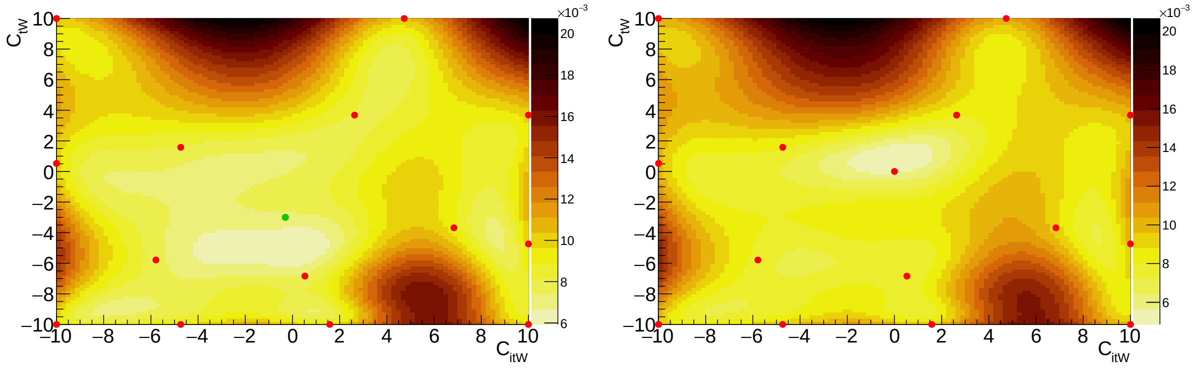

Figure 7.2: Comparing the uncertainty profile of two different morphing setups, showing the relative uncertainty from the morphing prediction on the cross section. The position of the red and green dots correspond to the values of C_{itW} (x-axis) and C_{tW} (y-axis) used for the templates. On the left the setup after the optimisation routine is given and on the right the setup where the SM is included in the templates instead of the green dot.

Template	C_{tW}	C_{itW}
0	-10	-10
1	0.53	-10
2	10	-10
3	-10	-4.74
4	1.58	-4.74
5	-5.79	-5.79
6	0	0
7	-6.84	0.53
8	-10	1.58
9	-10	10
10	-4.74	10
11	3.68	10
12	3.68	2.63
13	10	4.74
14	-3.68	6.84

Table 7.2: Table summarising the 15 templates for the morphing setup that will be used to extract C_{tW} and C_{itW} from the unfolded data.

7.4 Validation of the morphing setup

The performance of the morphing setup in terms of its uncertainty per point in EFT parameter space is shown in figure 7.2 on the right. The lightest (darkest) regions corresponds to an uncertainty of typical 1% (5%). What is interesting to note is that there are areas where the uncertainty on the prediction is smaller than at the positions of the templates (red dots). This can happen since those regions are described by multiple templates, with small interpolation weights, that effectively increase the Monte Carlo statistics.

As a next step, the morphing setup is verified by comparing its prediction for the polarisation angles with a validation sample that is part of the templates. This closure test is shown in figure 7.3, where the red band indicates the prediction by the morphing with its uncertainty and the blue points belong to the generated template. The prediction falls precisely on top of the validation and its uncertainty reflects exactly the MC statistics. This means that the weight of this template is unitary and all other template weights are zero, indicating a successful test.

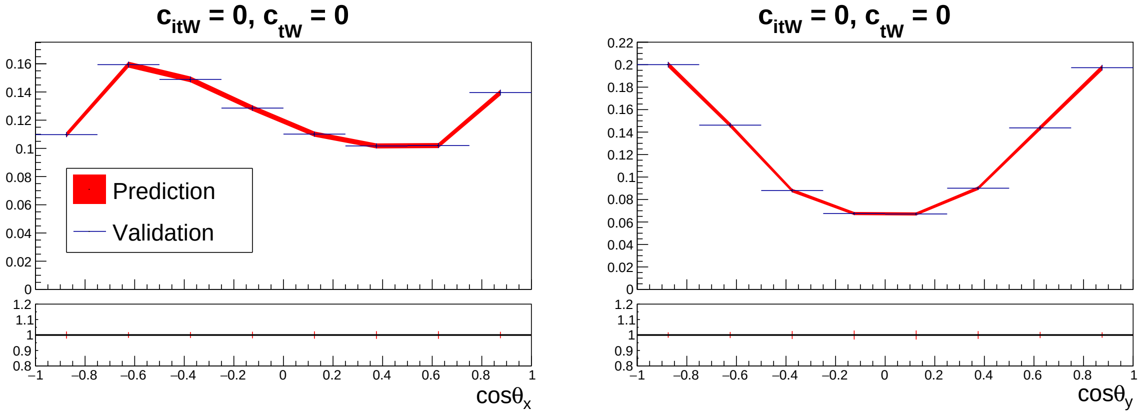

Figure 7.3: Validation of the morphing prediction for $\cos\theta_x$ *(left) and* $\cos\theta_y$ *(right) describing one of the templates. The red band shows the morphing prediction with its error, the blue points belong to the generated validation sample with coefficients* $C_{itW} = 0$ *and* $C_{tW} = 0$.

The final step is to compare the morphing prediction for $\cos\theta_x$ and $\cos\theta_y$ with validation samples that are not part of the templates. This will be done for two distinct points in parameter space: figure 7.4 shows a sample somewhat close to the SM ($C_{itW} = -0.3$ and $C_{tW} = -3$) and figure 7.5 a sample that corresponds to the location with the largest relative uncertainty ($C_{itW} = 10$ and $C_{tW} = 10$). For both good agreement is observed, as well as a reasonable uncertainty on the prediction.

The morphing setup behaves as expected and its prediction agrees well with MC validation samples. Its uncertainty is on the order of a few procent and is smallest near the SM.

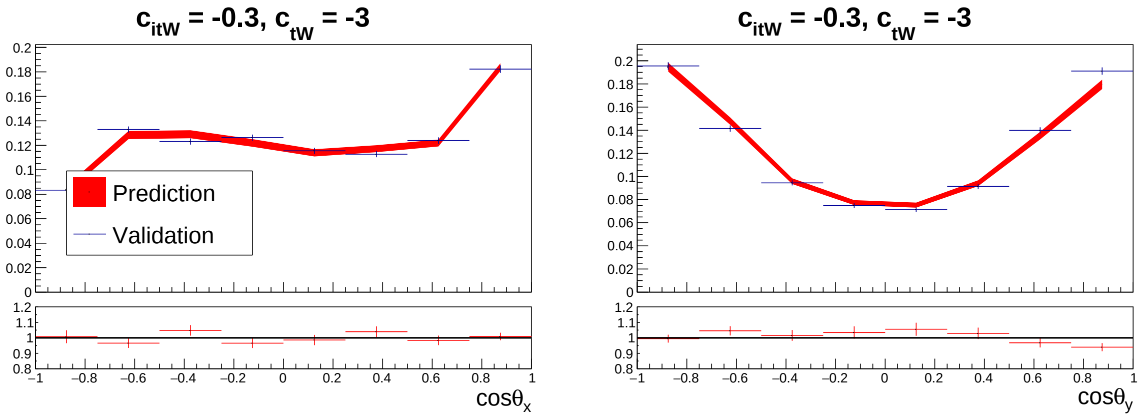

Figure 7.4: Validation of the morphing prediction for $\cos\theta_x$ *(left) and* $\cos\theta_y$ *(right) describing a point in parameter space somewhat close to the SM. The red band shows the morphing prediction with its error, the blue points belong to the generated validation sample with coefficients* $C_{itW} = -0.3$ *and* $C_{tW} = -3$.

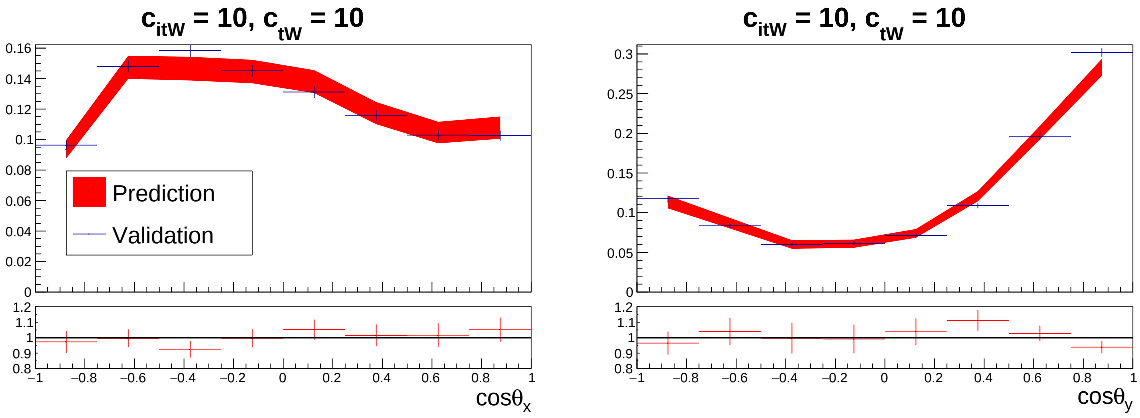

Figure 7.5: Validation of the morphing prediction for $\cos\theta_x$ *(left) and* $\cos\theta_y$ *(right) describing the point in parameter space that corresponds to the highest relative uncertainty on the cross section. The red band shows the morphing prediction with its error, the blue points belong to the generated validation sample with coefficients* $C_{itW} = 10$ *and* $C_{tW} = 10$.

Chapter 8

Extraction of EFT coefficients from the unfolded data

The normalised unfolded distributions of both $\cos\theta_x$ and $\cos\theta_y$ will be used to extract information on the C_{tW} and C_{itW} Wilson coefficients. The coefficients are obtained in a fit procedure that uses a likelihood function based on a model to describe the data. This chapter discusses the model, the validation and the results of extracting these EFT coefficients from the unfolded data. The results have been presented at the LHCP-2021 conference and a conference note is under review. A paper is in preparation.

8.1 Fit model

The coefficients are extracted by minimising the negative logarithm of the likelihood function (LH), which is the product of two probability functions:

$$\mathrm{LH} = P_{\mathrm{model}}\, P_{\mathrm{morphing}}. \tag{8.1}$$

The probability function of the model is represented by P_{model} and contains all uncertainties related to the unfolded data in a covariance matrix (as was discussed in section 6.3). These uncertainties contain: data statistics, systematic uncertainties and “unfolding MC statistics”, which arise from the limited MC statistics of the migration matrix used in the unfolding procedure. The model uses the morphing procedure for the parametric description of the EFT signal and has therefore also statistical uncertainties coming from the limited statistics of the morphing templates. These “morphing MC statistics” are described by nuisance parameters that are constrained in P_{morphing}.

Below, the ingredients of the likelihood function will be described. Several tests will be done in the next section to validate this fitting procedure.

8.1.1 The data and the covariance matrix Σ

The data is represented by the vector $\overrightarrow{\mathrm{data}}$ with 16 elements corresponding to the measured bin values of both the $\cos\theta_x$ and $\cos\theta_y$ distributions. The data (at particle level) is obtained from an unfolding procedure, leading to correlations between the bins that are included in the covariance matrix Σ with size 16×16. However, as will be discussed here, the rank (or dimension) of this matrix is only 14.

The distributions $\cos\theta_x$ and $\cos\theta_y$ are both obtained from the same dataset. Each unique event therefore appears twice in the data vector, which reduces the rank of the matrix by one. This can be seen as follows: already before normalisation, the sum of the bin contents of $\cos\theta_x$ must be exactly equal to the sum of the bin contents of $\cos\theta_y$. As a consequence, the content of one bin can always be expressed by the other bins: one bin is fully determined and therefore redundant.

The second redundant dimension is a consequence of the use of normalised distributions. When the data is normalised, the sum of the values of the 8 bins in the $\cos\theta_x$ distribution is known and thus one bin in this set becomes redundant[1]. As a result, the dimension of Σ is 14.

8.1.2 A reduced representation of the data in 14 dimensions

This paragraph discusses how the data vector $(\overrightarrow{\text{data}})$ with 16 elements and the corresponding covariance matrix Σ are represented by a vector with 14 elements and corresponding matrix of size 14×14, in accordance with the number of dimensions.

Every diagonalisable matrix can be factorised in terms of eigenvectors (U) and eigenvalues as given by:

$$\Sigma = U \cdot D \cdot U^T, \tag{8.2}$$

where the matrix D contains the eigenvalues as elements on its diagonal. Redundant dimensions can now be taken care of by removing the eigenvectors that correspond to the eigenvalues that are zero. The procedure of removing two eigenvectors from the full covariance matrix is shown in equation 8.3, where the dimensions of the matrices are shown between the brackets together with the transformation of the model on the second line.

$$\begin{aligned} \Sigma_{(16,16)} &= U_{(16,14)} \cdot D_{(14,14)} \cdot U^T_{(14,16)} \\ \left(\overrightarrow{\text{model}} - \overrightarrow{\text{data}}\right) \cdot U_{(16,14)} &= \vec{\mu}' \end{aligned} \tag{8.3}$$

The model in P_{model} can now represented by $\vec{\mu}'$ which contains 14 elements that would be all zero when the model exactly describes the data. Or in other words, non-zero values imply a difference between the data and the prediction. The covariance matrix then becomes $D' = D_{(14,14)}$ which is a diagonal matrix of size 14×14.

8.1.3 The probability density function P_{model}

The probability density function (pdf) is assumed Gaussian and is obtained from the reduced data representation by:

$$P_{\text{model}}(\overrightarrow{\text{data}}; \overrightarrow{\text{model}}, \Sigma) = \frac{1}{\sqrt{(2\pi)^{14}|D'|}} \exp\left\{-\frac{1}{2}\left(\vec{\mu}'\right)^T \cdot \left(D'\right)^{-1} \cdot \left(\vec{\mu}'\right)\right\}, \tag{8.4}$$

where the relation between the vectors and the matrix on the left-hand side to those on the right-hand side are given in equation 8.3.

8.1.4 The model

The model is represented by the vector $\overrightarrow{\text{model}}$ with 16 elements corresponding to the bin values of the predictions for both the $\cos\theta_x$ and $\cos\theta_y$ observables. As discussed in section 7.2, each bin can be described by a weighted sum over all the morphing templates. Normalisation of the predicted distributions depend on the coefficients that vary during the fitting procedure. Therefore, the normalisation is build into the model:

$$\overrightarrow{\text{model}} = \begin{bmatrix} \mu_{X1} \\ \vdots \\ \mu_{X8} \\ \mu_{Y1} \\ \vdots \\ \mu_{Y8} \end{bmatrix} \rightarrow \mu_{\rho_b} = \frac{1}{N_\rho}\left(\sum_t^{\text{templates}} w_t\left(C_{tW}, C_{itW}\right) \cdot \alpha_{\rho_b t}\right), \tag{8.5}$$

where $w_t\left(C_{tW}, C_{itW}\right)$ corresponds to the weight of template t and $\alpha_{\rho_b t}$ is the value of bin b from observable ρ and template t. Both observables have the same normalisation N_ρ which is obtained from a sum over all the bins from one observable:

---

[1] Note that the same argument does not hold for the 8 bins of $\cos\theta_y$, which would lead to another redundant dimension. The double usage of events used in the first argument, correlates the two histograms and is already accounted for.

$$\mathcal{N}_\rho = \sum_b^{\text{bins in }\rho} \sum_t^{\text{templates}} w_t\left(C_{tW}, C_{itW}\right) \cdot \alpha_{\rho_b t}. \tag{8.6}$$

8.1.5 Morphing uncertainties

Uncertainties originating from the morphing are incorporated by letting each α float within its corresponding uncertainty arising from the limited MC statistics. This is similar to the full Beeston Barlow method [104], where each bin from each (background) sample is described by a separate nuisance parameter. In this way the uncertainty on the model depends on the EFT coefficients encoded in the weights, fully including the interpolation uncertainty (seen in figure 7.2). This results in a total of 240 α nuisance parameters, coming from 15 independent templates distributed over two 8 bin histograms ($\cos\theta_x$ and $\cos\theta_y$).

The α parameters from the same template are statistically correlated between $\cos\theta_x$ and $\cos\theta_y$. In order to include these correlations consistently, a covariance matrix Σ_t^{MC} is constructed for each template t. It should be noted that the α parameters (bins) of the same observable are not correlated[2], only between the different polarisation angles there are correlations.

8.1.6 Features of Σ_t^{MC}

Also in the case of each covariance matrix that belongs to a template (Σ_t^{MC}), the usage of both $\cos\theta_x$ and $\cos\theta_y$ from the same dataset leads to one redundant dimension. As explained in section 8.1.4, the normalisation is implemented in the model itself. The α parameters therefore come from unnormalised templates. As a result, unlike Σ with two zero eigenvalues, each Σ_t^{MC} has one zero eigenvalue.

This redundant dimension could again be removed via eigendecomposition, however this tremendously increases the computation time on the minimisation of the negative-log likelihood[3]. For this reason, the first bin of $\cos\theta_x$ (α_{X1}) of each template is removed by expressing it in terms of the remaining other α parameters of that template:

$$\alpha_{X1} = \sum_{b=1}^{8} \alpha_{Yb} - \sum_{b=2}^{8} \alpha_{Xb}. \tag{8.7}$$

As a result, the total number of independent α parameters becomes 225: 15 inputs with 15 independent bins.

8.1.7 The probability density function P_{morphing}

The number of events in each bin of the morphing templates is large and therefore the statistical uncertainty is assumed Gaussian. In order to include the statistical correlation between the bins in $\cos\theta_x$ and $\cos\theta_y$, the α nuisance parameters are constrained with a multi variate Gaussian pdf per template. The full probability function becomes:

$$P_{\text{morphing}} = \prod_t^{\text{templates}} \frac{1}{\sqrt{(2\pi)^{15}|\Sigma_t^{\prime\text{MC}}|}} \exp\left\{-\frac{1}{2}\left(\vec{\alpha}_{0t} - \vec{\alpha}_t\right)^T \left(\Sigma_t^{\prime\text{MC}}\right)^{-1} \left(\vec{\alpha}_{0t} - \vec{\alpha}_t\right)\right\}, \tag{8.8}$$

where the vectors $\vec{\alpha}_{0t}$ and $\vec{\alpha}_t$ are of size 15 and contain the nominal bin values of template t and the corresponding independent nuisance parameters, respectively. The corresponding covariance matrix $\Sigma_t^{\prime\text{MC}}$ is of size 15×15.

8.1.8 Full likelihood

All ingredients of the likelihood given in equation 8.1 are discussed in the paragraphs above. For completeness the full likelihood is given in equation 8.9, where the separate components are indicated.

---

[2] Statistical bins in a histogram are uncorrelated.

[3] Each template has its own Σ_t^{MC} and thus produces its own transformation. This leads to large expressions in the model causing a huge (unnecessary) increase in computation time.

$$\mathrm{LH} \propto \underbrace{\exp\left\{-\frac{1}{2}\left(\vec{\mu}'\right)^T \left(D'\right)^{-1}\left(\vec{\mu}'\right)\right\}}_{P_{\text{model}}} \cdot \underbrace{\prod_t^{\text{templates}} \exp\left\{-\frac{1}{2}\left(\vec{\alpha}_{0t}-\vec{\alpha}_t\right)^T\left(\Sigma_t'^{\text{MC}}\right)^{-1}\left(\vec{\alpha}_{0t}-\vec{\alpha}_t\right)\right\}}_{P_{\text{morphing}}} \qquad (8.9)$$

The extraction of both Wilson coefficients is done by minimising the negative-logarithm of the full likelihood, expressed in equation 8.9, with respect to all the nuisance parameters. This procedure is usually referred to as fitting.

8.2 Validation

The full likelihood and all its ingredients are discussed in the previous section. This section focuses on testing the fitting procedure and its implementation. The fit model is confronted with several samples generated with non-zero values for the Wilson coefficients. Furthermore, a study is performed to quantify the importance of the Λ terms in the EFT expansion.

8.2.1 Asimov fit

Creating a dataset from the model itself is commonly referred to as an Asimov dataset. It is prepared such that the $\cos\theta_x$ and $\cos\theta_y$ distributions exactly match the model, but each bin gets the uncertainty (and correlations) of the genuine measured data (see section 6.3). Perfect agreement is therefore expected when fitting to an Asimov dataset, as well as no shifts (pulls) of any parameters. Furthermore, it provides the expected uncertainty on the final result as all uncertainties from the genuine measured data are included.

Figure 8.1 gives the post-fit distributions of both polarisation angles under study. The black points corresponds to the Asimov dataset and the red dashed line is the result of the model after the fit. Perfect agreement between data and the model is observed. The obtained values for the Wilson coefficients are presented in figure 8.2, where no pulls are immediately apparent.

The expected uncertainty is $C_{tW} = [\pm 0.5]$ and $C_{itW} = [\pm 0.2]$ both at 68.3% confidence level (CL). This is promising since the current best limits are $C_{tW} \in [-0.4, 0.5]$ at 95% CL [32], although here C_{itW} is assumed zero, and $C_{itW} \in [-0.8, 0.7]$ at 95% CL [105].

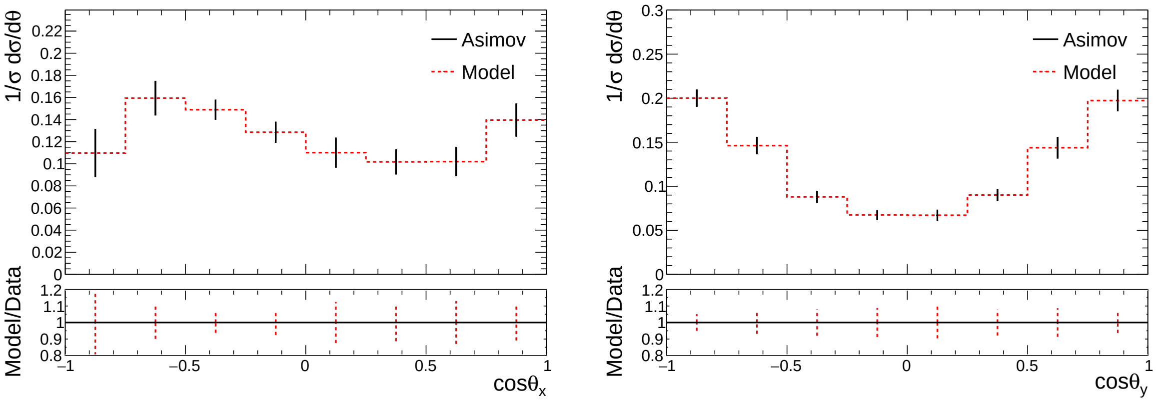

Figure 8.1: Fit result on the Asimov dataset with respect to $\cos\theta_x$ (left) and $\cos\theta_y$ (right). The black points show the Asimov data points and the red dashed line corresponds to the model after the fit. The lower inset gives the ratio between data and model.

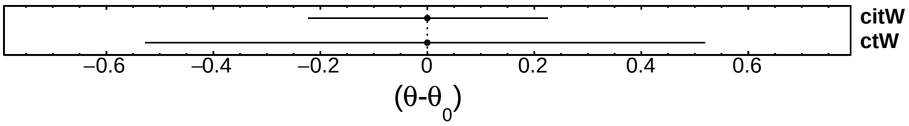

Figure 8.2: Asimov fit result showing the 1σ total expected uncertainty.

As discussed in the previous section (8.1.2), the model is transformed to its eigenvector representation (according to equation 8.3). Figure 8.3 shows this representation where each bin corresponds to an orthogonal dimension, meaning that there are no correlations between them. It should be noted that in the transformation it has been chosen to subtract the data directly[4], perfect agreement with data corresponds therefore to a value of zero.

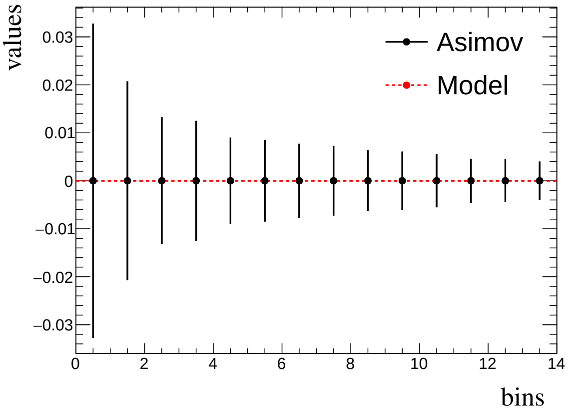

Figure 8.3: Fit result on the Asimov dataset given in the eigenvector representation (μ') defined by equation 8.3. In this representation there are no correlations between the bins.

To study the shape of the likelihood, a scan is done where one parameter is fixed over a certain range of values. At each point in the scan, the negative-logarithm of the LH is minimised (profiled) with respect to all non-fixed fit parameters. The difference with the minimum value obtained in the scan is shown in figure 8.4, where nice parabolic shapes are observed. The red vertical line indicates the result obtained from the best-fit where no parameters are fixed. It resides perfectly in the minimum of the scan which is an indication of proper fit behaviour.

The correlation between the two parameters of interest (POIs) can be investigated with a two dimensional likelihood scan. Here both coefficients are fixed over a certain range of values and only the nuisance parameters are left floating in the minimisation of the negative-logarithm of the LH at each point in the scan. The result is shown in figure 8.5, where a circular shape is observed indicating that there is no large correlation between the POIs. This is expected since figures 3.12 and 3.14 showed that each coefficient mostly affects a different observable.

The impact that different uncertainty sources have on the total expected uncertainty is presented in figure 8.6. Here four distinct categories are defined: *Sys*, *Stat*, *Unfolding* and *Morphing*. *Sys* contains all the systematic uncertainty sources, *Stat* corresponds to the data statistics and *Unfolding* contains the limited MC statistics from the background and signal samples used in the unfolding (more info can be found in section 6.3). The contribution of these categories are estimated by removing their corresponding uncertainty from the covariance matrix used in the fitting procedure. The fourth category, *Morphing*, corresponds to the MC statistics used in the templates, implemented as nuisance parameters as explained in section 8.1.5. At each entry in the figure the contribution to the total uncertainty (σ) is shown per particular category for C_{tW} (left) and C_{itW} (right). It can be seen that this analysis is dominated by systematics.

---

[4] Another possibility is to transform the data according to the same eigenvector as the model.

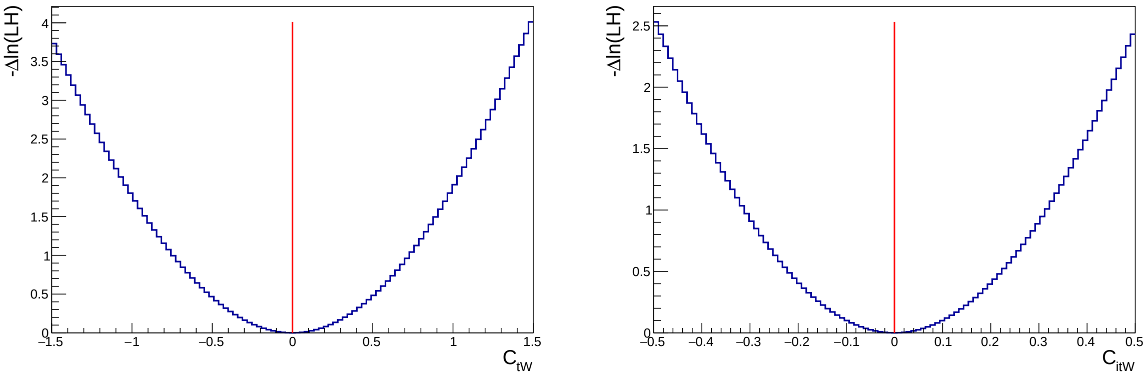

Figure 8.4: Likelihood scans of C_{tW} (left) and C_{itW} (right) using an Asimov dataset. Both separate scans are profiled which means that at each point the negative-logarithm of the LH is minimised. The red vertical line indicates the result obtained from the best-fit.

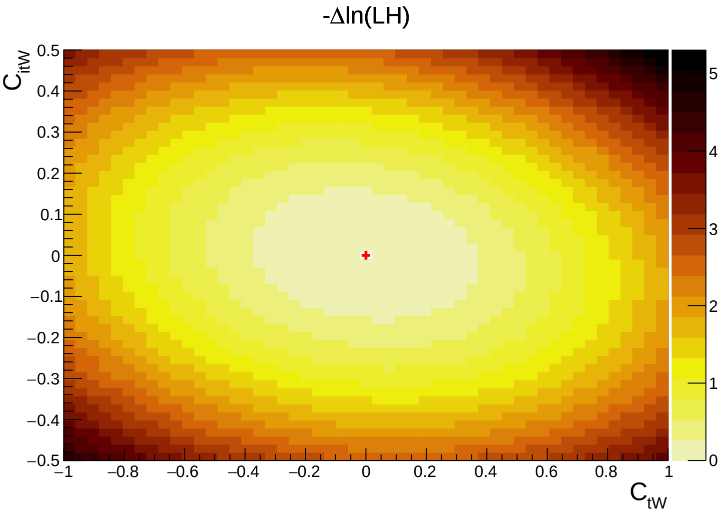

Figure 8.5: The two dimensional likelihood scan of the Wilson coefficients under study using an Asimov dataset. The scan is profiled which means that at each point the negative-logarithm of the LH is minimised with respect to the nuisance parameters.

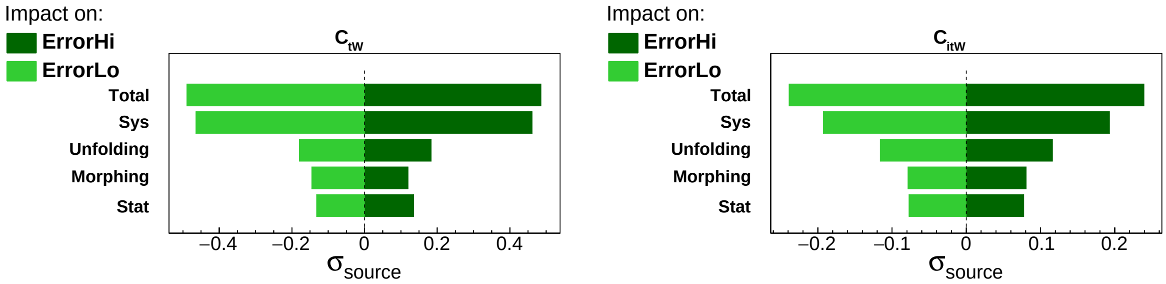

Figure 8.6: Uncertainty impact study. The change on the total uncertainty (σ) is shown for C_{tW} (left) and C_{itW} (right) when that particular category of uncertainty is not included in the fit. This is an estimate for “Sys”, “Stat” and “Unfolding” as the separate uncertainty sources are not accessible from the combined covariance matrix.

It can be concluded that the fit behaves as expected during the Asimov test. In the next paragraph the Gaussian behaviour of the uncertainties on the parameters (from the fitting procedure) are verified making use of pseudo-data (toys).

8.2.2 Toy study

To test if there is no bias in the fitting procedure, as well as to verify the Gaussian behavior of the uncertainties on the fit parameters, pseudo-data (toys) are exploited. A toy is obtained by letting the value in each bin fluctuate within its allowed uncertainty, where the correlations between bins are consistently taken into account. Figure 8.7 shows the fit result from 10k toys (blue points), together with a Gaussian curve (red).

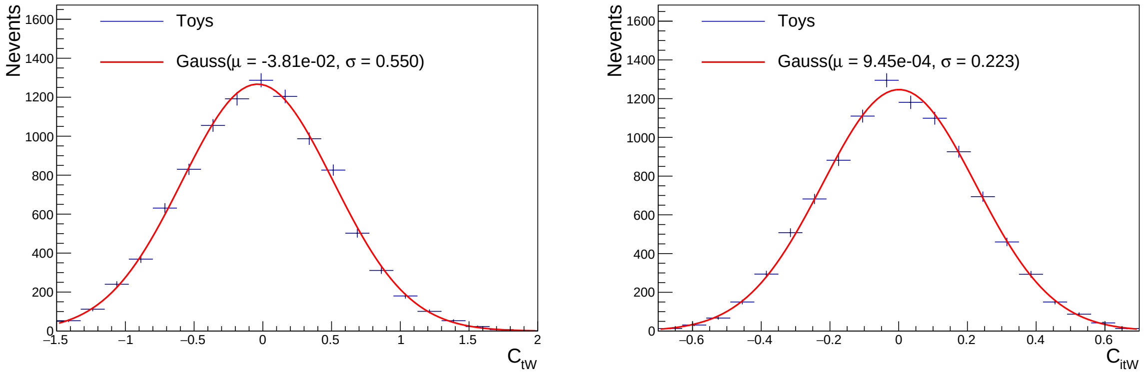

Figure 8.7: Fit validation with 10k toys.

It can be observed that the toy result has the expected Gaussian shape with a negligible bias. Furthermore, the width of the Gaussians (as listed by σ in the legend of the figure) agrees well with the uncertainty obtained from the Asimov fit in the previous section. In the following paragraph, fits will be done on validation samples from which the results can be directly compared to the values used to generate these samples.

8.2.3 Closure test

Another test is to use generated samples with non-SM coefficients as pseudo-data. For this closure test the same benchmark values for the Wilson coefficients are used as given in table 3.2. In order to make a fair comparison, only the relevant uncertainties will be taken into account in this study. This means that no unfolding and no systematic uncertainties are included since the fits are performed directly on particle level distributions of the generated MC validation samples. Hence, only the statistical uncertainties related to limited MC statistics of the simulated validation sample, including the correlation between both polarisation angles, is used together with the uncertainty from the morphing.

The difference between the obtained values for the Wilson coefficients (θ) and those used to generate the benchmark validation samples (θ_0) are shown in figures 8.8 and 8.9 for C_{tW} and C_{itW}, respectively. Each entry in the figure presents the result when fitted to that particular MC dataset indicated on the y-axis. As an example for the notation used on the y-axis, the top entry corresponds to the validation sample generated with $C_{itW} = -1.75$ and $C_{tW} = 2$. One should keep in mind that the error-bars represent real statistical uncertainties and thus that outliers can happen.

In both figures the validation sample with SM values is shown at the bottom. The results for C_{tW} and C_{itW} are in perfect agreement as this MC sample is part of the morphing templates. The results for other benchmark samples are also shown and are consistent with zero.

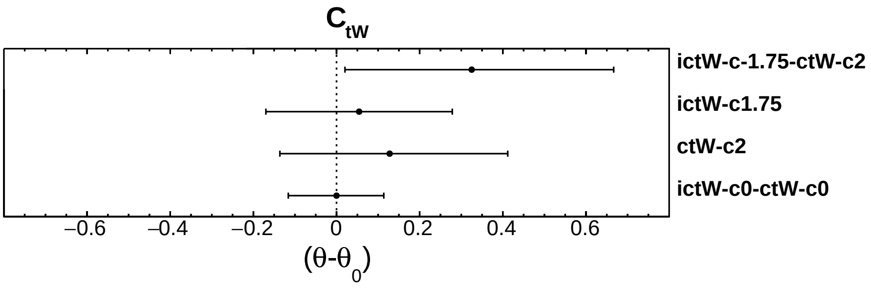

Figure 8.8: Closure tests for extracting C_{tW} from a fit to four benchmark MC validation samples indicated on the y-axis. Each entry shows the difference between the obtained value for C_{tW} (θ) and the one used to generate the validation sample (θ_0).

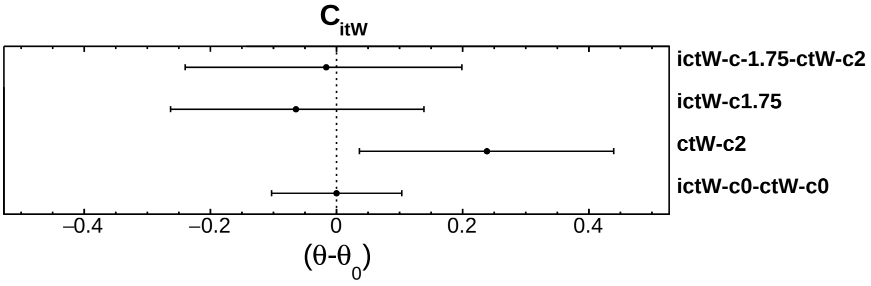

Figure 8.9: Closure tests for extracting C_{itW} from a fit to four benchmark MC validation samples indicated on the y-axis. Each entry shows the difference between the obtained value for C_{itW} (θ) and the one used to generate the validation sample (θ_0).

8.2.4 Robustness at particle level

The single top polarisation angles are expected to depend only on O_{tW} as was discussed in section 7.2. This presumption is further tested in this paragraph, which studies validation samples with non-zero coupling values for other dimension-6 effective operators. Table 8.1 summarises the choices of Wilson coefficients based on their current best limits.

Operator	Coupling value	Based on citation
O_{tG}	$C_{tG} = 0.82$	95% CL [32]
O_{bW}	$C_{bW} = 2.64$	95% CL [32]
	$C_{ibW} = 1.32$	90% CL [106]
$O_{\phi\phi}$	$C_{\phi\phi} = 8.82$	95% CL [32]
	$C_{i\phi\phi} = 5.29$	90% CL [107]

Table 8.1: Benchmark EFT samples to test the robustness of the model. The choices for the values have been based on the current best limits.

Figure 8.10 shows the NLO distribution of the polarisation angles in the Signal Region of these EFT samples together with the SM. No shape differences with respect to the SM are observed. Additionally samples with two non-zero Wilson coefficients have been generated, which are shown in figure 8.11. Here the yellow dash-dotted line does show a deviation from the SM in the $\cos\theta_y$ distribution (right). This is not surprising as it contains a non-zero value for C_{itW}.

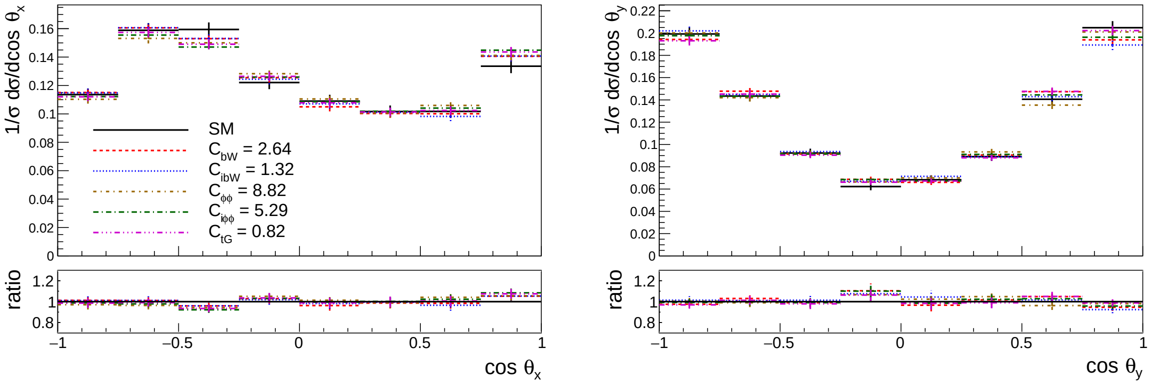

Figure 8.10: The normalised NLO distributions in the Signal Region of the 13 TeV polarisation measurement [87] of the top polarisation angles for the SM and effective operators. The ratio shown in the lower inset is defined as the effect of the operator over the SM.

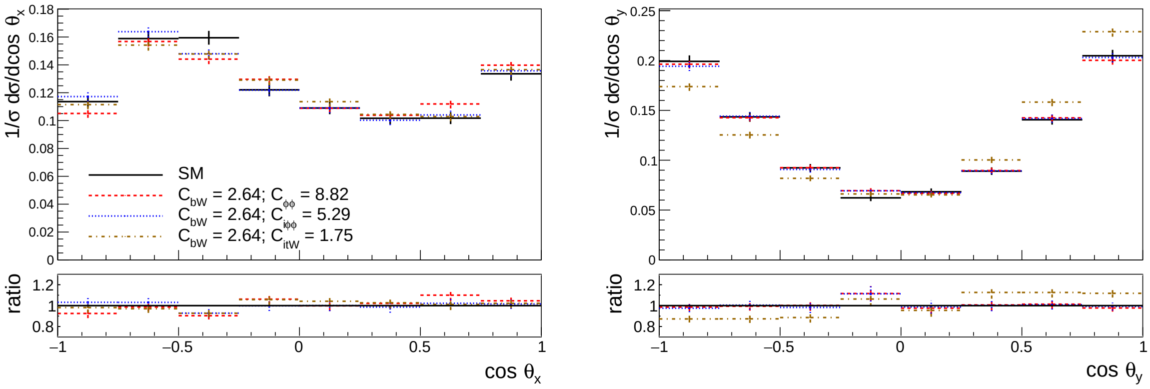

Figure 8.11: The normalised NLO distributions in the Signal Region of the 13 TeV polarisation measurement [87] of the top polarisation angles for the SM and effective operators. The ratio shown in the lower inset is defined as the effect of the operator over the SM.

Figures 8.12 and 8.13 show the obtained fit values for C_{tW} and C_{itW}, respectively. Each entry presents the result when fitted to that particular MC dataset shown on the y-axis, where the benchmark sample for the 4-fermion operator (here indicated by C_{4f}) is also presented. As an example for the notation used on the y-axis, the top entry corresponds to the sample generated with $C_{bW} = 2.64$ and $C_{itW} = 1.75$ and the coefficient of the operator $O_{\phi\phi}$ is indicated by C_{ff}. Again only the relevant uncertainties are included in these fits: the morphing uncertainty together with the statistical uncertainty corresponding to the limited MC statistics of the validation sample. The total expected uncertainty on the parameters of interest, obtained from the Asimov fit containing all uncertainties, are given by the green (1σ) and yellow (2σ) bands.

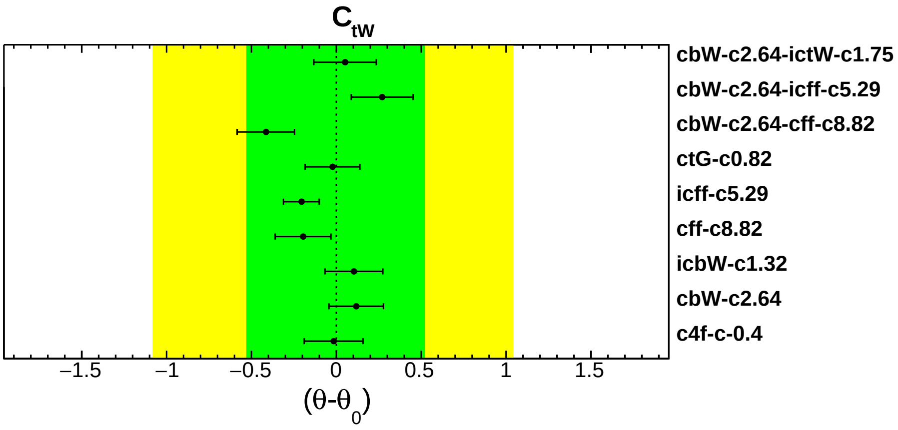

Figure 8.12: Robustness test for C_{tW} with respect to MC samples generated with the non-zero Wilson coefficients indicated on the y-axis. Each entry shows the difference between the obtained value for C_{tW} (θ) and the one used to generate the validation sample (θ_0). The green and yellow band show the expected 1σ and 2σ uncertainty.

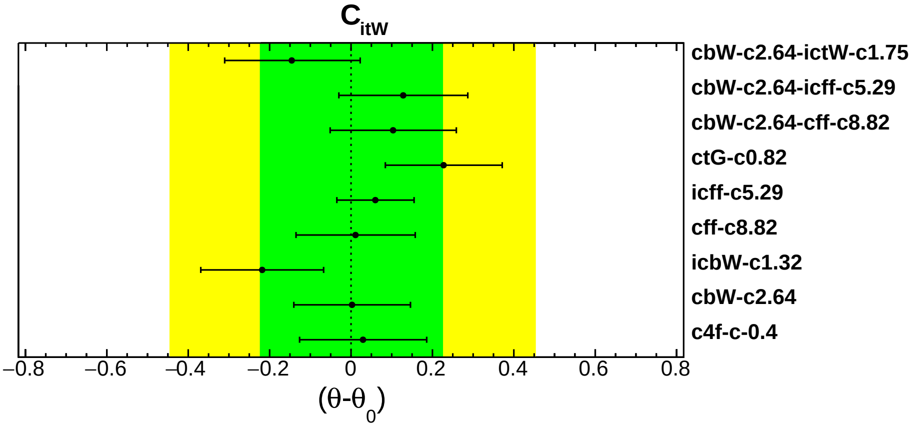

Figure 8.13: Robustness test for C_{itW} with respect to MC samples generated with the non-zero Wilson coefficients indicated on the y-axis. Each entry shows the difference between the obtained value for C_{itW} (θ) and the one used to generate the validation sample (θ_0). The green and yellow band show the expected 1σ and 2σ uncertainty.

Most pulls are consistent with zero and everything falls within the expected uncertainty (green and yellow band), implying that this setup suffices with the current precision. The fact that some pulls deviate from zero does point out that in further interpretations, with improved uncertainties, these effective operators should be taken into account.

8.2.5 Cut-offs in Λ

As discussed in section 7.2, there are many orders in Λ included in the nominal fit. These terms are often not taken into account due to the large suppression factors. In this paragraph validation fits to MC samples will be done when certain cut-offs in Λ are applied by setting the corresponding O terms to zero in the morphing expression. Table 8.2 summarises the available cut-offs, where the orders in Λ are presented in terms of $1/\Lambda^2$ because that corresponds to the leading term when dimension-6 operators are involved. As a reminder, in this work Λ has been set to 1 TeV.

Name	Including up to	Terms in $\lvert\mathcal{M}\rvert^2$
Linear	$1/\Lambda^{2\cdot 1}$	3
Squared	$1/\Lambda^{2\cdot 2}$	6
Cubed	$1/\Lambda^{2\cdot 3}$	10
Nominal	$1/\Lambda^{2\cdot 4}$	15

Table 8.2: Summarising the available setups where a particular cut-off in Λ is applied. The orders in Λ are presented in terms of $1/\Lambda^2$ because that corresponds to the leading term when dimension-6 effective operators are involved.

Figures 8.14 and 8.15 compare the obtained values and uncertainties for C_{tW} and C_{itW}, respectively, when certain cut-offs in Λ are considered. The same four different benchmark samples are studied, as was done in the closure tests, each generated with a different set of coupling values given in table 3.2. Each entry in the figure presents the result from four different setups, with a certain Λ cut-off, when fitted to that particular MC dataset indicated on the y-axis. As an example for the notation used on the y-axis, the top entry corresponds to the validation sample generated with $C_{itW} = -1.75$ and $C_{tW} = 2$. In these tests the systematic uncertainties are taken into account and the expected values from the generation of the validation samples are not subtracted from the result.

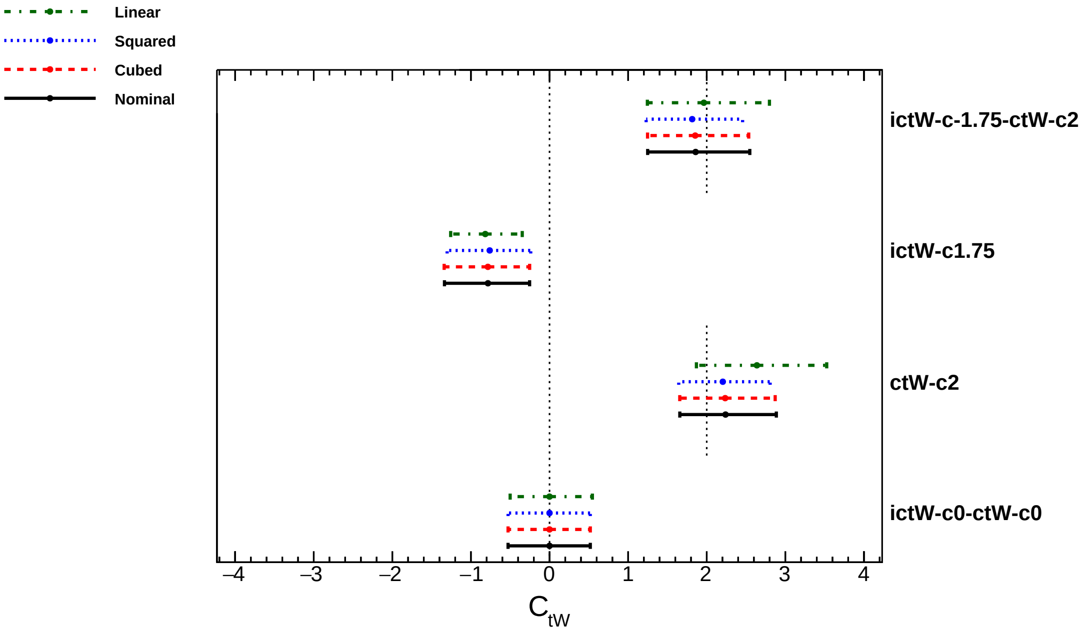

Figure 8.14: Comparison of MC validation fit results of C_{tW} when certain cut-offs in Λ are applied.

There is good sensitivity for these non-zero Wilson coefficients and all setups are more or less consistent with each other. For the SM validation sample (shown at the bottom), the difference between including only the linear terms (green dash-dotted) and the all terms (black solid) is in fact negligible. However, when non-zero couplings are involved this is not always the case. Overall it seems that including up to the squared terms (blue dotted) is sufficient.

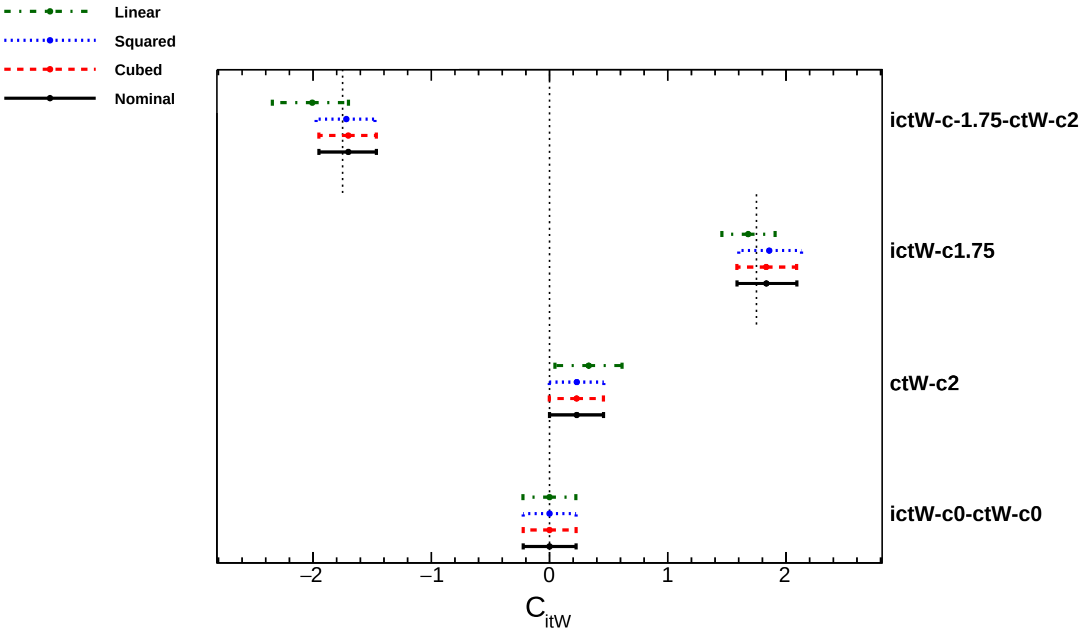

Figure 8.15: Comparison of MC validation fit results of C_{itW} when certain cut-offs in Λ are applied.

Most EFT interpretations make an assumption on how many orders of Λ are included. This is the first time that it is possible to study what such an assumption implies. As expected, when results turn out to be close to the SM only including the linear terms seem to be sufficient. Even further away from the SM, the linear results remain more or less consistent with the other setups. However, if possible, it is better to go one step further and include up to the squared terms.

8.2.6 Conclusion

It can be concluded that the fit procedure behaves as expected. The likelihood scans have a nice parabolic shape and its minimum and width correspond to the best-fit result and uncertainty. Generating and fitting 10k toy datasets shows that no bias in the fit procedure is present. Furthermore, results from fitting to MC validation samples are consistent with the values for the coefficients set in the generation.

It is practically inevitable to make assumptions about other EFT operators when certain coefficients (in this case C_{tW} and C_{itW}) are extracted. Stress testing the assumptions by fitting to MC samples with non-zero EFT (typically set to their 2 σ uncertainty) has shown relatively small sensitivity to their values and the effects appear to be covered by the expected uncertainty. Based on the physics arguments discussed in section 1.3.2 and the results presented here, the conclusion is that C_{tW} and C_{itW} can indeed be extracted from the $\cos\theta_x$ and $\cos\theta_y$ distributions. Last, but not least, all orders of the EFT expansion are kept making it possible to compare for the first time how the interpretation result is affected when certain terms are excluded in the fit. Overall it suffices when up to the squared terms are taken into account.

8.3 Results

The previous two sections discussed the fit model and its validation. In this section the extraction of C_{tW} and C_{itW} from the data recorded with the ATLAS detector in the years 2015 until 2018, corresponding to a luminosity of about 139 fb^{-1}, is presented.

The result of the simultaneous fit of both C_{tW} and C_{itW} is shown in figure 8.16, where a good agreement between the model and the data is observed. The best fit values for the coefficients are: $C_{tW} = 0.4 \pm 0.5$ and $C_{itW} = -0.3 \pm 0.2$ at 68.3% CL, which is consistent with the SM as shown in figure 8.17.

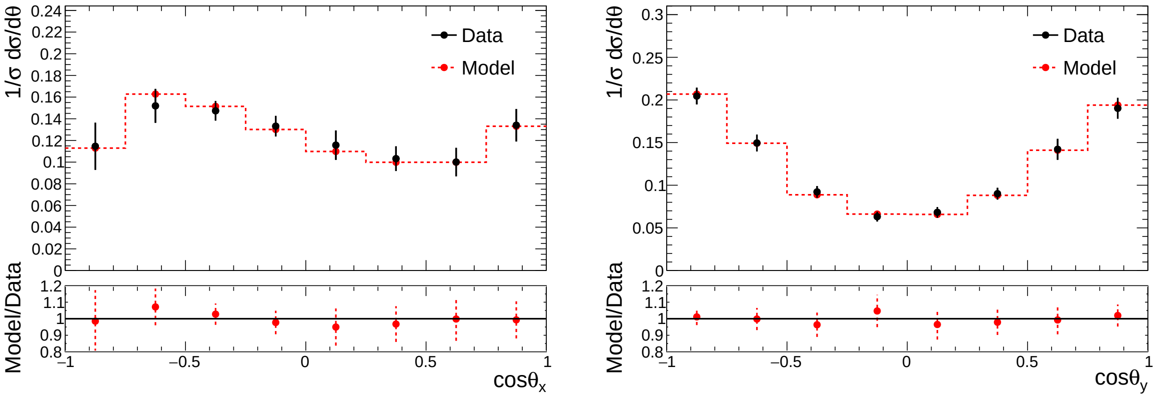

Figure 8.16: Fit result with respect to both polarisation angles $\cos\theta_x$ *(left) and* $\cos\theta_y$ *(right). The solid line shows the data and the dashed line corresponds to the model. The lower pad gives the ratio between data and model.*

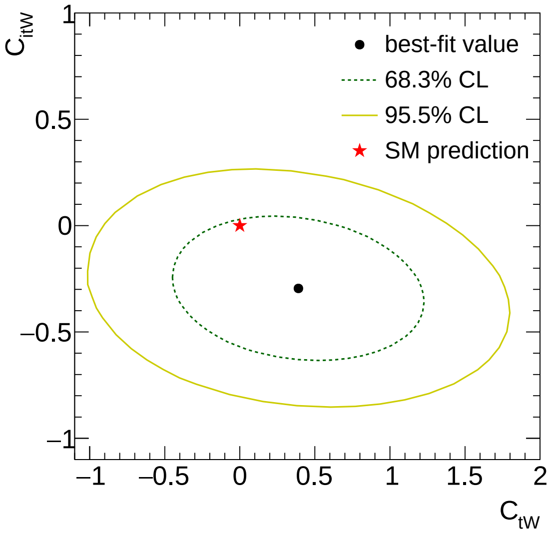

Figure 8.17: The observed best-fit value (dot) for the C_{tW} *(x-axis) and* C_{itW} *(y-axis) with the uncertainty contours at 68% CL (dashed) and 95% CL (solid). The cross indicates the SM prediction.*

The obtained limits for the coefficients at 68.3% CL and 95.5% CL are given in table 8.3. The limits on C_{tW} are comparable with the results of EFT fits in the top sector [32, 108, 109] that include the polarisation in single-top production [105] and the bounds obtained from W boson helicity measurements in top decay [110]. Very stringent individual limits on C_{itW} exist from EDM analyses [64], but these tend to become much weaker in a multi-parameter fit. The limit presented in this work is more stringent than the marginalised bounds in Ref. [64] and is the best limit obtained from high-energy experiments.

	C_{tW}		C_{itW}	
	68.3% CL	95.5% CL	68.3% CL	95.5% CL
All terms	[-0.2, 0.9]	[-0.7, 1.5]	[-0.5, -0.1]	[-0.7, 0.2]
Order $1/\Lambda^4$	[-0.2, 0.9]	[-0.7, 1.5]	[-0.5, -0.1]	[-0.7, 0.2]
Order $1/\Lambda^2$	[-0.2, 1.0]	[-0.7, 1.7]	[-0.5, -0.1]	[-0.8, 0.2]

Table 8.3: Obtained limits on the real (C_{tW}) and imaginary (C_{itW}) coefficient of the O_{tW} operator. Also shown are the limits when only the terms up to a specific order in Λ are taken into account.

Also given in the table are the limits when a certain cut off on the order of Λ is applied. It is observed that including terms up to $1/\Lambda^4$ is sufficient, which corresponds to the squared terms of a dimension-six coefficient. This is the first time that the usual assumption to exclude terms beyond $1/\Lambda^4$ is validated.

Chapter 9

Study on the effects from systematic uncertainties

The fit model discussed in the previous chapter has all the systematic uncertainties included in the covariance matrix. In this approach the effects from individual systematic sources, which are the most dominant for the total uncertainty on the Wilson coefficients (as seen in figure 8.6), are not accessible. For this reason, in this chapter an alternative fit model is exploited to provide more insight on the effects from individual systematic uncertainties. This model is called the "hybrid model" and yields similar results as the matrix method of the previous chapter when asymmetric systematic uncertainties are treated equivalently.

9.1 The hybrid model

The effect of each individual systematic source on the shape of the $\cos\theta_x$ and $\cos\theta_y$ distributions is known and can be fitted to the data. This is done by implementing the strength of their effect as nuisance parameters, one for each source. Other uncertainties, such as the statistical uncertainty, remain in the covariance matrix. Hence, this model is referred to as the hybrid model.

Compared to the previous model, which shall be referred to as the "matrix model", more detailed information becomes available, such as the size of the pull or constraint per systematic source, as well as the impact that each source has on the obtained values for the Wilson coefficients. The likelihood of the hybrid model is now a product of three probability functions:

$$\mathrm{LH}_{\mathrm{hybrid}} = P_{\text{hybrid model}}\, P_{\text{morphing}}\, P_{\text{sys}}, \tag{9.1}$$

where the most notable difference with the matrix model is that the systematic uncertainties are no longer included in the covariance matrix of $P_{\text{hybrid model}}$ but are expressed by nuisance parameters that are constrained in P_{sys}. The component related to the morphing (P_{morphing}) is the same as it is in the matrix model and is described in section 8.1.7.

In this section the ingredients of the likelihood function for the hybrid model will be described. A comparison with the matrix model will be done in the next section to validate this alternative model.

9.1.1 Ingredients of $P_{\text{hybrid model}}$

To incorporate the systematic uncertainties in the model, each morphing expression for a bin (b) is scaled with the relative effect from systematic variations. A bin in the hybrid model therefore reads:

$$\mu_b = \frac{1}{\mathcal{N}_\rho}\left(\sum_t^{\text{templates}} w_t\left(C_{tW}, C_{itW}\right)\cdot \alpha_{tb}\cdot\left(1+\sum_s^{\text{systematics}} \theta_s\cdot\Delta_{sb}\right)\right), \tag{9.2}$$

where both observables have the same normalisation $\mathcal{N}_\rho$ which is obtained from a sum over all the bins from one observable:

$$\mathcal{N}_\rho = \sum_{b}^{\text{bins in }\rho} \left(\sum_{t}^{\text{templates}} w_t \left(C_{tW}, C_{itW}\right) \cdot \alpha_{tb} \cdot \left(1 + \sum_{s}^{\text{systematics}} \theta_s \cdot \Delta_{sb}\right)\right). \tag{9.3}$$

Per systematic source (s) there is a nuisance parameter θ_s and a response function Δ_{sb}, which is defined as the relative difference between the nominal distribution (N) and the variation (V):

$$\Delta_{sb} = \frac{V_{sb} - N_b}{N_b}. \tag{9.4}$$

For systematic sources that have an asymmetric variation, the response function can contain both these contributions:

$$\Delta_{sb} = \begin{cases} \Delta^+_{sb} & \text{if } \theta > 0 \\ \Delta^-_{sb} & \text{if } \theta < 0 \end{cases}, \tag{9.5}$$

where Δ^+ and Δ^- correspond to the up and down response functions, respectively.

Uncertainties related to the choice of the parton density function (PDF) are obtained by taking the average of multiple different PDF sets and remain in the covariance matrix. Additionally, the contributions from b-tagging and lepton scale factors are estimated to be small and remain in the covariance matrix to reduce the time it takes for the hybrid model fit to converge.

By definition, asymmetric uncertainty sources are symmetrised in the covariance matrix. To be able to compare the hybrid model to the matrix model, asymmetric response functions need to be symmetrised in a similar manner. This will be discussed in the next paragraph.

9.1.2 Symmetrisation of asymmetric variations

In the construction of the covariance matrix each systematic uncertainty fluctuates independently. This corresponds to adding the separate contributions in quadrature preserving the correlations between the bins. Mathematically the contribution to the covariance matrix from one uncertainty source (Σ_{sys}) can be written as:

$$\begin{aligned} \Delta &= \hat{V} - \hat{N}, \\ \Sigma_{\text{sys}} &= \Delta \cdot \Delta^T, \end{aligned} \tag{9.6}$$

where $\hat{V}$ and $\hat{N}$ are vectors corresponding to the unfolded variation and nominal, respectively. Both vectors have 16 elements containing the normalised bin values of both polarisation angles, where each polarisation angle (set of 8 bins) is normalised separately. The asymmetric sources are symmetrised based on the variances:

$$\Sigma_{\text{nominal}} = \frac{\Sigma^+ + \Sigma^-}{2}, \tag{9.7}$$

where Σ^+ and Σ^- correspond to the up and down covariance matrices, respectively. The suffix nominal indicates here that this corresponds to the symmetrisation used in the matrix model. Symmetrising the variances of the asymmetric sources in the hybrid model will not preserve the same level of correlations between the bins. Therefore, an equivalent symmetrisation is explored starting with symmetrising the response based on the variations:

$$\Delta_{\text{sym}} = \frac{\Delta^+ - \Delta^-}{2}. \tag{9.8}$$

It should be noted that in general Δ^+ and Δ^- have opposite signs and for that reason there is a minus sign in the symmetrisation[1]. With this symmetrised response function, an alternative covariance matrix can be constructed:

$$\Sigma_{\text{sym}} = \Delta_{\text{sym}} \cdot \Delta^T_{\text{sym}}. \tag{9.9}$$

Actually, one can show that the same nominal covariance matrix, shown in equation 9.7, is obtained when adding the asymmetric part (the difference between the up and down variations) to the symmetric part defined above:

---

[1] If both variations have the same sign, they end up on the same side with respect to the nominal distribution and their response is highly asymmetric.

$$
\begin{aligned}
\Delta_{\text{asym}} &= \frac{\Delta^{+} + \Delta^{-}}{2}, \\
\Sigma_{\text{asym}} &= \Delta_{\text{asym}} \cdot \Delta^{T}_{\text{asym}}, \\
\Sigma_{\text{nominal}} &= \Sigma_{\text{sym}} + \Sigma_{\text{asym}}.
\end{aligned}
\tag{9.10}
$$

For the purpose of comparison, these can be regarded as two independent systematic sources, each with its own nuisance parameter. To be specific, the hybrid model that is internally consistent with the matrix model is defined as follows: each systematic uncertainty source obtains two distinct (uncorrelated) nuisance parameters, one that has the symmetric response (Δ_{sym}), the other that has the asymmetric[2] response (Δ_{asym}).

9.1.3 Decorrelating the modelling systematic

From a fit using the hybrid model on Asimov test data, not shown in this work, it was seen that the theoretical uncertainty source *GEN_TCHAN_AFII_GEN*, related to the generator choice for the t-channel signal process, has a large contribution to the total uncertainty for both Wilson coefficients while its nuisance parameter gets somewhat constrained. Since the estimation of this modelling uncertainty comes from the comparison of two different Monte Carlo simulations, it is actually a multi dimensional uncertainty. In other words, the variation of one nuisance parameter may not represent the exact shape that simultaneously acts on $\cos\theta_x$ and $\cos\theta_y$. For this reason this paragraph studies the impact on the result when splitting this source into separate (decorrelated) effects in the $\cos\theta_x$ and $\cos\theta_y$ distributions.

Table 9.1 summarises the effect when decorrelating *GEN_TCHAN_AFII_GEN* between $\cos\theta_x$ and $\cos\theta_y$. It can be observed that the constraint gets somewhat reduced in the decorrelated setup, which causes the uncertainty on the Wilson coefficients to increase slightly.

Setup	Constraint *GEN_TCHAN_AFII_GEN*	Uncertainty on C_{tW}	 C_{itW}
Normal	± 0.55	± 0.49	± 0.24
Decorrelated	$X : \pm 0.60$ $Y : \pm 0.69$	± 0.50	± 0.25

Table 9.1: Effect when decorrelating $\cos\theta_x$ *and* $\cos\theta_y$ *for GEN_TCHAN_AFII_GEN.*

The uncertainties on the POIs are slightly larger in the decorrelated setup. The conservative choice is made and the decorrelated setup is used. Note that this has also been done in the matrix model presented in the previous chapter.

9.1.4 The probability density function P_{sys} and the full likelihood

The systematic uncertainties are assumed to be Gaussian and therefore each θ nuisance parameter is constrained with a Gaussian pdf centred at zero with unit width:

$$
P_{\text{sys}} = \prod_{s}^{\text{systematics}} \frac{1}{\sqrt{2\pi}} \exp\left\{-\frac{\theta_s^2}{2}\right\}. \tag{9.11}
$$

The uncertainty sources that are not described by a nuisance parameter, such as the statistical and the PDF uncertainties, remain part of the covariance matrix. As was the case in the matrix model setup, this covariance matrix is also of rank 14 and therefore again a transformation to the eigenvector representation is applied as presented in equation 8.3. The pdf describing the uncertainty related to the morphing (P_{morphing}) is the same in both models and is given in equation 8.8.

---

[2] Note that both Δ_{sym} and Δ_{asym} are in fact symmetric, see equations 9.8 and 9.10. The term asymmetric here refers to the original difference between the up and the down variations, which would be zero for 100% symmetric uncertainty sources.

This concludes all the ingredients for the likelihood of the hybrid model given in equation 9.1. For completeness the full likelihood is given in equation 9.12, where the separate components are indicated. In the following section this procedure is validated by comparing it to the matrix model setup.

$$\mathrm{LH}_{\mathrm{hybrid}} \propto \underbrace{\exp\left\{-\frac{1}{2}\left(\vec{\mu}'\right)^{T}\left(D'\right)^{-1}\left(\vec{\mu}'\right)\right\}}_{P_{\text{hybrid model}}} \cdot \underbrace{\overset{\text{templates}}{\prod_{t}} \exp\left\{-\frac{1}{2}\left(\vec{\alpha}_{0t}-\vec{\alpha}_{t}\right)^{T}\left(\Sigma_{t}^{\prime\mathrm{MC}}\right)^{-1}\left(\vec{\alpha}_{0t}-\vec{\alpha}_{t}\right)\right\}}_{P_{\text{morphing}}} \cdot \underbrace{\overset{\text{systematics}}{\prod_{s}} \exp\left\{-\frac{\theta_{s}^{2}}{2}\right\}}_{P_{\text{sys}}} \tag{9.12}$$

9.2 Validation

In order to validate the implementation of the hybrid model, the fits to MC validation samples are compared with those done with the matrix model. Similar results are expected between both models since constraints and pulls on uncertainty sources in a covariance matrix happen implicitly [111]. The same four different benchmark samples are studied, as was done in the closure test of the previous chapter, each generated with a different set of coupling values given in table 3.2.

The values for C_{tW} and C_{itW} are given in figures 9.1 and 9.2, respectively. Each entry in the figure presents the results of both models when fitted to that particular MC dataset indicated on the y-axis. As an example for the notation used on the y-axis, the top entry corresponds to the validation sample generated with $C_{itW} = -1.75$ and $C_{tW} = 2$. It can be observed that both models are in good agreement with each other, concluding that the hybrid model can be used to estimate the effects from individual systematic uncertainty sources.

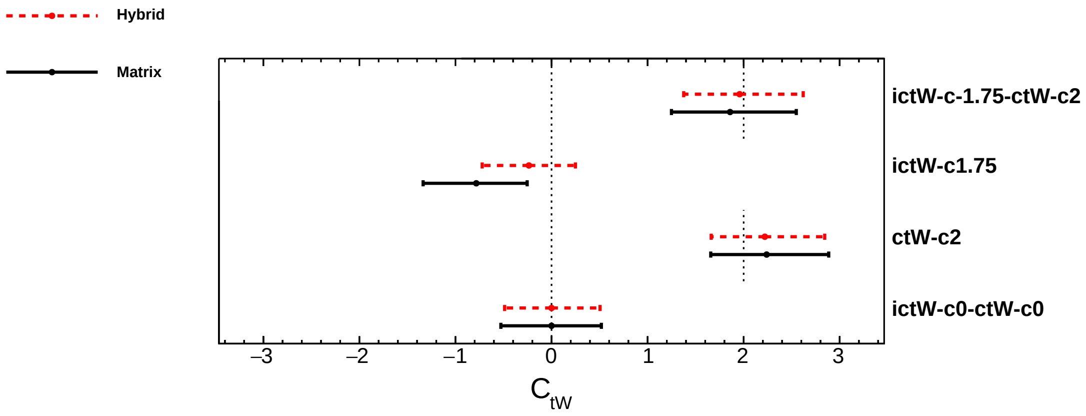

Figure 9.1: Comparison of MC validation fit results of C_{tW} from both fit models. As indicated, the red dashed (black solid) bars represent the hybrid (matrix) model.

9.3 Effects from systematic uncertainties

Now that the hybrid model is defined and validated, it can be exploited to gain insight on the effects from individual systematic uncertainties. This will be done in this section, where the hybrid model is fitted to the unfolded data measured with the ATLAS detector in the years 2015 to 2018. The nuisance parameters that correspond to the asymmetric part of the response function (Δ_{asym}) are indicated with "Asym" at the end of their name and the decorrelated modelling uncertainty (*GEN_TCHAN_AFII_GEN*) either has an "X" or "Y" at the end of its name to refer to either $\cos\theta_x$ or $\cos\theta_y$.

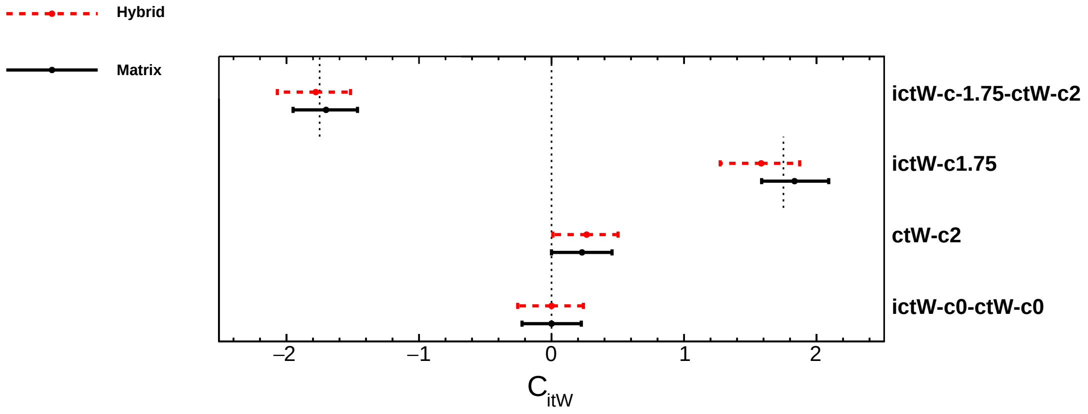

Figure 9.2: Comparison of MC validation fit results of C_{itW} from both fit models. As indicated, the red dashed (black solid) bars represent the hybrid (matrix) model.

The effect that nuisance parameters have on the fit result can be seen in the ranking shown in figure 9.3. Here the change on the obtained value for both Wilson coefficients are given on the top axis when the nuisance parameter in question is fixed to the value corresponding to its up (blue) or down (cyan) variation. The empty bar belongs to the pre-fit range and the filled to the post-fit range. Additionally the pulls and constraints on the fitted nuisance parameters from the best-fit are shown by the black dots and lines that are associated with the bottom axis.

The ranking is based on the effect from the pre-fit range (empty bar). High ranked nuisance parameters are usually stronger correlated with the POI than lower ranked parameters. Differences between the empty and the filled bar are directly related to the constraint and pull of that nuisance parameter.

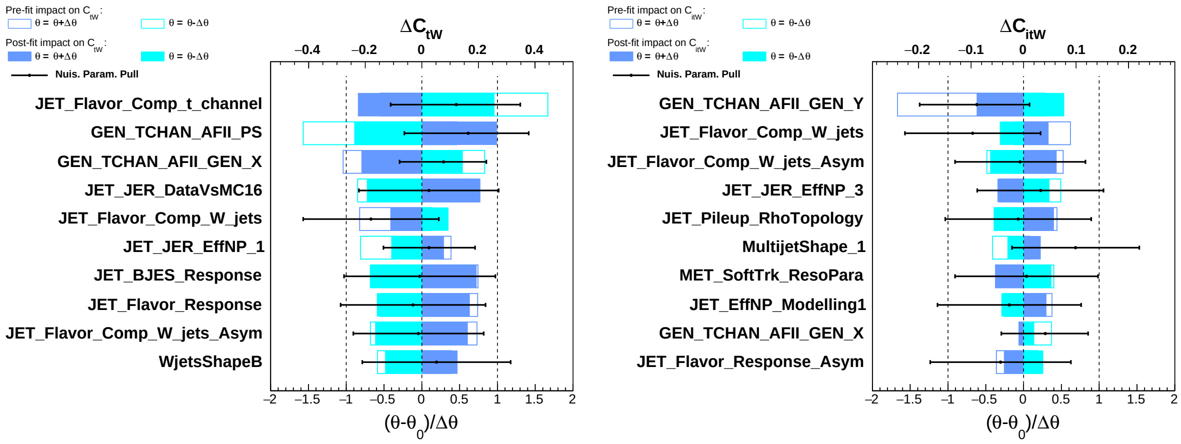

Figure 9.3: Nuisance parameter ranking study for the hybrid model with two nuisance parameters per asymmetric uncertainty source. The change on the value is shown on the top axis for C_{tW} (left) and C_{itW} (right) when one source of uncertainty is fixed to its up (blue) and down (cyan) variations. The empty bar corresponds to the pre-fit range and the full bar to the post-fit range. The pull and constraint is additionally shown via the black line and corresponds to the bottom axis.

It can be observed that the uncertainties related to measuring jets (sources with *JET*) are important. This is not surprising as jets are difficult to measure experimentally and are essential in this analysis as they are used to reconstruct the top quark and its spin axis. Additionally the modelling of the signal sample (sources with *GEN_TCHAN*) is important, where, as expected, the parameter of *GEN_TCHAN_AFII_GEN* related to $\cos\theta_y$ ranks high for C_{itW}, whereas the part related to $\cos\theta_x$ ranks high for C_{tW}.

Another thing to notice is that the asymmetric part of *JET_Flavor_Comp_W_jets*, which accounts for the flavour related uncertainty on the jet energy scale (JES) of the W+jets background, ranks high for both C_{tW} and C_{itW}. This indicates that this measurement is sensitive to the asymmetry between the up and the down variations and suggests that symmetrisation of this uncertainty can hide an important effect. The statistical uncertainties on these variations are large and therefore symmetrisation is adopted in the default setup.

9.3.1 Conclusion

The hybrid model gives similar results as the matrix model when asymmetric systematic uncertainties are treated consistently. This alternative model has been exploited in this chapter to obtain additional insight on the effects from individual uncertainty sources. From Asimov results, not shown in this work, it was observed that the systematic uncertainty related to modelling the hard process of the signal sample (*GEN_TCHAN_AFII_GEN*) ranks high and is constrained by the data. The nuisance parameter of this modelling uncertainty may not represent the exact shape that simultaneously acts on both polarisation angles, which may lead underestimating its uncertainty. Therefore, the constraint is slightly reduced by decorrelating its effect between the $\cos\theta_x$ and $\cos\theta_y$ distributions. The hybrid model was then fitted to the unfolded data which showed that the largest contributions to the final uncertainty on the coefficients come from measuring jets and modelling the signal process.

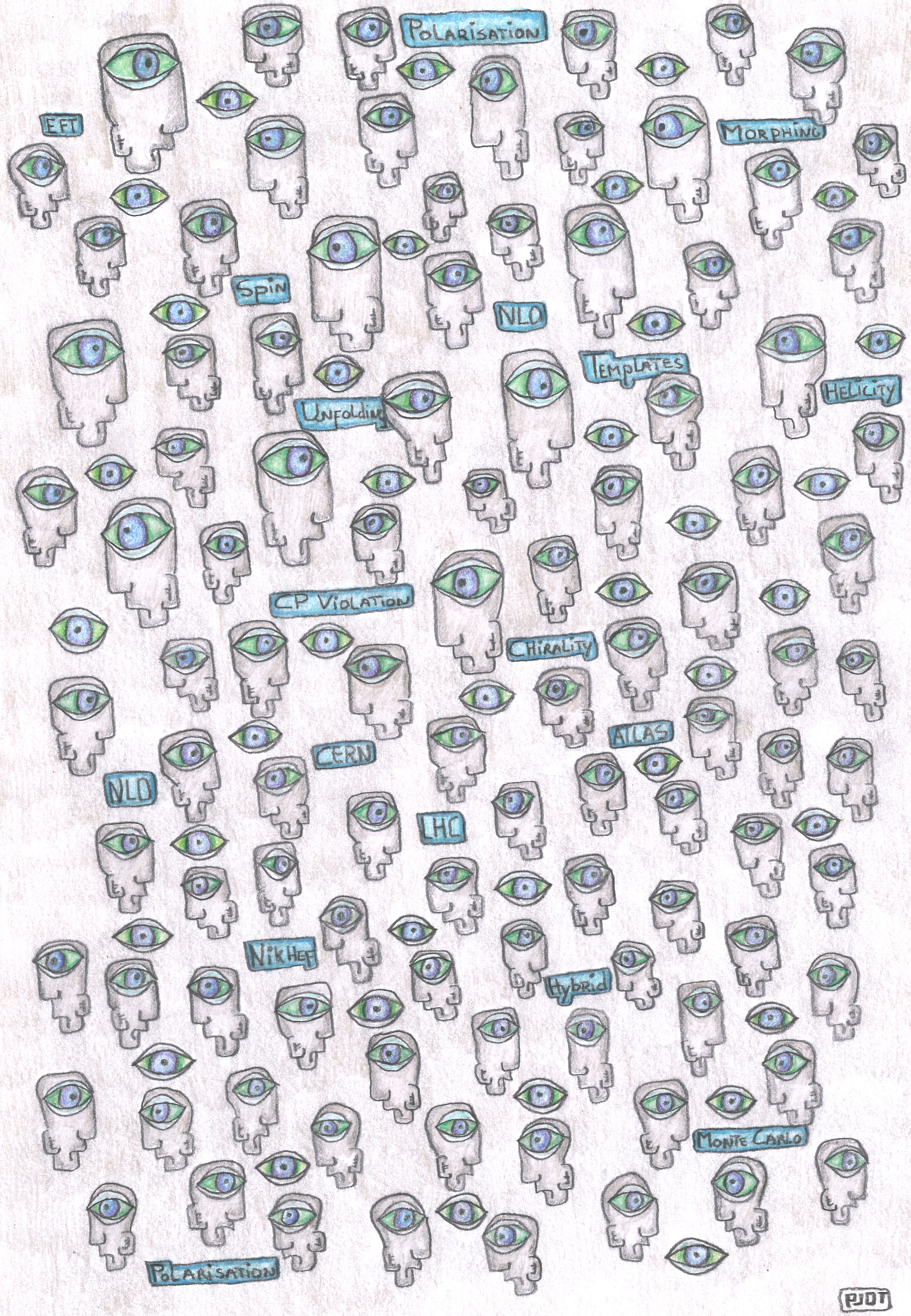
POLARISATION
EFT
MORPHING
SPIN
NLO
TEMPLATES
HELICITY
Unfolding
CP VIOLATION
CHIRALITY
ATLAS
CERN
NLO
LHC
NikHef
Hybrid
MONTE CARLO
POLARISATION
PJDT

Chapter 10

Discussion

The objective of this thesis was to study possible effects from new physics that lead to CP violation in the Wtb vertex. The work has been divided into three main parts. Part I contained the phenomenological study on how Effective Field Theory (EFT) affects the single top quark process. It discussed the important theoretical aspects and presented the most sensitive distributions for measuring deviations from the SM based on Monte Carlo (MC) simulations. In part II the experimental analysis on measuring these distributions with the ATLAS detector was provided. The technique of unfolding was employed to remove effects caused by the detector material, making it possible to compare the measured results directly to simulations. Finally in part III the measured results were interpreted in terms of EFT operators, where a morphing technique was exploited for the parametric description of the signal. In this chapter the conclusions from each part are collected, together with the assumptions that went into the work. Additionally, suggestions for possible improvements for future analyses are provided.

10.1 Phenomenological study

In part I a phenomenological study, based on MC simulations, has been performed on the single top t-channel process in the context of EFT. In the EFT formalism the SM Lagrangian is augmented by including an expansion in orders of $1/\Lambda$ with corresponding higher dimensional operators and their coefficients C_i. The scale Λ is where new physics effects effectively start to contribute and is set to 1 TeV in this work. The following three dimension-6 operators have been studied that contribute at leading order in QCD and at $O(1/\Lambda^2)$ in the t-channel process: O_{tW}, $O_{\varphi Q}$ and O_{qQ}.

For the first time the effects from these dimension-6 operators on the single top production and decay have been computed at NLO in QCD. It was found that NLO effects affect both the total rates and the differential distributions in a non-trivial way. Differences between the K-factor distribution, which is defined as the ratio NLO over LO, between the SM and EFT operators were seen to be on the order of 10% for the rates and the shapes. It can therefore be concluded that NLO effects are needed to reliably predict the impact of the dimension-6 operators.

The expression for a differential cross section in the presence of dimension-6 operators becomes:

$$d\sigma = d\sigma_{\mathrm{SM}} + \sum_i \frac{C_i}{\Lambda^2} 2\mathrm{Re}\left(d\sigma^*_{\mathrm{SM}}\, d\sigma_i\right) + \sum_{i\leq j} \frac{C_i C_j}{\Lambda^4} |d\sigma|^2_{i,j}, \tag{10.1}$$

where the terms C_i/Λ^2 and C_iC_j/Λ^4 are referred to as the linear and squared terms, respectively. In order to fully exploit the power of spin correlations, a series of angular observables were explored that can be used to probe new physics couplings in either the production or decay of the top quark. These include the so-called polarisation angles and W helicity fractions. These angular distributions are found to be sensitive to different operators. Most notably, the polarisation angles $\cos\theta_x$ and $\cos\theta_y$ are sensitive to the linear terms of the real (C_{tW}) and imaginary (C_{itW}) part of the O_{tW} operator, respectively. The parameter C_{itW} is of particular interest as a non-zero value flags CP violation in the Wtb vertex.

The work presented in part I is an example of using an accurate and realistic simulation framework to compute deviations from the SM within SMEFT for a limited number of operators. As mentioned, the work has been done with NLO precision in QCD. This is already an improvement since most EFT interpretations do not go beyond LO. An obvious next step would be to verify that the effects on the dimension-6 operators when going to NNLO are small enough to ignore. Furthermore, only the dimension-6 operators have been studied that contribute at leading order in QCD and at $O(1/\Lambda^2)$ in the t-channel process. Even in this limited set the interference between the 4 fermion operator (O_{qQ}) and the imaginary part of O_{tW} has not been studied since no such model at NLO was available at the time. Even though the contributions from other operators, not included in this study, are expected to be less dominant, in further analyses (with higher precision) the expansion of the EFT scope might become necessary. For instance the left-handed operators O_{bW} and $O_{\phi\phi}$, which linear terms are suppressed by the b-quark mass, or the top-gluon operator O_{tG} that contributes at NLO in QCD. Perhaps even including operators beyond the top sector that can contribute to the decay of the W boson (or to the irreducible backgrounds).

The effects of the squared terms (C_iC_j/Λ^4) of the dimension-6 operators have been included this study. The terms with order $1/\Lambda^4$ are however not complete as no dimension-8 operators were taken into account. When designing an EFT interpretation there is always the trade off between computation time and feasibility on the one side, and inclusiveness on the other. Over time the limits on Wilson coefficients will become tighter, while the uncertainty on the measurements decrease, meaning that the assessment of which effective operators to include has to be done separately for each new analysis.

10.2 Unfolding analysis

Part II presented the latest measurement of the top quark's polarisation angles $\cos\theta_x$ and $\cos\theta_y$ obtained in the single top t-channel process from a dataset of 139 fb^{-1} recorded with the ATLAS detector in the years 2015 until 2018. The measured polarisation angles were unfolded, removing detector effects, to be able to compare the results directly to MC simulations. The process of unfolding corrects for the effects caused by the propagation from "particle level" (MC simulation) to "reco level" (after detector smearing and reconstruction). For the unfolding process a large MC sample is required and hence this procedure depends on the choice of the MC generator and the accuracy of the detector simulation. Furthermore, the MC generator uses SM settings and therefore tests are performed to verify that the unfolding procedure is robust against contributions from the EFT. For this work the results of these tests showed that possible effects are smaller than the current sensitivity, however a future analysis with even higher precision may be affected.

The final distributions were normalised and a covariance matrix was built that contains all the bin-to-bin uncertainties and correlations. A good agreement between the data and the prediction was observed and the most dominant uncertainty sources are the jet energy resolution (JER) and the modelling of the t-channel signal sample. The total uncertainty on the normalised and unfolded bins in the distributions of $\cos\theta_x$ and $\cos\theta_y$ range from about 5% to 20%. With this precision it can be observed that there is indeed sensitivity to the real and imaginary part of the O_{tW} operator.

The dominant uncertainties include both experimental (JER) and theoretical (modelling) uncertainty sources. An improvement in either area could therefore reduce the total uncertainty for the next measurement. The uncertainty related to the modelling is estimated by taking the difference between two MC generators. This means that the size of this uncertainty depends on the choice for the alternative MC generator. In addition, there are many differences in how the available generators implement their calculations. It is doubtful that this estimate therefore exactly describes the shape variation of the distributions. For analyses where the modelling has a dominant contribution to the total uncertainty, such as this one, it might be beneficial to have the theory community reassess what might be a better way to estimate this uncertainty.

The effect from systematic uncertainties on this measurement are estimated using MC samples of limited size. This is understandable since technical resources are valuable, but as a consequence large statistical fluctuations can be present in the obtained systematic effects. These are often reduced using ad hoc techniques such as "symmetrisation", averaging the up and down variations, "smoothing", averaging bins that are next to each other, or even both. In the default setup of this work the contribution from all double sided systematic uncertainties have been symmetrised.

10.3 EFT interpretation

In part III the unfolded and normalised distributions of $\cos\theta_x$ and $\cos\theta_y$ are used to extract the real and imaginary part of the dimension-6 operator O_{tW}. The data was confronted with this operator in a likelihood fit which requires a theoretical prediction in a parametric form. For this purpose, a morphing technique was employed to describe the angular distributions as a function of C_{tW} and C_{itW}. This technique interpolates from a set of MC templates that have been generated on a grid of fixed values for the coefficients. The grid has been obtained through an optimisation procedure and the resulting morphing setup produces predictions that agree well with MC validation samples. The uncertainty related to the morphing are of the order of a few percent and is the smallest near the SM.

The contribution of O_{tW} is included in the production and decay of single top quarks, leading to 15 independent terms in the full expression of a differential cross section:

$$\begin{aligned} d\sigma(C_{tW}, C_{itW}) = &\left| d\sigma_{\text{SM}} + \frac{C_{tW}}{\Lambda^2} \cdot d\sigma_{tW} + \frac{C_{itW}}{\Lambda^2} \cdot d\sigma_{itW} \right|^2_{\text{production}} \\ &\cdot \left| d\sigma_{\text{SM}} + \frac{C_{tW}}{\Lambda^2} \cdot d\sigma_{tW} + \frac{C_{itW}}{\Lambda^2} \cdot d\sigma_{itW} \right|^2_{\text{decay}} . \end{aligned} \tag{10.2}$$

To predict distributions for any value of the coefficients when including all terms, a morphing setup with 15 templates is required. A search algorithm has been exploited to minimise the maximum relative error on the total cross section in a pre-defined parameter region: $-10 \leq C \leq 10$ for both C_{tW} and C_{itW}. This choice performs well for this study. Nonetheless, in other cases it may be beneficial to not limit the search to a fixed parameter region and include (much) larger values for the coefficients to optimise the sensitivity for terms with a large Λ suppression. Furthermore, certain bins may be of particular interest in the future and consequently something else than the relative error on the total cross section should be minimised.

The search algorithm replaces each template with one that is produced at the point in parameter space that corresponds to the maximum relative error. This method leads to a local minimum and therefore leaves enough room for improved tactics like, for instance, gradient descent. Another option would be to combine multiple morphing setups in order to produce a more uniform uncertainty with respect to the coefficients. In any case, it is expected that the time it takes to maximally optimise the morphing setup is not worthwhile, given the minor decrease in the uncertainty on the final result. This is especially the case when the time can also be spent on increasing the MC statistics of the templates.

In the implementation of the fitting procedure the covariance matrix from the unfolded measurement is first diagonalised and the data is projected onto the eigenvectors with non-zero eigenvalues. Good agreement between the model and the data has been observed and the obtained values in a simultaneous fit of both C_{tW} and C_{itW} to the data are $C_{tW} = 0.4 \pm 0.5$ and $C_{itW} = -0.3 \pm 0.2$ at 68.3% CL, which are in accordance with the SM. The limit for C_{itW} presented in this work is more stringent than the marginalised bounds in Ref. [64] and is the best limit obtained from high-energy experiments. Checks have been done that verify that these results are robust under non-zero values for the coefficients of the following dimension-6 operators: $O_{\varphi Q}$, O_{qQ}, O_{bW}, $O_{\phi\phi}$ and O_{tG}. However, some pulls were observed which hint that for a future study, with improved uncertainties, these operators should be taken into account.

All terms of the EFT expansion have been included in the interpretation of O_{tW}, even though the higher order terms are not complete as the full expansion that involves dimension-8 operators is not yet available. This however allowed to study the impact from these terms by comparing the result when higher orders of Λ are excluded in the fit. As expected, when results turn out to be close to the SM only including the linear terms seem to be sufficient. Even further away from the SM the linear results remain more or less consistent with the other setups. However, if possible, it is better to go one step further and include up to the squared terms. This might mean that future work could profit from including the linear terms from dimension-8 operators. This is the first time that the usual assumption to exclude terms beyond $1/\Lambda^4$ has been validated.

In the last chapter of part III an alternative fit model, called the hybrid model, has been developed to gain more insight into the impact of individual uncertainty sources. In this model, the strength of each systematic uncertainty source is implemented as a nuisance parameter. Other uncertainties, such as the statistical uncertainty, remain in the covariance matrix. Even though both approaches for including uncertainty sources (in a matrix or as a nuisance parameter) yield the exact same results when all uncertainties are treated equivalently, the hybrid setup has more freedom as it allows for asymmetric systematic variations. In this work, the statistical uncertainties on the asymmetric variations was large and therefore the symmetrised matrix setup has been used. When systematic variations are obtained using samples with high statistical precision, a more complete approach would involve the hybrid setup with asymmetric variations.

Appendices

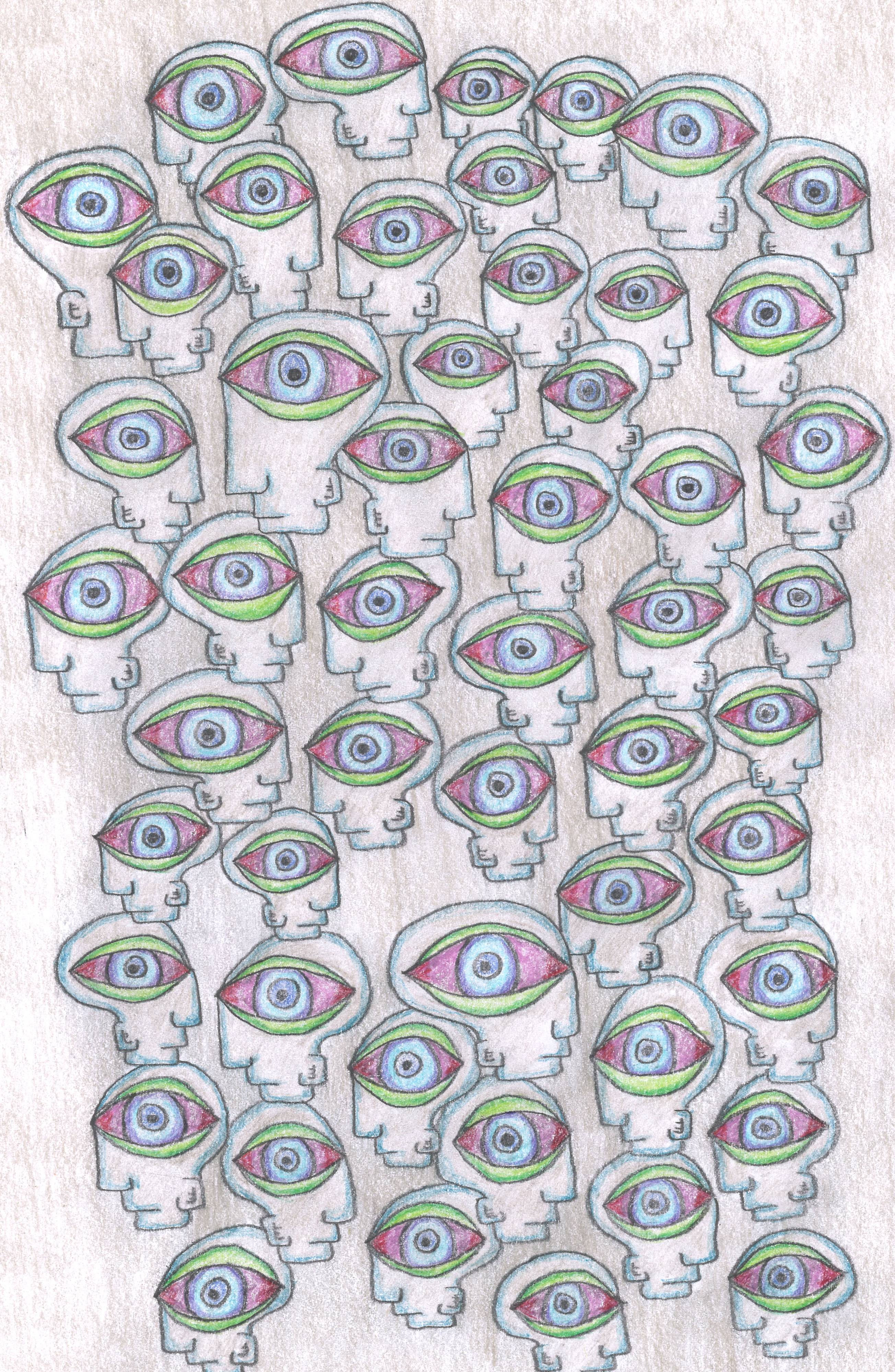

PJOT

Appendix A

Interference study

The morphing method provides the possibility to study if interference terms play a role in the description of an observable. As shown in table 3.1, the interference between the imaginary part of O_{tW} and the SM has no contribution to the inclusive cross section. However, in the $\cos\theta_y$ distribution there is sensitivity for this effect (figure 3.14). The question to answer is whether this effect is caused by the squared terms, which are suppressed by order $1/\Lambda^4$, or is the interference non-zero for this observable[1]?

To simplify the procedure of investigating the contribution of the interference in $\cos\theta_y$, a LO morphing setup is used focusing only on C_{itW} which contributes to the production and decay of the top quark. The expression for this cross section becomes:

$$\begin{aligned}\sigma(C_{itW}) = \left| O_{\text{SM}} + \frac{C_{itW}}{\Lambda^2} \cdot O_{itW} \right|^2_{\text{production}} \cdot \left| O_{\text{SM}} + \frac{C_{itW}}{\Lambda^2} \cdot O_{itW} \right|^2_{\text{decay}} = \\ \tilde{O}_1 + C^1_{itW} \cdot \tilde{O}_2 + C^2_{itW} \cdot \tilde{O}_3 + C^3_{itW} \cdot \tilde{O}_4 + C^4_{itW} \cdot \tilde{O}_5,\end{aligned} \tag{A.1}$$

where $C_{\text{SM}} = 1$ and all orders of the EFT expansion (Λ), together with the numerical factors originating from the squaring, are absorbed in the $\tilde{O}$ terms. The odd factors of C_{itW} correspond to the interference terms under study. Thus, five templates are required to describe the case with interference whereas only three are needed when no interference is included. The templates for both setups are presented in table A.1 and figure A.1 shows both morphing predictions for $\cos\theta_y$ compared to a validation sample.

Template	C_{itW}
1	-10
2	-2.93
3	0
4	5.56
5	10

Template	C_{itW}
1	-10
2	0
3	5.56

Table A.1: The templates for the morphing setup with (left) and without (right) interference.

It can be seen that for the setup without interference (right) the morphing prediction deviates significantly. The requirement for including the interference becomes even more apparent when a validation sample with a higher value and opposite sign for C_{itW} is taken, as seen in figure A.2. This indicates that for the $\cos\theta_y$ observable, which has sensitivity for C_{itW}, interference terms cannot be neglected and are therefore taken into account in the rest of the work presented in this thesis.

---

[1] Actually, based on the fact that the distributions of $\cos\theta_y$ go in opposite direction with respect to the SM when considering values for C_{itW} with opposite signs, as can be seen in figure 3.15, it is known that interference terms are important.

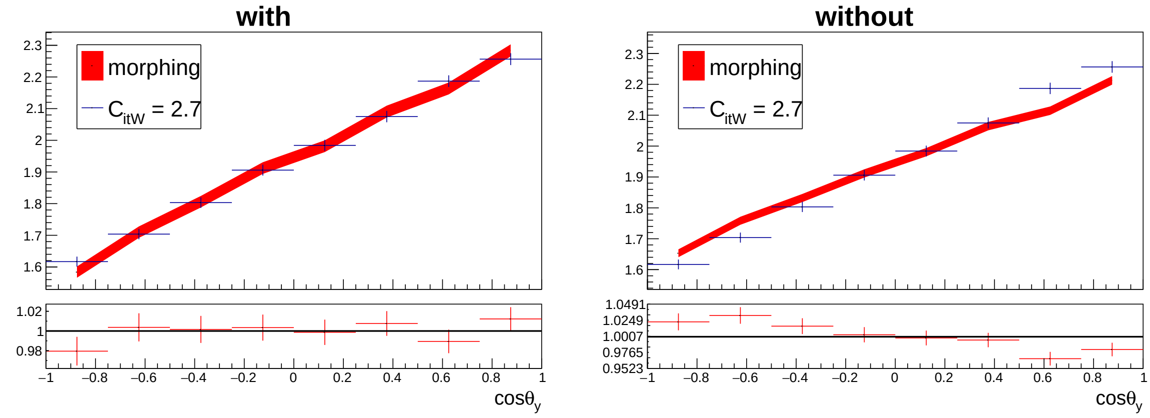

Figure A.1: Validation of the morphing prediction for a setup with (left) and without (right) interference terms. The red band shows is the morphing prediction with its error, the blue points belong to a generated validation sample where $C_{itW} = 2.7$

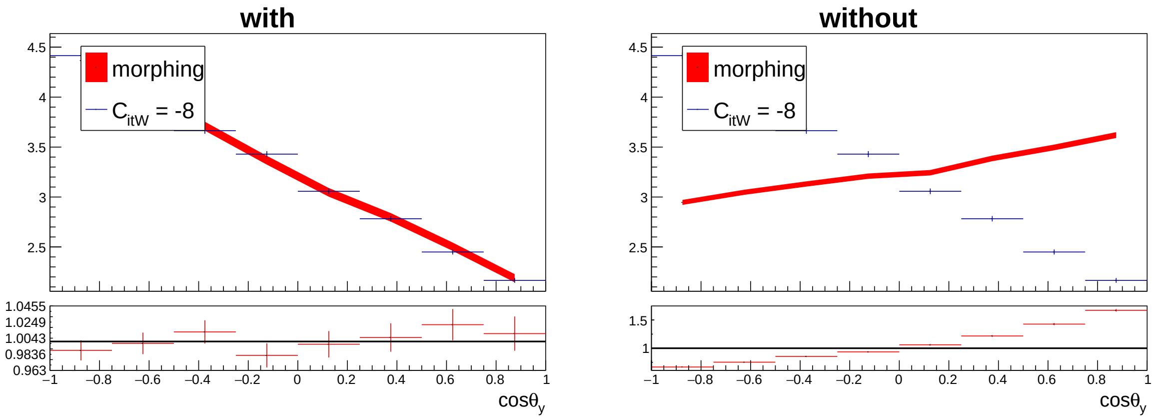

Figure A.2: Validation of the morphing prediction for a setup with (left) and without (right) interference terms. The red band shows is the morphing prediction with its error, the blue points belong to a generated validation sample where $C_{itW} = -8$

Appendix B

Validation of the morphing optimisation procedure

The optimisation approach, discussed in section 7.3, makes use of two assumptions in order to speed up the process: morphed predictions are employed as new templates and the initial set of templates have been generated with LO precision. This appendix justifies both these assumptions in separate sections.

B.1 Morphed template

To verify that a ”morphed template” can be exploited in the optimisation routine, figure B.1 compares two different setups. On the left all templates are genuine MC samples, where on the right one of the templates (SM) has been replaced by a morphed template.

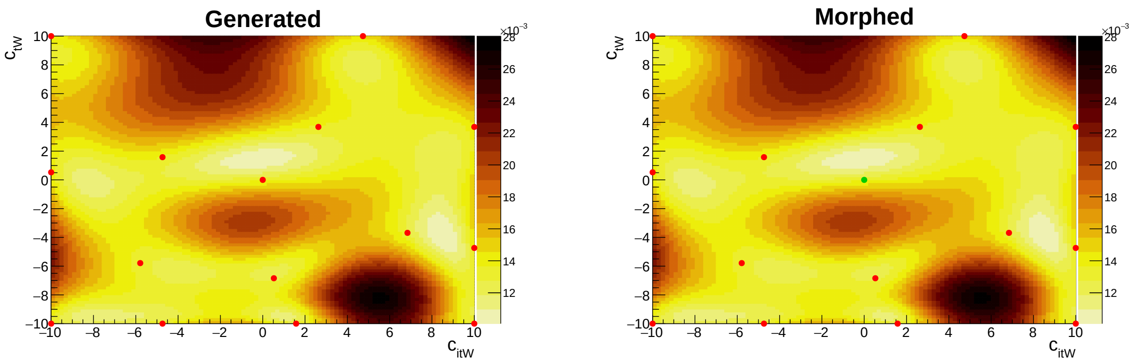

Figure B.1: Relative morphing uncertainty with a setup containing genuine MC templates (left) and where one has been replaced by a morphed template (right). The red dots correspond to the generated templates, whereas the green dot shows a template created by the morphing procedure.

It can be observed that indeed the morphed template (green dot) mimics the behavior of a template satisfactory. It should be mentioned that this only works when the uncertainty on the morphed template is changed such that it resembles the MC statistical error of the template it replaces.

B.2 LO versus NLO

To check that LO templates represent the NLO behavior sufficiently, figure B.2 compares their uncertainty profiles. On the left a morphing setup with LO templates without any additional selection cuts after the generation is shown. On the right the exact same setup is used, only here the templates have been generated with NLO precision in QCD and additional selection criteria are applied that lead to the Signal Region defined in section 5.3. In order to only compare the pattern of the contours, both figures have been normalised.

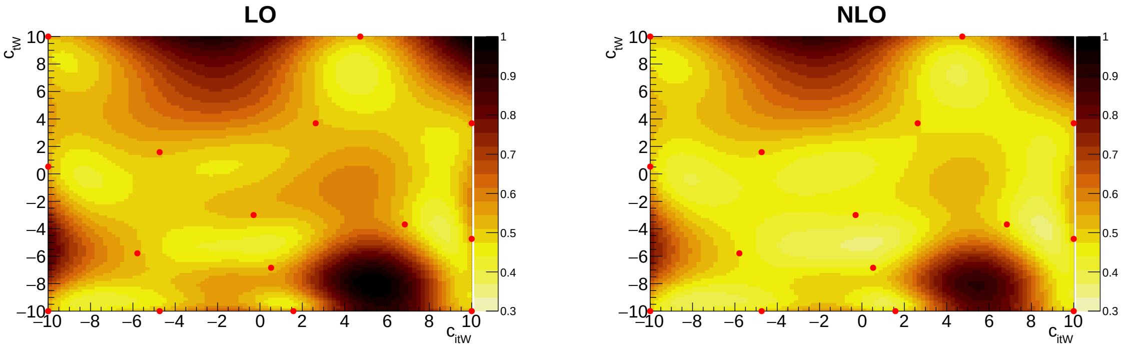

Figure B.2: Normalised relative morphing uncertainty for LO (left) and NLO in the SR (right). The red dots correspond to the templates for the morphing.

The contours exhibit a similar pattern and it can be concluded that LO templates without any additional selection criteria can safely be used in the optimisation routine, to simplify the procedure.

Bibliography

[1] M. de Beurs et al. “Effective operators in t-channel single top production and decay”. In: *Eur. Phys. J.* C78.11 (2018), p. 919. DOI: `10.1140/epjc/s10052-018-6399-3`. arXiv: `1807.03576 [hep-ph]`.

[2] Georges Aad et al. “Observation of a new particle in the search for the Standard Model Higgs boson with the ATLAS detector at the LHC”. In: *Phys. Lett. B* 716 (2012), pp. 1–29. DOI: `10.1016/j.physletb.2012.08.020`. arXiv: `1207.7214 [hep-ex]`.

[3] E. Drexler. *Summary of interactions between particles described by the Standard Model.* URL: `https://en.wikipedia.org/wiki/Standard_Model#/media/File:Elementary_particle_interactions_in_the_Standard_Model.png`.

[4] P.A.R. Ade et al. “Planck 2013 results. I. Overview of products and scientific results”. In: *Astron. Astrophys.* 571 (2014), A1. DOI: `10.1051/0004-6361/201321529`. arXiv: `1303.5062 [astro-ph.CO]`.

[5] D. Griffiths. *Introduction to Elementary Particles*. Physics textbook. Wiley, 2008. ISBN: 9783527406012. URL: `https://books.google.nl/books?id=w9Dz56myXm8C`.

[6] M. Thomson. *Modern Particle Physics*. Modern Particle Physics. Cambridge University Press, 2013. ISBN: 9781107034266. URL: `https://books.google.nl/books?id=BV1sAAAAQBAJ`.

[7] F. Halzen and A.D. Martin. *Quarks and leptons: an introductory course in modern particle physics*. Wiley, 1984. URL: `https://books.google.de/books?id=zwDvAAAAMAAJ`.

[8] Donald Hill Perkins. *Introduction to high energy physics; 4th ed.* Cambridge: Cambridge Univ. Press, 2000. DOI: `10.1017/CBO9780511809040`. URL: `https://cds.cern.ch/record/396126`.

[9] Nicola Cabibbo. “Unitary Symmetry and Leptonic Decays”. In: *Phys. Rev. Lett.* 10 (12 June 1963), pp. 531–533. DOI: `10.1103/PhysRevLett.10.531`. URL: `https://link.aps.org/doi/10.1103/PhysRevLett.10.531`.

[10] Makoto Kobayashi and Toshihide Maskawa. “CP-Violation in the Renormalizable Theory of Weak Interaction”. In: *Progress of Theoretical Physics* 49.2 (Feb. 1973), pp. 652–657. ISSN: 0033-068X. DOI: `10.1143/PTP.49.652`. eprint: `https://academic.oup.com/ptp/article-pdf/49/2/652/5257692/49-2-652.pdf`.

[11] B. Pontecorvo. “Inverse beta processes and nonconservation of lepton charge”. In: *Sov. Phys. JETP* 7 (1958), pp. 172–173.

[12] Ziro Maki, Masami Nakagawa, and Shoichi Sakata. “Remarks on the Unified Model of Elementary Particles”. In: *Progress of Theoretical Physics* 28.5 (Nov. 1962), pp. 870–880. ISSN: 0033-068X. DOI: `10.1143/PTP.28.870`. eprint: `https://academic.oup.com/ptp/article-pdf/28/5/870/5258750/28-5-870.pdf`. URL: `https://doi.org/10.1143/PTP.28.870`.

[13] Ikaros I.Y. Bigi and A.I. Sanda. “Notes on the Observability of CP Violations in B Decays”. In: *Nucl. Phys. B* 193 (1981), pp. 85–108. DOI: `10.1016/0550-3213(81)90519-8`.

[14] J. H. Christenson et al. “Evidence for the 2π Decay of the K_2^0 Meson”. In: *Phys. Rev. Lett.* 13 (4 July 1964), pp. 138–140. DOI: `10.1103/PhysRevLett.13.138`. URL: `https://link.aps.org/doi/10.1103/PhysRevLett.13.138`.

[15] A. Apostolakis et al. “A Determination of the CP violation parameter eta+- from the decay of strangeness tagged neutral kaons”. In: *Phys. Lett. B* 458 (1999), pp. 545–552. DOI: `10.1016/S0370-2693(99)00596-1`.

[16] Sébastien Descotes-Genon and Patrick Koppenburg. “The CKM Parameters”. In: *Ann. Rev. Nucl. Part. Sci.* 67 (2017), pp. 97–127. DOI: `10.1146/annurev-nucl-101916-123109`. arXiv: `1702.08834 [hep-ex]`.

[17] C. Jarlskog. “Commutator of the Quark Mass Matrices in the Standard Electroweak Model and a Measure of Maximal CP Nonconservation”. In: *Phys. Rev. Lett.* 55 (10 Sept. 1985), pp. 1039–1042. DOI: `10.1103/PhysRevLett.55.1039`. URL: `https://link.aps.org/doi/10.1103/PhysRevLett.55.1039`.

[18] Wei-Shu Hou. “Source of CP Violation for the Baryon Asymmetry of the Universe”. In: *Chin. J. Phys.* 47 (2009), p. 134. arXiv: `0803.1234 [hep-ph]`.

[19] F. Abe et al. “Observation of top quark production in anti-p p collisions”. In: *Phys. Rev. Lett.* 74 (1995), pp. 2626–2631. eprint: `hep-ex/9503002`.

[20] S. Abachi et al. “Observation of the top quark”. In: *Phys. Rev. Lett.* 74 (1995), pp. 2632–2637. eprint: `hep-ex/9503003`.

[21] I. Bigi et al. “Production and decay properties of ultra-heavy quarks”. In: *Physics Letters B* 181.1 (1986), pp. 157–163. ISSN: 0370-2693. DOI: `https://doi.org/10.1016/0370-2693(86)91275-X`. URL: `http://www.sciencedirect.com/science/article/pii/037026938691275X`.

[22] Gregory Mahlon and Stephen J. Parke. “Improved spin basis for angular correlation studies in single top quark production at the Tevatron”. In: *Phys. Rev.* D55 (1997), pp. 7249–7254. DOI: `10.1103/PhysRevD.55.7249`. arXiv: `hep-ph/9611367 [hep-ph]`.

[23] J. A. Aguilar-Saavedra et al. “Probing anomalous Wtb couplings in top pair decays”. In: *Eur. Phys. J.* C50 (2007), pp. 519–533. DOI: `10.1140/epjc/s10052-007-0289-4`. arXiv: `hep-ph/0605190 [hep-ph]`.

[24] J. A. Aguilar-Saavedra and J. Bernabeu. “W polarisation beyond helicity fractions in top quark decays”. In: *Nucl. Phys.* B840 (2010), pp. 349–378. DOI: `10.1016/j.nuclphysb.2010.07.012`. arXiv: `1005.5382 [hep-ph]`.

[25] Gregory Mahlon and Stephen J. Parke. “Single top quark production at the LHC: Understanding spin”. In: *Phys. Lett.* B476 (2000), pp. 323–330. DOI: `10.1016/S0370-2693(00)00149-0`. arXiv: `hep-ph/9912458 [hep-ph]`.

[26] Gregory Mahlon. “Observing spin correlations in single top production and decay”. In: *thinkshop**2: Top Quark Physics for Run II and Beyond Batavia, Illinois, November 10-12, 2000*. 2000. arXiv: `hep-ph/0011349 [hep-ph]`.

[27] J. A. Aguilar-Saavedra and S. Amor Dos Santos. “New directions for top quark polarization in the t-channel process”. In: *Phys. Rev.* D89.11 (2014), p. 114009. DOI: `10.1103/PhysRevD.89.114009`. arXiv: `1404.1585 [hep-ph]`.

[28] Andrew Kobach. “Baryon Number, Lepton Number, and Operator Dimension in the Standard Model”. In: *Phys. Lett.* B758 (2016), pp. 455–457. DOI: `10.1016/j.physletb.2016.05.050`. arXiv: `1604.05726 [hep-ph]`.

[29] M. Anderson et al. “Search for invisible modes of nucleon decay in water with the SNO+ detector”. In: *Physical Review D* 99.3 (Feb. 2019). ISSN: 2470-0029. DOI: `10.1103/physrevd.99.032008`. URL: `http://dx.doi.org/10.1103/PhysRevD.99.032008`.

[30] A. Gando et al. “Search for Majorana Neutrinos near the Inverted Mass Hierarchy Region with KamLAND-Zen”. In: *Phys. Rev. Lett.* 117.8 (2016). [Addendum: Phys.Rev.Lett. 117, 109903 (2016)], p. 082503. DOI: `10.1103/PhysRevLett.117.082503`. arXiv: `1605.02889 [hep-ex]`.

[31] Brian Henning et al. *2, 84, 30, 993, 560, 15456, 11962, 261485, ...: Higher dimension operators in the SM EFT*. 2015. arXiv: `1512.03433 [hep-ph]`.

[32] Ilaria Brivio et al. “O new physics, where art thou? A global search in the top sector”. In: *Journal of High Energy Physics* 2020.2 (Feb. 2020). ISSN: 1029-8479. DOI: `10.1007/jhep02(2020)131`. URL: `http://dx.doi.org/10.1007/JHEP02(2020)131`.

[33] Cen Zhang. “Single Top Production at Next-to-Leading Order in the Standard Model Effective Field Theory”. In: *Phys. Rev. Lett.* 116.16 (2016), p. 162002. DOI: `10.1103/PhysRevLett.116.162002`. arXiv: `1601.06163 [hep-ph]`.

[34] Gauthier Durieux, Fabio Maltoni, and Cen Zhang. "Global approach to top-quark flavor-changing interactions". In: *Phys. Rev.* D91.7 (2015), p. 074017. DOI: `10.1103/PhysRevD.91.074017`. arXiv: `1412.7166 [hep-ph]`.

[35] J. A. Aguilar-Saavedra, C. Degrande, and S. Khatibi. "Single top polarisation as a window to new physics". In: *Phys. Lett.* B769 (2017), pp. 498–502. DOI: `10.1016/j.physletb.2017.04.023`. arXiv: `1701.05900 [hep-ph]`.

[36] G. D'Ambrosio et al. "Minimal flavor violation: An Effective field theory approach". In: *Nucl. Phys.* B645 (2002), pp. 155–187. DOI: `10.1016/S0550-3213(02)00836-2`. arXiv: `hep-ph/0207036 [hep-ph]`.

[37] M. Sozzi. *Discrete Symmetries and CP Violation: From Experiment to Theory*. Oxford Graduate Texts. OUP Oxford, 2008. ISBN: 9780191537950. URL: `https://books.google.ch/books?id=UYHsn9kvQ14C`.

[38] Andy Buckley et al. "General-purpose event generators for LHC physics". In: *Phys. Rept.* 504 (2011), pp. 145–233. DOI: `10.1016/j.physrep.2011.03.005`. arXiv: `1101.2599 [hep-ph]`.

[39] Stefan Höche. *Introduction to parton-shower event generators*. 2015. arXiv: `1411.4085 [hep-ph]`.

[40] Fred James. "Monte Carlo theory and practice". In: *Reports on Progress in Physics - REP PROGR PHYS* 43 (Sept. 1980), pp. 1145–1189. DOI: `10.1088/0034-4885/43/9/002`. URL: `https://www.researchgate.net/publication/252622717_Monte_Carlo_theory_and_practice`.

[41] Stefan Weinzierl. "Introduction to Monte Carlo methods". In: (2000). arXiv: `hep-ph/0006269 [hep-ph]`.

[42] G P Lepage. *VEGAS - an adaptive multi-dimensional integration program*. Tech. rep. CLNS-447. Ithaca, NY: Cornell Univ. Lab. Nucl. Stud., Mar. 1980. URL: `http://cds.cern.ch/record/123074`.

[43] Peter Skands. "Introduction to QCD". In: *Proceedings, 2nd Asia-Europe-Pacific School of High-Energy Physics (AEPSHEP 2014): Puri, India, November 04–17, 2014*. [,63(2017)]. 2013, pp. 341–420. DOI: `10.1142/9789814525220_0008,10.23730/CYRSP-2017-002.63`. arXiv: `1207.2389 [hep-ph]`.

[44] Geoffrey T. Bodwin. "Factorization of the Drell-Yan Cross-Section in Perturbation Theory". In: *Phys. Rev. D* 31 (1985). [Erratum: Phys.Rev.D 34, 3932 (1986)], p. 2616. DOI: `10.1103/PhysRevD.34.3932`.

[45] John C. Collins, Davison E. Soper, and George F. Sterman. "Factorization for Short Distance Hadron - Hadron Scattering". In: *Nucl. Phys. B* 261 (1985), pp. 104–142. DOI: `10.1016/0550-3213(85)90565-6`.

[46] John C. Collins, Davison E. Soper, and George F. Sterman. "Soft Gluons and Factorization". In: *Nucl. Phys. B* 308 (1988), pp. 833–856. DOI: `10.1016/0550-3213(88)90130-7`.

[47] Yuri L. Dokshitzer. "Calculation of the Structure Functions for Deep Inelastic Scattering and e+ e- Annihilation by Perturbation Theory in Quantum Chromodynamics." In: *Sov. Phys. JETP* 46 (1977), pp. 641–653.

[48] V.N. Gribov and L.N. Lipatov. "Deep inelastic e p scattering in perturbation theory". In: *Sov. J. Nucl. Phys.* 15 (1972), pp. 438–450.

[49] L.N. Lipatov. "The parton model and perturbation theory". In: *Sov. J. Nucl. Phys.* 20 (1975), pp. 94–102.

[50] Guido Altarelli and G. Parisi. "Asymptotic Freedom in Parton Language". In: *Nucl. Phys. B* 126 (1977), pp. 298–318. DOI: `10.1016/0550-3213(77)90384-4`.

[51] Rikkert Frederix, Emanuele Re, and Paolo Torrielli. "Single-top t-channel hadroproduction in the four-flavour scheme with POWHEG and aMC@NLO". In: *JHEP* 09 (2012), p. 130. DOI: `10.1007/JHEP09(2012)130`. arXiv: `1207.5391 [hep-ph]`.

[52] T. Kinoshita. "Mass singularities of Feynman amplitudes". In: *J. Math. Phys.* 3 (1962), pp. 650–677. DOI: `10.1063/1.1724268`.

[53] T. D. Lee and M. Nauenberg. "Degenerate Systems and Mass Singularities". In: *Phys. Rev.* 133 (6B Mar. 1964), B1549–B1562. DOI: `10.1103/PhysRev.133.B1549`. URL: `https://link.aps.org/doi/10.1103/PhysRev.133.B1549`.

[54] Gavin P. Salam. “Towards Jetography”. In: *Eur. Phys. J.* C67 (2010), pp. 637–686. DOI: `10.1140/epjc/s10052-010-1314-6`. arXiv: `0906.1833 [hep-ph]`.

[55] R. K Ellis, W. J. Stirling, and B. R. Webber. *QCD and Collider Physics*. Cambridge Monographs on Particle Physics, Nuclear Physics and Cosmology. Cambridge University Press, 1996. DOI: `10.1017/CBO9780511628788`.

[56] Ansgar Denner and S. Dittmaier. “The Complex-mass scheme for perturbative calculations with unstable particles”. In: *Nucl. Phys. Proc. Suppl.* 160 (2006). [,22(2006)], pp. 22–26. DOI: `10.1016/j.nuclphysbps.2006.09.025`. arXiv: `hep-ph/0605312 [hep-ph]`.

[57] C. F. Uhlemann and N. Kauer. “Narrow-width approximation accuracy”. In: *Nucl. Phys.* B814 (2009), pp. 195–211. DOI: `10.1016/j.nuclphysb.2009.01.022`. arXiv: `0807.4112 [hep-ph]`.

[58] Pierre Artoisenet et al. “Automatic spin-entangled decays of heavy resonances in Monte Carlo simulations”. In: *JHEP* 03 (2013), p. 015. DOI: `10.1007/JHEP03(2013)015`. arXiv: `1212.3460 [hep-ph]`.

[59] Stefano Frixione and Bryan R. Webber. “Matching NLO QCD computations and parton shower simulations”. In: *JHEP* 06 (2002), p. 029. DOI: `10.1088/1126-6708/2002/06/029`. arXiv: `hep-ph/0204244`.

[60] M. Tanabashi et al. “Review of Particle Physics”. In: *Phys. Rev. D* 98 (3 Aug. 2018), p. 030001. DOI: `10.1103/PhysRevD.98.030001`. URL: `https://link.aps.org/doi/10.1103/PhysRevD.98.030001`.

[61] J. Alwall et al. “The automated computation of tree-level and next-to-leading order differential cross sections, and their matching to parton shower simulations”. In: *JHEP* 07 (2014), p. 079. DOI: `10.1007/JHEP07(2014)079`. arXiv: `1405.0301 [hep-ph]`.

[62] Rikkert Frederix et al. “Off-shell single-top production at NLO matched to parton showers”. In: *JHEP* 06 (2016), p. 027. DOI: `10.1007/JHEP06(2016)027`. arXiv: `1603.01178 [hep-ph]`.

[63] Richard D. Ball et al. “Parton distributions for the LHC Run II”. In: *JHEP* 04 (2015), p. 040. DOI: `10.1007/JHEP04(2015)040`. arXiv: `1410.8849 [hep-ph]`.

[64] V. Cirigliano et al. “Constraining the top-Higgs sector of the Standard Model Effective Field Theory”. In: *Phys. Rev.* D94.3 (2016), p. 034031. DOI: `10.1103/PhysRevD.94.034031`. arXiv: `1605.04311 [hep-ph]`.

[65] Morad Aaboud et al. “Measurement of the inclusive cross-sections of single top-quark and top-antiquark t-channel production in pp collisions at $\sqrt{s} = 13$ TeV with the ATLAS detector”. In: *JHEP* 04 (2017), p. 086. DOI: `10.1007/JHEP04(2017)086`. arXiv: `1609.03920 [hep-ex]`.

[66] Albert M Sirunyan et al. “Cross section measurement of t-channel single top quark production in pp collisions at $\sqrt{s} = 13$ TeV”. In: *Phys. Lett.* B772 (2017), pp. 752–776. DOI: `10.1016/j.physletb.2017.07.047`. arXiv: `1610.00678 [hep-ex]`.

[67] Morad Aaboud et al. “Direct top-quark decay width measurement in the $t\bar{t}$ lepton+jets channel at $\sqrt{s}$=8 TeV with the ATLAS experiment”. In: *Eur. Phys. J.* C78.2 (2018), p. 129. DOI: `10.1140/epjc/s10052-018-5595-5`. arXiv: `1709.04207 [hep-ex]`.

[68] CMS Collaboration. *Bounding the top quark width using final states with two charged leptons and two jets at $\sqrt{s}$ = 13 TeV*. Tech. rep. CMS-PAS-TOP-16-019. Geneva: CERN, 2016. URL: `https://cds.cern.ch/record/2218019`.

[69] Pier Paolo Giardino and Cen Zhang. “Probing the top-quark width using the charge identification of b jets”. In: *Phys. Rev.* D96.1 (2017), p. 011901. DOI: `10.1103/PhysRevD.96.011901`. arXiv: `1702.06996 [hep-ph]`.

[70] J. A. Aguilar-Saavedra. “Single top quark production at LHC with anomalous Wtb couplings”. In: *Nucl. Phys.* B804 (2008), pp. 160–192. DOI: `10.1016/j.nuclphysb.2008.06.013`. arXiv: `0803.3810 [hep-ph]`.

[71] Torbjörn Sjöstrand et al. “An Introduction to PYTHIA 8.2”. In: *Comput. Phys. Commun.* 191 (2015), pp. 159–177. DOI: `10.1016/j.cpc.2015.01.024`. arXiv: `1410.3012 [hep-ph]`.

[72] Matteo Cacciari, Gavin P. Salam, and Gregory Soyez. “FastJet User Manual”. In: *Eur. Phys. J.* C72 (2012), p. 1896. DOI: `10.1140/epjc/s10052-012-1896-2`. arXiv: `1111.6097 [hep-ph]`.

[73] Matteo Cacciari, Gavin P. Salam, and Gregory Soyez. "The Anti-k(t) jet clustering algorithm". In: *JHEP* 04 (2008), p. 063. DOI: `10.1088/1126-6708/2008/04/063`. arXiv: `0802.1189 [hep-ph]`.

[74] Cen Zhang and Scott Willenbrock. "Effective-Field-Theory Approach to Top-Quark Production and Decay". In: *Phys. Rev.* D83 (2011), p. 034006. DOI: `10.1103/PhysRevD.83.034006`. arXiv: `1008.3869 [hep-ph]`.

[75] D. Barducci et al. "Interpreting top-quark LHC measurements in the standard-model effective field theory". In: (2018). Ed. by Juan Antonio Aguilar-Saavedra et al. arXiv: `1802.07237 [hep-ph]`.

[76] Oliver Sim Bruning et al. *LHC Design Report*. Geneva: CERN, 2004. URL: `https://cds.cern.ch/record/782076`.

[77] Esma Mobs. "The CERN accelerator complex - 2019. Complexe des accélérateurs du CERN - 2019". In: (July 2019). General Photo. URL: `https://cds.cern.ch/record/2684277`.

[78] G. Aad et al. "The ATLAS Experiment at the CERN Large Hadron Collider". In: *JINST* 3 (2008), S08003. DOI: `10.1088/1748-0221/3/08/S08003`.

[79] A. Airapetian et al. "ATLAS: Detector and physics performance technical design report. Volume 1". In: (1999). URL: `https://cds.cern.ch/record/391176`.

[80] A. Airapetian et al. "ATLAS: Detector and physics performance technical design report. Volume 2". In: (1999). URL: `https://cds.cern.ch/record/391177`.

[81] Joao Pequenao and Paul Schaffner. "An computer generated image representing how ATLAS detects particles". Jan. 2013. URL: `https://cds.cern.ch/record/1505342`.

[82] ATLAS Collaboration. "ATLAS inner detector: Technical design report. Vol. 1". In: (Apr. 1997).

[83] M Capeans et al. *ATLAS Insertable B-Layer Technical Design Report*. Tech. rep. CERN-LHCC-2010-013. ATLAS-TDR-19. Sept. 2010. URL: `https://cds.cern.ch/record/1291633`.

[84] Peter Berta. "ATLAS jet and missing-ET reconstruction, calibration, and performance". In: *Nuclear and Particle Physics Proceedings* 273-275 (2016). 37th International Conference on High Energy Physics (ICHEP), pp. 1121–1126. ISSN: 2405-6014. DOI: `https://doi.org/10.1016/j.nuclphysbps.2015.09.176`. URL: `http://www.sciencedirect.com/science/article/pii/S2405601415006653`.

[85] ATLAS Collaboration. *ATLAS muon spectrometer: Technical Design Report*. Technical Design Report ATLAS. Geneva: CERN, 1997. URL: `https://cds.cern.ch/record/331068`.

[86] AtlasPublic TWiki. *Luminosity Public Results Run2*. URL: `https://twiki.cern.ch/twiki/bin/view/AtlasPublic/LuminosityPublicResultsRun2#Multiple_Year_Collision_Plots` (visited on 03/03/2020).

[87] Runyu Bi et al. *Complete measurement of the top-quark polarisation in t-channel single top-quark production using pp collisions at* $\sqrt{s}$ = 13 *TeV with the ATLAS detector*. Tech. rep. ATL-COM-PHYS-2019-326. Geneva: CERN, Apr. 2019. URL: `https://cds.cern.ch/record/2671941`.

[88] Morad Aaboud et al. "Performance of the ATLAS Trigger System in 2015". In: *Eur. Phys. J. C* 77.5 (2017), p. 317. DOI: `10.1140/epjc/s10052-017-4852-3`. arXiv: `1611.09661 [hep-ex]`.

[89] Daniel Froidevaux and Paris Sphicas. "General-Purpose Detectors for the Large Hadron Collider". In: *Annual Review of Nuclear and Particle Science* 56.1 (2006), pp. 375–440. DOI: `10.1146/annurev.nucl.54.070103.181209`. URL: `https://doi.org/10.1146/annurev.nucl.54.070103.181209`.

[90] Georges Aad et al. "Muon reconstruction performance of the ATLAS detector in proton–proton collision data at $\sqrt{s}$ =13 TeV". In: *Eur. Phys. J. C* 76.5 (2016), p. 292. DOI: `10.1140/epjc/s10052-016-4120-y`. arXiv: `1603.05598 [hep-ex]`.

[91] ATLAS Collaboration. *Electron identification measurements in ATLAS using* $\sqrt{s}$ *= 13 TeV data with 50 ns bunch spacing*. Tech. rep. ATL-PHYS-PUB-2015-041. Geneva: CERN, Sept. 2015. URL: `https://cds.cern.ch/record/2048202`.

[92] ATLAS Collaboration. *Constituent-level pile-up mitigation techniques in ATLAS*. Tech. rep. ATLAS-CONF-2017-065. Geneva: CERN, Aug. 2017. URL: `https://cds.cern.ch/record/2281055`.

[93] ATLAS Collaboration. *Optimisation and performance studies of the ATLAS b-tagging algorithms for the 2017-18 LHC run*. Tech. rep. ATL-PHYS-PUB-2017-013. Geneva: CERN, July 2017. URL: `https://cds.cern.ch/record/2273281`.

[94] M. Aaboud et al. "Performance of missing transverse momentum reconstruction with the ATLAS detector using proton–proton collisions at $\sqrt{s}$ = 13 TeV". In: *The European Physical Journal C* 78.11 (Nov. 2018). ISSN: 1434-6052. DOI: `10.1140/epjc/s10052-018-6288-9`. URL: `http://dx.doi.org/10.1140/epjc/s10052-018-6288-9`.

[95] Morad Aaboud et al. "Performance of missing transverse momentum reconstruction with the ATLAS detector using proton-proton collisions at $\sqrt{s}$ = 13 TeV". In: *Eur. Phys. J. C* 78.11 (2018), p. 903. DOI: `10.1140/epjc/s10052-018-6288-9`. arXiv: `1802.08168 [hep-ex]`.

[96] ATLAS Collaboration. *Estimation of non-prompt and fake lepton backgrounds in final states with top quarks produced in proton-proton collisions at $\sqrt{s}$ = 8 TeV with the ATLAS detector*. Tech. rep. ATLAS-CONF-2014-058. Geneva: CERN, Oct. 2014. URL: `https://cds.cern.ch/record/1951336`.

[97] G. D'Agostini. "A Multidimensional unfolding method based on Bayes' theorem". In: *Nucl. Instrum. Meth. A* 362 (1995), pp. 487–498. DOI: `10.1016/0168-9002(95)00274-X`.

[98] G. Aad et al. "The ATLAS Simulation Infrastructure". In: *Eur. Phys. J. C* 70 (2010), pp. 823–874. DOI: `10.1140/epjc/s10052-010-1429-9`. arXiv: `1005.4568 [physics.ins-det]`.

[99] B. Efron. "Bootstrap Methods: Another Look at the Jackknife". In: *Ann. Statist.* 7.1 (Jan. 1979), pp. 1–26. DOI: `10.1214/aos/1176344552`. URL: `https://doi.org/10.1214/aos/1176344552`.

[100] Jon Butterworth et al. "PDF4LHC recommendations for LHC Run II". In: *Journal of Physics G: Nuclear and Particle Physics* 43.2 (Jan. 2016), p. 023001. ISSN: 1361-6471. DOI: `10.1088/0954-3899/43/2/023001`. URL: `http://dx.doi.org/10.1088/0954-3899/43/2/023001`.

[101] Max Baak et al. "Interpolation between multi-dimensional histograms using a new non-linear moment morphing method". In: *Nucl. Instrum. Meth.* A771 (2015), pp. 39–48. DOI: `10.1016/j.nima.2014.10.033`. arXiv: `1410.7388`.

[102] ATLAS Collaboration. *A morphing technique for signal modelling in a multidimensional space of coupling parameters*. Tech. rep. ATL-PHYS-PUB-2015-047. Geneva: CERN, Nov. 2015. URL: `https://cds.cern.ch/record/2066980`.

[103] Carsten Daniel Burgard. "Measurement of $H \to W^{\pm}W^{\mp *} \to \ell^- \bar{\nu}_\ell \ell'^+ \nu_{\ell'}$ Decays at $\sqrt{s}$=13 TeV with the ATLAS Experiment and Analysis of Effective Higgs Boson Couplings". Presented 24 Jul 2017. Jan. 2017. URL: `http://cds.cern.ch/record/2290546`.

[104] Roger Barlow and Christine Beeston. "Fitting using finite Monte Carlo samples". In: *Computer Physics Communications* 77.2 (1993), pp. 219–228. ISSN: 0010-4655. DOI: `https://doi.org/10.1016/0010-4655(93)90005-W`. URL: `http://www.sciencedirect.com/science/article/pii/001046559390005W`.

[105] Morad Aaboud et al. "Analysis of the Wtb vertex from the measurement of triple-differential angular decay rates of single top quarks produced in the t-channel at $\sqrt{s}$ = 8 TeV with the ATLAS detector". In: *JHEP* 12 (2017), p. 017. DOI: `10.1007/JHEP12(2017)017`. arXiv: `1707.05393 [hep-ex]`.

[106] V. Cirigliano et al. "Is there room for CP violation in the top-Higgs sector?" In: *Physical Review D* 94.1 (July 2016). ISSN: 2470-0029. DOI: `10.1103/physrevd.94.016002`. URL: `http://dx.doi.org/10.1103/PhysRevD.94.016002`.

[107] S. Alioli et al. "Right-handed charged currents in the era of the Large Hadron Collider". In: *Journal of High Energy Physics* 2017.5 (May 2017). ISSN: 1029-8479. DOI: `10.1007/jhep05(2017)086`. URL: `http://dx.doi.org/10.1007/JHEP05(2017)086`.

[108] Nathan P. Hartland et al. "A Monte Carlo global analysis of the Standard Model Effective Field Theory: the top quark sector". In: *JHEP* 04 (2019), p. 100. DOI: `10.1007/JHEP04(2019)100`. arXiv: `1901.05965 [hep-ph]`.

[109] Gauthier Durieux et al. "The electro-weak couplings of the top and bottom quarks — Global fit and future prospects". In: *Journal of High Energy Physics* 2019.12 (Dec. 2019). ISSN: 1029-8479. DOI: `10.1007/jhep12(2019)098`. URL: `http://dx.doi.org/10.1007/JHEP12(2019)098`.

[110] Georges Aad et al. “Combination of the W boson polarization measurements in top quark decays using ATLAS and CMS data at $\sqrt{s}$ = 8 TeV”. In: *JHEP* 08.08 (2020), p. 051. DOI: `10.1007/JHEP08(2020)051`. arXiv: `2005.03799 [hep-ex]`.

[111] M Botje. “Error estimates on parton density distributions”. In: *Journal of Physics G: Nuclear and Particle Physics* 28.5 (Apr. 2002), pp. 779–789. ISSN: 0954-3899. DOI: `10.1088/0954-3899/28/5/305`. URL: `http://dx.doi.org/10.1088/0954-3899/28/5/305`.


THE TOP PORTAL
TO NEW PHYSICS
MARC de BEURS
PJOT
W
t
W
b
b

Samenvatting

Dit proefschrift met de titel “De top portaal naar nieuwe fysica” gaat over de zoektocht naar processen die nog niet door de huidige deeltjestheorie worden beschreven. Hierbij kijk ik of het zwaarste elementaire deeltje dat we kennen, het top-quark, een portaal kan zijn naar nieuwe fysica. Ik heb het werk onderverdeeld in drie delen. In het eerste deel heb ik met computersimulaties gekeken hoe nieuwe effecten zich kunnen manifesteren in gedrag van het top-quark. In het tweede deel beschrijf ik hoe we het top-quark meten met de ATLAS-detector op CERN. In het derde deel komt alles bij elkaar en confronteer ik de meetresultaten met mijn simulaties.

Waarom worden experimenten in de deeltjes-fysica, zoals op CERN, eigenlijk gedaan?

In essentie gaat het er om dat we willen weten wat er precies gebeurde bij het ontstaan van het universum: de Big Bang. Dat was een knal met ontzettend veel energie waar allemaal processen optraden die uiteindelijk hebben geleid tot de sterren, planeten en het leven om ons heen. Om deze processen te begrijpen maken we in de LHC-deeltjesversneller van CERN in zekere zin “kleine big bangs”. In twee ringen van de versneller worden protonen (de atoomkern van waterstof) versneld tot ongeveer de lichtsnelheid. Op een aantal punten kruisen de ringen en laten we de proton met veel energie op elkaar botsen. Op de plek van de botsing staan grote detectoren, zoals de ATLAS-detector, om alles wat er gebeurd tot in detail te kunnen bestuderen. Om een beetje een idee te geven van de omvang, deze ringen zijn 27 kilometer in omtrek, bevinden zich ongeveer 100 meter onder de grond en de ATLAS-detector is ongeveer zo groot als het Paleis op de Dam.

In hoeverre zeggen deze botsingen van protonen dan iets over het ontstaan van het universum?

Grappig genoeg een hele hoop. Energie maakt namelijk dingen mogelijk. Hoe meer energie je in een botsing stopt, hoe meer processen kunnen plaatsvinden en hoe beter we de oerknal kunnen ontrafelen. We weten hierdoor al ontzettend veel over de bouwstenen van het universum en welke krachten er invloed op hebben. Deze theorie noemen we het Standaard Model (SM). Een erg saaie naam voor zeker geen saaie theorie. Het SM beschrijft dat er een beperkt aantal elementaire deeltjes zijn waaruit alles en iedereen bestaat. Ook de fundamentele krachten worden beschreven door het uitwisselen van deeltjes. Aan de hand van deze theorie kunnen we vrij goed beschrijven wat er bij het begin van het universum gebeurde. Maar we weten dat het SM nog niet af is. Het SM vertelt ons namelijk dat evenveel materie als anti-materie wordt gemaakt. Als het SM het hele verhaal is, dan zou dat betekenen dat ook tijdens de oerknal evenveel materie als anti-materie is gemaakt. Dit is echter niet wat sterrenkundige zien als ze door hun telescopen kijken. Ons universum lijkt uitsluitend uit materie te bestaan. Dit wijst erop dat er nog niet ontdekte processen moeten zijn die tijdens de oerknal hebben plaatsgevonden. Het SM voorspelt dus een symmetrie tussen de materie en anti-materie, terwijl we een asymmetrie observeren in het universum. Deze asymmetrie noemen we “CP schending” en dat is waar ik met dit werk voornamelijk naar heb gezocht.

Materie en anti-materie, wat moet ik me daarbij voorstellen?

Alle bouwstenen, of puzzelstukjes, waar het hele universum (en dus wij ook) uit bestaat noemen we materie. Dit zijn bijvoorbeeld de elementaire deeltjes elektronen en quarks. Nu zien we in onze metingen op CERN dat er voor elk deeltje ook een anti-deeltje bestaat. Die anti-deeltjes hebben precies dezelfde eigenschappen als de deeltjes, behalve dat ze een tegenovergestelde elektrische lading hebben. Het anti-deeltje van het elektron is bijvoorbeeld het positron dat een positieve elektrische lading heeft. In het SM zijn evenveel processen waar elektronen bij betrokken zijn als waar positronen bij betrokken zijn. Hierdoor zou je verwachten dat er een gelijke hoeveelheid elektronen en positronen in het universum is. Maar dit is dus niet want we observeren.

Hoe zoek je dan naar CP schending, de asymmetrie tussen de deeltjes en anti-deeltjes?

Er zijn eigenlijk twee manieren hoe je naar dit soort processen kan zoeken. De meest voor de hand liggende is om nog meer energie in de botsingen te stoppen en kijken of er opeens nieuwe reacties plaatsvinden waarbij meer deeltjes dan anti-deeltjes worden gemaakt. Dit is niet iets wat ik zomaar kan doen, hiervoor is namelijk een nog grotere versneller nodig (waar overigens wel allemaal plannen voor zijn). Ik gebruik een andere methode: een precisiemeting. Om te kijken of er wellicht toch een kleine afwijking is met wat het SM voorspelt. Dit is eigenlijk een indirecte meting waarbij we op zoek gaan naar de “schaduw” van een nieuw proces. Ik heb het top-quark, het aller zwaarste elementaire deeltje dat tot nu toe bekend is, tot in detail bestudeerd. Hierbij maak ik gebruik van computersimulaties om een idee te krijgen hoe de “schaduw” van nieuwe processen eruit ziet bij het meten van het top-quark. Het framework dat ik voor de simulaties heb gebruikt heet “Effectieve Field Theory” (EFT). In de simulaties heb ik de schaduwen van allemaal nieuwe processen bestudeerd, waaronder een proces dat betrokken kan zijn bij CP schending.

Waarom kijk je dan specifiek naar het top-quark?

Het interessante aan het top-quark is dat hij zo zwaar is dat hij direct vervalt nadat hij is geproduceerd. Andere quarks gaan eerst andere reacties aan en worden hierdoor verstrooid. Het top-quark heeft dit niet en daardoor kunnen zijn eigenschappen worden gemeten aan de hand van zijn verval-producten. Zo zijn er bijvoorbeeld een aantal hoeken tussen gemeten deeltjes te definiëren die informatie bevatten van de spin-richting van het top-quark. In het eerste deel van mijn proefschrift heb ik gevonden dat deze hoeken ook de meeste gevoeligheid hebben voor de “schaduw” van nieuwe processen.

Spin?

Dat is één van de fundamentele eigenschappen die deeltjes hebben: een intrinsiek impulsmoment. Je zou het je kunnen voorstellen als de richting van de draaiing van een deeltje om zijn eigen as. Draait het deeltje linksom dan heet dat “spin up”, draait hij rechtsom dan heet dat “spin down”. In de werkelijkheid klopt deze klassieke omschrijving alleen niet helemaal. Voor de complete beschrijving heb je namelijk kwantummechanica nodig. Wel is spin behouden. Dit betekent dat als het top-quark “spin up” had, dan hebben zijn verval-producten samen ook “spin up”. De informatie wordt dus doorgegeven en dat kunnen we meten aan de hand van een aantal hoeken tussen de gemeten deeltjes. In mijn proefschrift meet ik de “polarisatie” van het top-quark dat direct te maken heeft met zijn spin-richting.

Je hebt nu al een paar keer genoemd dat het top-quark zwaar is, wat moet ik me daarbij voorstellen?

Vergeleken met jou en mij is een top-quark natuurlijk helemaal niet zo zwaar. Maar wij bestaan dan ook uit ontelbaar veel atomen die weer bestaan uit tientallen protonen en neutronen (die weer uit quarks bestaan). Vergeleken met andere deeltjes is het top-quark superzwaar. Namelijk, ongeveer 172 keer zo zwaar als de kern van een waterstofatoom, terwijl zo een proton zelf uit drie veel lichtere quarks bestaat. Een top-quark is dus ook vele malen zwaarder dan een waterstofatoom omdat de massa van een atoom voornamelijk in de kern zit.

Maar hoe kunnen deze superzware quarks dan toch ontstaan bij het botsen van protonen?

Hier komt de bekendste natuurkundige formule van pas, namelijk die van Einstein: $E = mc^2$. Deze vergelijking vertelt ons dat energie (E) in massa (m) omgezet kan worden. In de deeltjesversneller op CERN worden de protonen versneld tot ongeveer de lichtsnelheid. Sneller dan dat kunnen ze niet. Wanneer nog meer energie in een proton wordt gestopt terwijl die al met ongeveer de lichtsnelheid gaat, kan het proton niet meer sneller en wordt hij alleen maar zwaarder. Op het moment dat je nu twee protonen op elkaar knalt, dan kan de energie omgezet worden in massa en kan dus het top-quark gemaakt worden. Leuk detail om te vermelden is dat eigenlijk quarks op elkaar moeten knallen om zwaardere deeltjes te maken. Het proton kan je zien als een zak vol met quarks die openscheurt bij een botsing. Alleen op het moment dat twee quarks elkaar vinden kunnen er zwaardere deeltjes, zoals het top-quark, gemaakt worden die interessant zijn om te bestuderen.

Hoeveel top-quarks worden er dan ongeveer gemaakt?

Per botsing niet zo veel, hooguit een paar. Dat is ook de reden dat ik meetresultaten van drie jaar heb gebruikt voor mijn onderzoek. In totaal zijn er ongeveer 30 miljoen single top-quarks in mijn dataset. Dat is ook nodig, want om een precisiemeting te doen heb je nou eenmaal veel statistiek nodig. Daar komt nog eens bij dat er ook veel andere processen bij de botsingen plaatsvinden die voor mij niet interessant zijn, zogenoemde “achtergronden”. Ik ben bijvoorbeeld alleen geïnteresseerd in top-quarks die in hun eentje worden geproduceerd, omdat ik dan precies kan weten wat zijn spin is. De botsingen in mijn dataset waarbij twee top-quarks zijn gemaakt wil ik bijvoorbeeld weggooien. Dit is niet altijd even makkelijk omdat het nogal veel kan lijken op het signaal in de detector wanneer er maar één top-quark was. Onze detector en reconstructie-algoritmes zijn namelijk niet perfect. Zo kan je wel eens een top-quark missen waardoor het lijkt alsof er maar ééntje was.

Het lijkt erop dat we nu bij het laatste deel zijn aangekomen, de confrontatie van de meting met de simulaties?

Nog niet helemaal. Je kan namelijk een simulatie niet direct met de meting vergelijken omdat de deeltjes die door detectorlagen heen gaan toch elke keer een klein beetje van richting kunnen veranderen. Deze “detector-effecten” kun je niet zomaar verwaarlozen, die moet je meenemen in je analyse. Dat doen we doorgaans door de gehele ATLAS-detector in de simulatie te bouwen. Dit kost alleen nogal wat rekenkracht aangezien de deeltjes erg klein zijn en de detector nogal groot. Ik gebruik 15 simulaties om alle mogelijke schaduwen te onderzoeken. In principe zou ik dan voor iedere simulatie opnieuw het effect van de hele detector moeten berekenen. In plaats daarvan gebruik ik een techniek die “unfolding” heet. Dit kun je het zien als een soort correctie, of filter. Hierbij hebben we de simulatie van de ATLAS-detector maar één keer nodig om te leren hoe deze filter eruit ziet, dat we vervolgens kunnen gebruiken voor alle 15 simulaties.

Hoe confronteer je vervolgens 15 simulaties met één meting?

Hiervoor gebruik ik een interpolatietechniek die we “morphing” noemen. Op de voorhand weten we namelijk niet hoe groot de schaduw van de nieuwe processen is op het top-quark. Wel bestaan er een aantal eerdere metingen waaruit we bepaalde gebieden kunnen uitsluiten. We weten dan dat daar geen ruimte meer is voor een schaduw. Alsnog blijft er een groot onontdekt gebied over. Een simulatie kun je zien als de beschrijving van de schaduw op één specifiek punt. Een soort pixel in het totale onontdekte gebied. Door nu simulaties te maken op een aantal slimme plekken kan ik toch een beeld krijgen van de vorm van de schaduw in het hele onontdekte gebied.

En, is het top-quark een portaal naar nieuwe fysica?

De polarisatie van het top-quark die ik heb gemeten komt overeen met wat het SM voorspelt. Dat is ergens een beetje jammer, ik had graag een afwijking gezien omdat dat betekent dat ik iets nieuws zou hebben gemeten. Dit betekent ook dat ik geen CP schending gemeten heb, de asymmetrie van de deeltjes waar ik naar op zoek was. Het top-quark is dus vooralsnog geen portaal. Wel heeft mijn resultaat de kleinste onzekerheid op het nieuwe proces dat betrokken kan zijn bij CP schending. Het gebied waar de schaduw van dit proces kan zijn heb ik dus iets kleiner gemaakt.

Wat is het belangrijkste dat jouw proefschrift bijdraagt aan de wetenschap?

Het verkleinen van de schaduw is belangrijk in de zoektocht naar nieuwe processen. Zo kan de volgende meting nog specifieker in een bepaald gebied kijken. Daarbij komt dat mijn werk laat zien dat een aantal bestaande methodes samen goed werken. Namelijk: het beschrijven van de schaduwen van nieuwe processen in het framework van EFT, deze simulaties confronteren met meetresultaten die gecorrigeerd zijn voor de detector-effecten (unfolding), waarbij ik een interpolatietechniek (morphing) heb gebruikt om het hele schaduw gebied te kunnen beschrijven. In de toekomst gaan deze technieken zeker vaker gebruikt worden. Als het aan mij ligt in een combinatie, net als wat ik heb gedaan.

Summary

This thesis with the titel “The top portal to new physics” is about the search for processes that are not described by the current theory of particle physics. I investigated if the heaviest known elementary particle, the top quark, could be a portal to new physics. I have divided the work in three parts. In the first part I used computer simulations to see how new effects can manifest considering the top quark. In the second part I describe how we measure the top quark with the ATLAS detector at CERN. In the third part everything comes together and I confront the measurements with my simulations.

Why are particle physics experiments, such as those at CERN, actually being done?

In essence we want to know exactly what happened at the birth of the universe: the Big Bang. This was an event with an enormous amount of energy where all kinds of processes occurred that ultimately led to the formation of the stars, planets and all the life around us. To understand these processes, “small big bangs” are produced with the LHC particle accelerator at CERN. In the two rings of the accelerator, protons (the atomic nucleus of hydrogen) are accelerated up to approximately the speed of light. At several locations the two accelerator rings cross and the high energetic protons collide. At these collisions big detectors, like the ATLAS detector, are stationed to study everything in detail. To give an impression of the sheer size, these rings are about 27 km in circumference, they are located around 100 meter under the ground and the ATLAS detector is approximately as big as the Palace at Dam-square.

How much do these collisions tell us about the birth of the universe?

Funny enough a lot, because energy makes things possible. The more energy you put into a collision, the more processes can happen and the better we can unravel the Big Bang. Due to these experiments, we already know much about the building blocks of the universe and with which forces they interact. This is all summarised in the theory that we call the Standard Model (SM). A very dull name for definitely not a dull theory. The SM describes that there are only a limited amount of different kinds of elementary particles from which everything and everyone around us is built. Also the fundamental forces of nature are described by the exchange of particles. On the basis of this theory we can describe quite well what happened at the early stages of the universe. But we know that the SM is not finished. Namely, the SM tells us that equal amounts of matter and anti-matter are produced. If the SM was the complete story, this would mean that also during the Big Bang equal amounts of matter and anti-matter was produced. This is however not what astrophysicists see when they look through their telescopes. Our universe seems to consist exclusively of matter. This hints to the existence of yet undiscovered processes that had to take place during the birth of the universe. The SM thus predicts a symmetry between matter and anti-matter, while we observe an asymmetry in the universe. This asymmetry is what we call “CP violation” and that is what I have mainly been looking for.

Matter and anti-matter, how should I picture that?

All the building blocks that make up the entire universe (including us) is what we call matter. These are, for example, the elementary particles electrons and quarks. In the measurements at CERN we see that for every particle there exists also an anti-particle. These anti-particles have the exact same properties as the particles, except that they have an opposite electric charge.

For example, the anti-particle of the electron is the positron which has a positive electric charge. In the SM there are as many processes that involve electrons as those that involve positrons. Because of this you would assume that equal amounts of electrons and positrons would exist in the universe. But that is not what we observe.

How would one then look for CP violation, this asymmetry between the particles and anti-particles?

There are actually two ways how you can search for this. The most obvious method is to pump more energy in the collisions and see if suddenly new types of processes occur where more particles are produced than anti-particles. This is however not something that I can just do, because for this I would need a bigger particle accelerator (for which there are plans by the way). I use a different method: a precision measurement. To investigate if there is perhaps a small deviation from what the SM predicts. This is actually an indirect measurement where we look for the "shadow" of a new process. I studied the top quark, the heaviest elementary particle known today, in great detail. I have used computer simulations to get an idea how the shadow of new processes looks like when measuring the top quark. The framework that I used in these simulations is called "Effective Field Theory" (EFT). With these simulations I studied the shadows of many new processes, of which a process that is related to CP violation.

Why do you look at the top quark in particular?

The interesting thing about the top quark is that it is so heavy that it decays immediately after its production. Other quarks first undergo other interactions which causes them to decohere. This does not happen with the top quark and therefore all its properties can be measured from its decay products. For example, a couple of angles between the measured particles can be defined that contain information on the direction of the spin of the top quark. In the first part of this thesis I found that these angles have the most sensitivity for the shadow of new processes.

Spin?

This is one of the fundamental properties that particles have: an intrinsic form of angular momentum. You can picture this as the direction of rotation of a particle around its own axis. Is a particle rotating counter-clockwise then we call this "spin up", is it rotating clockwise then we call it "spin down". In reality this classical description is not entirely correct. For the complete description one would actually need quantum mechanics. Nonetheless, spin is a conserved quantity. This means that if the top quark had "spin up", then the decay products together also have "spin up". The information is thus conveyed to the decay products, which we can measure making use of a couple of angles between the measured particles. In my thesis I measure the "polarisation" of the top quark which is directly related to its spin direction.

By now you have mentioned a couple of times that the top quark is heavy, how should I picture that?

Compared to you and me, a top quark is of course not so heavy. But this is an unfair comparison, since we consist of uncountable amounts of atoms that consist of tens of protons and neutrons (that consist of quarks). But compared to other particles, the top quark is super-heavy. Namely, approximately 172 times heavier than the nucleus of a hydrogen atom, while such a proton consists of three quarks of much smaller mass. A top quark is thus many times heavier than a hydrogen atom since the mass of an atom is almost entirely determined by the mass of the nucleus.

But how do you produce these super-heavy quarks by colliding protons?

Now the most famous equation comes in handy, namely Einstein's $E = mc^2$. This equation tells us that energy (E) can be converted into mass (m). Protons are accelerated up to almost the speed of light in the particle accelerator at CERN. Faster than that is not possible. When at this stage more energy is put into the protons, while they already travel at nearly the speed of light, the proton can not go faster and can only become heavier. If you then collide two of these accelerated protons, their combined energy can be converted into mass and the top quark could be produced. A nice detail to mention here is that actually the quarks inside the proton need to collide in order to make the heavier particles. You can picture a proton as a bag full of quarks that tears open on collision. Only when two quarks meet each other, heavy particles, like the top quark, can be produced that are interesting to study.

How many top quarks are then approximately produced?

At each collision not so many, maximally a couple. That is also the reason that I have used three years worth of data taking for my research. In total there are about 30 million of single top quarks in my dataset. Such an amount is necessary, because one needs a lot of statistics for a precision measurement. On top of that, there are many other processes that can occur at these collisions that are not interesting for my work, which I call "backgrounds". I am for instance only interested in top quarks that have been produced on their own: single top quarks. Because in that way I can know precisely what its spin is. I for example want to remove the collisions from my dataset where two top quarks have been produced. This is not always an easy task, as two top quarks could resemble the signal in the detector as if there would have been only one top quark. Our detector and reconstruction algorithms are not perfect. This way you can sometimes mis one top quark making it look as if there was only one in the first place.

Its seems that we have arrived at the final part, the confrontation of the simulations to the measurement?

No, not yet. The reason being that you can not directly compare the simulations with the measurement, because the particles can change their direction of movement each time when they propagate through the layers of the detector. These "detector effects" can not be neglected and have to be taken into account in the analysis. This is most often done by building the entire ATLAS detector into the simulation. However, this will lead to a lot of computation time to run the simulation since the particle are tiny and the detector is huge. Furthermore, I use 15 simulations to study all possible shadows. Which means that in principle I would need to calculate the effects caused by the ATLAS detector also 15 times, once for each simulation. In stead of doing that, I use a technique called "unfolding". You can see this as a correction, or filter, that summarises the detector effects. Now I only need to simulate the ATLAS detector once, to learn how this filter looks like, which I thereafter use for all my 15 simulations.

How do you then confront 15 simulation with one measurement?

For this I use an interpolation technique that we call "morphing". In advance we do not know how large the shadow of these new processes on the top quark can be. There exist earlier measurement results from which we can exclude certain areas, we know that in those areas there is no more room left for a shadow, nonetheless a large undiscovered area remains to be investigated. One simulation is like the description of the shadow in one particular point, something like a pixel in the total undiscovered terrain. By creating simulations in smart locations, I can obtain an image of the shadow in the entire unknown area.

And, is the top quark a portal to new physics?

The polarisation of the top quark that I have measured is consistent with what the SM predicts. That is somewhat unfortunate, I would have liked to have seen a deviation since that would indicate that I would have measured something new. This result also means that I did not find any CP violation, the asymmetry of the particles that I was after. For the time being, the top quark does not seem to be a portal to new physics. My result does have the smallest uncertainty on the process that can be involved with CP violation. I have thus made the area smaller where the shadow of this process could be.

What is the most important contribution that your thesis brings to science?

Decreasing the size of the shadow is very important in the search for new processes. This way the next measurement can focus their attention on a smaller area. Furthermore, this work shows that a number of existing techniques work well together. Namely: describing the shadows of new processes using the EFT framework, confronting these simulation with measurement results that have been corrected for the detector effects (unfolding), making use of an interpolation method (morphing) to describe the entire shadow area. In the future these techniques will most certainly be used more often. If you ask me, in some sort of combination, such as what I have done.

Acknowledgements

These last years have been a wonderful journey. I must say that I enjoyed it very much and that I am also quite happy with the outcome of all the work. Of course I could not have done it on my own. In this last chapter I want to express my gratitude to all that supported me throughout my PhD.

I like to start with thanking my promoter and daily supervisor Marcel Vreeswijk. Ik waardeer het ontzettend hoe jij mij hebt begeleidt gedurende deze jaren. Niet alleen je professionele kennis, maar ook je sociale manier van communiceren. Ik heb mij altijd helemaal vrij gevoeld in mijn werk, maar nooit alleen omdat ik altijd met van alles bij je kon aankloppen. Van de discussies die we dan hadden heb ik ook elke keer flink genoten. Fantastisch ook dat ik officieel je eerste promovendus ben, aangezien je afgelopen jaar professor bent geworden. Deze titel heb je in mijn ogen ook meer dan verdient. Ook wil ik je bedanken voor al je geduld bij het lezen en verbeteren van mijn thesis. Erg fijn hoe snel je was met het terugsturen van feedback. Ik wil graag 1 quote van jou delen, waaruit blijkt hoe een goede begeleider jij bent. Het was rond het moment dat mijn opvolger, Jordy, net was begonnen met zijn PhD. We zaten te praten en ik zat vol met ideeën wat Jordy allemaal zou kunnen gaan doen. Hierop reageerde jij met het volgende: “Allemaal leuke plannen, maar vergeet niet dat het wel zijn eigen PhD is hè”. Marcel, ik heb me geen betere begeleider kunnen wensen. Dank voor deze goede tijd!

Uiteraard wil ik ook mijn copromotor Eric Laenen bedanken. Jouw theoretische expertise heeft mijn werk naar een hoger niveau gebracht. Zeker in het begin, wanneer ik met MC simulaties bezig was. Super dat we dit onderdeel hebben kunnen publiceren samen! Ik moet bekennen dat ik het eerste gesprek met jou nogal spannend vond. Dit was nog voordat ik was aangenomen, dus waarschijnlijk nog een onderdeel van de selectie procedure. Maar aangezien ik mijn bachelor en master in Delft heb gedaan, was mijn theoretische kennis van particle physics niet spectaculair. Uiteindelijk viel het mee hoe erg je mij in dat eerste gesprek aan de tand hebt gevoeld. In alle gesprekken daarna heb jij mij telkens verder en verder geholpen, zodat ik uiteindelijk anderen binnen de ATLAS groep met theoretische kwesties heb kunnen helpen. Ook wil ik je bedanken voor je hulp en feedback tijdens het schrijven van dit proefschrift. Mede dankzij jou is het geworden zoals het nu is.

I like to continue with thanking all the members on the committee - Eleni Vryonidou, Pamela Ferrari, Paul de Jong, Stan Bentvelsen, Gerhard Raven, Wouter Verkerke and Ivo van Vulpen - for kindly agreeing to read all of this thesis. I also want to thank Patrick Decowski for your support as a C3 member and for following my progress throughout the years.

Special thanks goes out to Eleni with whom I have worked together at the start of my PhD. You really helped me getting up to speed with MC simulations and EFT. All our meetings and discussions were always very fruitful and enjoyable. Thank you also for being there for me to answer all my questions, even after our collaborative work had finished. Your patience and clarity was always much appreciated.

Additionally I want to thank Casten Burgard for all his help and support related to morphing. Even though I know you must have been very busy, you always found time to have a “quick” Skype call (which often took more like an hour). Ook wil ik Jordy de Vries bedanken voor zijn betrokkenheid. Fijn om af en toe met jou over EFT, of andere zaken, te kunnen discussiëren. Furthermore I want to thank Marco Zaro for his help with Madgraph, Darren Scott for EFT discussions and Tomas Dado for your support related to fitting.

Of course I also want to thank my collaborators from Valencia and Pittsburgh: Runyu, Joe, Nello, Susana, Maria Jose, Carlos, Oscar, Galo, Jim, Chi Wing and Huacheng. We had many (long) meetings from which our work really benefited. At the time of writing we are really close to publishing the final result. I know that by the time you read this, we will have succeeded. Special thanks goes out to Galo. We had many private discussions on unfolding and building the covariance matrix. It really helped me push my knowledge on these topics forward and only with your help I was able to fit both $\cos\theta_x$ and $\cos\theta_y$ polarisation angles together. I also want to thank Carlos for the amazing amount of work that you have done. Not only were you an expert in unfolding, you also took the responsibility to take over the template fit when Runyu had finished his PhD. Without you there would definitely not have been a combined paper. I additionally want to thank Jim, Carlos and Sebastian Merkt for their time and contributions to the "Regular EFT meeting" that I organised. Last but not least I would like to thank my successor Jordy Degens. Erg fijn om een andere student op het Nikhef te hebben gehad die met vergelijkbaar werk bezig was. Hierdoor konden we gemakkelijk over alle technische maar ook praktische en sociale dingen praten.

Ook wil ik graag Martijn van Calmhoudt bedanken voor zijn hulp bij het schrijven van de sammenvatting. Toen ik met het een idee kwam om een interview format te gebruiken was jij direct enthousiast. Heel fijn, want het was anders een beetje gek geweest om een soort van interview met mezelf te houden. Vervolgens wil ik graag Elies en Klompie bedanken voor het proeflezen van mij samenvatting en het nuttige en leuke commentaar.

Ook wil ik mijn neef Pjot heel erg bedanken voor de prachtige voor- en achterkant. Je had zelfs zo veel mooie tekeningen gemaakt dat je het mij moeilijk maakte om te kiezen, ik heb ze er gewoon allemaal ingestopt. Zonder jou was dit maar een erg kaal proefschrift geworden.

Besides all the work that had to be done, there has been also a lot of time for unwinding with colleagues for which I would like to thank the whole of the ATLAS group at Nikhef, the rest of the students and staff I have met at Nikhef, and the members of the PhD council. Especially, I would like to thank Broos, Marko and Karel, a group I ended up eating quite a bit of cheese fondue with. Before you guys I actually never ate fondue so far away from the mountains, but thanks to our cheese smuggler Marko, it tasted amazing even in Amsterdam. Also, I would like to thank Matthew and Shuvay who made my time in Geneva so much fun! Even though we do not live so close together any more, I am sure we will keep seeing each other. Our trip together with Broos to South Africa was "Baya Lekker" and has been a great sealing of our friendship, undoubtedly we will have more trips like this! Also, I would like to thank Shuvay and Dominick for our apartment in Saint Genis Pouilly. As the "Three amigos" we had a great time and our parties with beer on tap were unforgettable. Keep melting that cheese whenever there is snow on the Jura (or Mount Blanc)! I additionally want to thank all my football palls at CERN: the AGFC team, the "le box" indoor team and our team at the CERN league.

Ook wil ik mijn vrienden bedanken voor de nodige afleiding en support. De Moose meneren, andere Guldenaren, de boys van de Domini, de Oude Strijders, de 27'ers en de mannen van WV. Uiteraard ben ik ook mijn familie heel dankbaar voor alle steun. Paps, de Moes, Saar, Egbert, Hein en Dinnie, jullie stonden altijd voor mij klaar. Oom Prak vergeet natuurlijk ook zijn kleine nichtjes niet: Nova, Lilou en Marie, jullie hebben de magische kracht om altijd een glimlach op mijn gezicht te toveren. Last but not least, wil ik natuurlijk mijn verloofde bedanken. Elies, jouw steun en betrokkenheid heeft mij altijd veel kracht gegeven. Zelfs tijdens de lockdown, wanneer we met z'n tweeën in ons kleine appartementje in de Pijp aan het werken waren, ben jij er altijd voor mij geweest. Ookal hield ik je nogal al vaak van je werk, zelfs tijdens het schrijven van dit dankwoord bijvoorbeeld. Bedankt voor jouw geduld en vertrouwen.

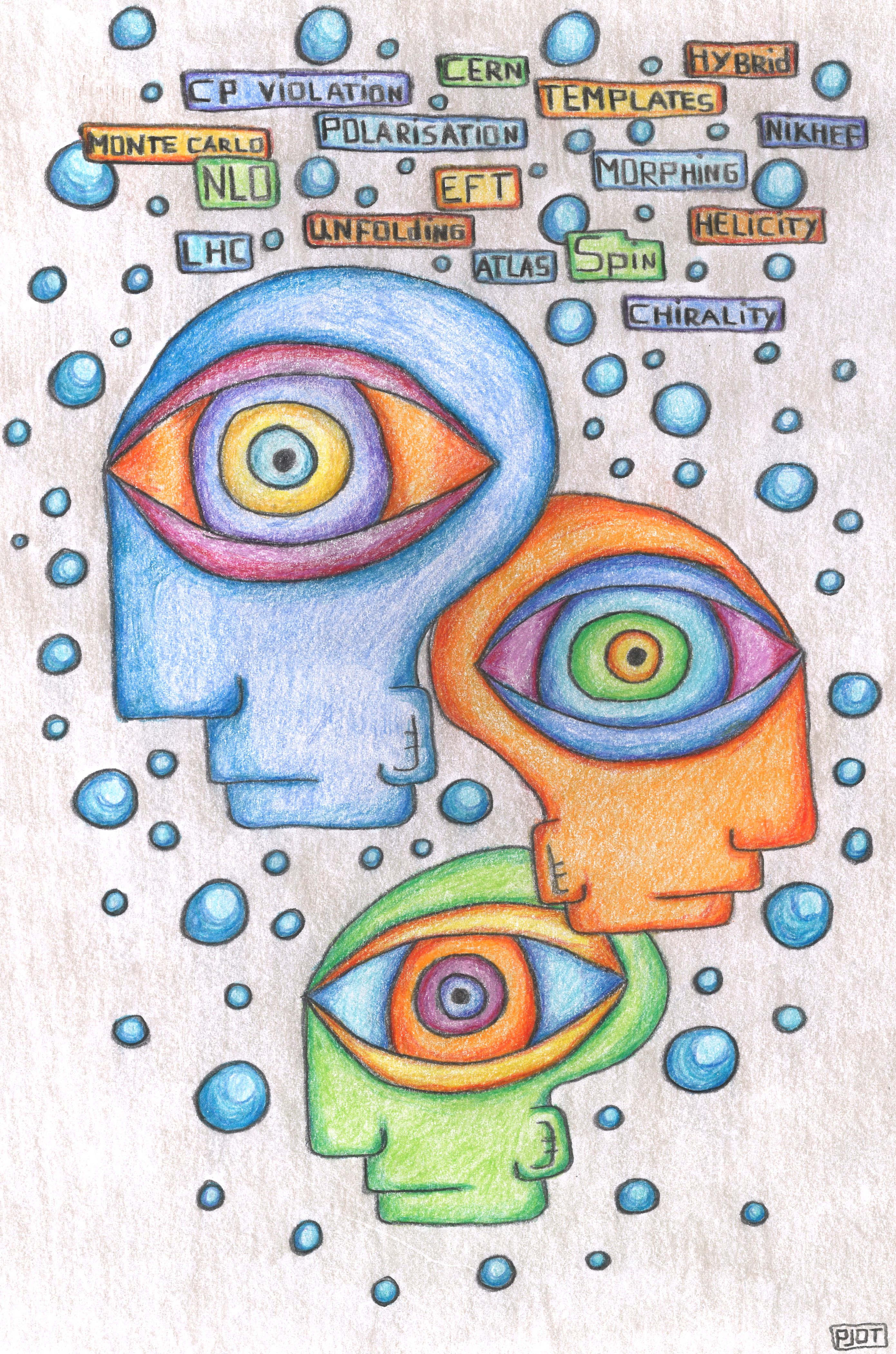
CERN
HYBRID
CP VIOLATION
TEMPLATES
MONTE CARLO
POLARISATION
NIKHEF
NLO
EFT
MORPHING
UNFOLDING
HELICITY
LHC
ATLAS
SPIN
CHIRALITY
PJOT